ABSTRACT

INFLUENCE OF DEFECTS AND IMPURITIES ON SOLAR CELL PERFORMANCE

by
Vinay Budhraja

Multicrystalline silicon (mc-Si) solar cells exhibit high impurity content and higher density of crystal defects such as grain boundaries, dislocations, stacking faults and impurity precipitates. Even though the effect of dislocations on mc-Si solar cell performance has been studied, a severe lack of understanding of the quantitative effects of dislocations on cell parameters still exists. Some correlation has been reported under the assumption of a uniform distribution of dislocation density and a negligible effect of front and back surface recombination velocity. This assumption can cause a significant error as the current mc-Si technology provides good surface passivation by SiN:H and very effective back surface fields.

This work is an extension of previous models that use Green Function to include the influence of front (S_1) and back (S_2) surface recombination velocities. The three dimensional continuity equation of the minority carriers has been solved in a solar cell having periodic array of dislocations and with front and back surface recombination. Each dislocation is considered to be a space charge cylinder perpendicular to the surface and extending through the entire cell. The calculations show that low dislocation densities ($< 10^4$ cm^{-2}) have very little effect on the cell performance. This is in agreement with the previously published data. The results of calculated dependencies of cell parameters on the dislocation density for different recombination activities are discussed in this work.

INFLUENCE OF DEFECTS AND IMPURITIES ON SOLAR CELL PERFORMANCE

by
Vinay Budhraja

A Dissertation
Submitted to the Faculty of
New Jersey Institute of Technology
in Partial Fulfillment of the Requirements for the Degree of
Doctor of Philosophy in Electrical Engineering

Department of Electrical and Computer Engineering

January 2012

.

APPROVAL PAGE

INFLUENCE OF DEFECTS AND IMPURITIES ON SOLAR CELL PERFORMANCE

Vinay Budhraja

Dr. Durgamadhab Misra, Dissertation Co-Advisor Date
Professor of Electrical and Computer Engineering, NJIT

Dr. Nuggehalli M. Ravindra, Dissertation Co-Advisor Date
Professor of Department of Physics, NJIT

Dr. Bhushan Sopori, Dissertation Co-Advisor Date
Principal Scientist, NREL

Dr. Marek Sosnowski, Committee Member Date
Professor of Electrical and Computer Engineering, NJIT

Dr. Edip Niver, Committee Member Date
Professor of Electrical and Computer Engineering, NJIT

BIOGRAPHICAL SKETCH

Author: Vinay Budhraja

Degree: Doctor of Philosophy

Date: January 2012

Undergraduate and Graduate Education:

- Doctor of Philosophy in Electrical Engineering,
  New Jersey Institute of Technology, Newark, NJ, 2012
- Master of Technology in Materials Science Programme,
  Indian Institute of Technology Kanpur, India, 2007
- Bachelor of Technology in Electronics and Communication Engineering,
  Institute of Engineering and Technology Kanpur, India, 2004

Major: Electrical Engineering

Presentations and Publications:

V. Budhraja, B. Sopori, N.M. Ravindra, and D. Misra, "Improved dislocation model of silicon solar cells with the effect of front and back surface recombination velocity," to be published.

V. Budhraja, D. Misra, and N.M. Ravindra, " Advancements in PV multicrystalline silicon solar cells from 1980 to 2010 – An Overview," 37th IEEE Photovoltaic Specialists Conference, Seattle, WA, USA, June, 2011.

V. Budhraja, B. Sopori, N.M. Ravindra, and D. Misra, " An improved model of dislocations in a silicon solar cell," 21st Workshop On Crystalline Silicon Solar Cells & Modules: Materials and Processes, Breckenridge, Colorado, July 31-August 3, 2011.

V. Budhraja, B. Sopori, N.M. Ravindra, and D. Misra, "An improved three dimension model of dislocations in a silicon solar cell: solution by Green's function method. Photovoltaic Materials and Manufacturing Issues II, MRS Technology Development Workshop Series, Denver, Colorado, October 4-7, 2011.

V. Budhraja, D. Misra, and N.M. Ravindra, "Simulation of device parameters of high efficiency multicrystalline silicon solar cells. Emerging Materials Research, 2011 (accepted for publication).

V. Budhraja, X. Wang, D. Misra, "MOS Capacitors with metal gate/high-k dielectrics on GaAs bulk substrate," Journal of Materials Science: Materials in Electrons, Vol. 21, No. 12, pp. 1322-1326, 2010.

B. Sopori. P. Rupnowski, S. Shet, V. Budhraja, S. Johnston, N. Call, M. Seacrist, G. Shi, J. Chen, and A. Deshpande, " Influence of defects and defect distribution in multicrystalline silicon on solar cell performance," 35th IEEE Photovoltaics Specialists Conference, Honolulu, Hawai, USA, pp. 2233-2237, June 2010.

B.Sopori, P. Rupnowski, V. Budhraja**,** M. Albert, C. Khattak, M. Seacrist, "A New, Ultrafast Technique for Mapping Dislocation Density in Large-area, Single-crystal and Multicrystalline Si Wafers," Materials Research Society, Boston, MA, December 2009.

B. Sopori, V. Budhraja, P. Rupnowski, S. Johnston, N. Call, H. Mountinho and M. Al. Jassim, "Defect clusters in multicrystalline silicon: Their nature and influence on solar cell performance," 34th IEEE PVSC, pp. 1969-1974, Philadelphia, PA, June 7-12, 2009.

B. Sopori, P. Rupnowski, V. Mehta, V. Budhraja, S. Johnston, N. Call, H. Mountinho, M. Al. Jassim, A. Shaikh, M. Seacrist and D. Carlson, "Performance limitations of mc-Si solar cells caused by defect clusters," ECS Transactions, The Electrochemical Society, 18, pp. 1049-1058, March 2009.

V. Budhraja, D. Misra, "Electrical Characterization of Metal Gate/High-k Dielectrics on GaAs Substrate," ECS Transaction, Physics and Technology of High-k Gate Dielectrics Vol. 16, No.5, pp. 455-461, 2008.

Dedicated to

The knowledge of spirituality
The king of Yogi’s
My real God
The will to innovate

Sri Omprakash ji Maharaj
(MyPujaya Guru ji)

ACKNOWLEDGMENT

It is my pleasure to express my sincere gratitude to Dr. Durga Misra and Dr. N.M. Ravindra for their guidance, suggestions and help throughout the course of this thesis work. Their close involvement and interest in this work motivated me highly to achieve the best.

I wish to express my sincere gratitude to Dr. Bhushan Sopori (Principal Engineer, NREL) who introduced me to the exciting field of Solar Cells. He has taught me so many things that will be beneficial to me in my whole life.

I am also grateful to Dr. Ana Kanevce (Scientist III, NREL) for the useful suggestions, guidance and timely help as and when required by me. I thank to Dr. Vishal Mehta and Dr. Peter Rupnowski for their technical help during the experiments.

I sincerely thank Jerry Tynan (Research Technician IV, NREL) who helped me in building equipments and set ups during my research at NREL.

I sincerely thank my lab as well as room partner, Srinivas Devayajanam for his support and discussion throughout my experiment.

I respectfully salute my friends, especially Debraj, Sudhakar, Prakash, Katherine, Yi and Audrey who supported me during my stay at NREL.

I sincerely thank my friends from NJIT, especially Dhananjay Singh, Anil and Manav for their support and timely help.

Finally, my special thanks to my Param Pujya Adhyatmic Guru Ji, my parents and my sister for their continuous encouragement, without whom the degree might remain a dream for me.

TABLE OF CONTENTS

TABLE OF CONTENTS
(Continued)

Chapter **Page**

TABLE OF CONTENTS
(Continued)

Chapter **Page**

LIST OF TABLES

Table **Page**

LIST OF FIGURES

LIST OF FIGURES
(Continued)

LIST OF FIGURES
(Continued)

Figure **Page**

LIST OF SYMBOLS

Al	Aluminium
AR	Antireflection
BSF	Back surface field
CdTe	Cadmium Telluride
CIGS	Copper Indium Gallium Diselenide
CVD	Chemical vapor deposition
cm	centimeter
c	Velocity of light
D	Diffusion coefficient
D_n	Electron diffusion coefficient
D_p	Hole diffusion coefficient
D_{it}	Density of interface states as a function of energy level
DLTS	Deep level transient spectroscopy
E	Electric field
E_c	Energy level of conduction band
E_i	Intrinsic energy level
E_t	Energy level of a recombination center
E_v	Energy level of the valence band
EBIC	Electron beam induced current
f	Distribution function
F	Photon flux reach at front surface

F_L	Photon Flux
F_n	Electron flux density
FF	Fill Factor
G	Electron – hole pair generation rate
G_n	Electron generation rate
G_p	Hole generation rate
GaAs	Gallium Arsenide
h	Planck’s constant
I	Electric current
I_{01}	Saturation current in quasi neutral region
I_{02}	Saturation current in depletion region
J	Electric current density
J_n	Electron current density
J_p	Hole current density
J_{sc}	Short – circuit current density
k	Boltzmann’s constant
L_n	Minority carrier diffusion length of electrons
L_p	Minority carrier diffusion length of holes
LBIC	Light beam induced current
MACD	Maximum achievable current density
MOS	Metal oxide semiconductor
m*	Effective mass
mA	milliamp

mc-Si	Multicrystalline silicon
mW	milliwatt
n	Electron concentration
N_A	Number of acceptors
N_D	Number of donors
N_d	Dislocation Density
n_i	Intrinsic carrier concentration
n_p	Electron concentration in p-region
n_{po}	Electron concentration in p-region at equilibrium
N_{it}	Number of interface states
nm	nanometer
N_t	Number of recombination centers
PCD	Photoconductance decay
PEB	Post Exposure Bake
PERL	Passivated emitter, rear locally – diffused cell
p_n	Hole concentration in n-region
p_{n0}	Hole concentration in n-region at equilibrium
q	Magnitude of a single electric charge
Q.E	Quantum efficiency
r_0	Dislocation core radius
R	Reflection coefficient
R_n	Electron recombination rate
R_p	Hole recombination rate

Si	Silicon
SiO_2	Silicon dioxide
Si_3N_4	Silicon nitride
S_1	Front surface recombination velocity
S_2	Back surface recombination velocity
SPV	Surface photovoltage
S.R	Spectral Response
t	Time
T	Temperature
U	Recombination rate
V	volts
V_{oc}	Open circuit voltage
W_p	Watt peak (W)
Z_j	Junction Depth
η	Efficiency of a solar cell
v_{th}	Thermal velocity
ε_o	Permittivity of free space
ρ	Charge distribution
λ	Wavelength
τ_n	Electron minority carrier lifetime
τ_p	Hole minority carrier lifetime

CHAPTER 1

INTRODUCTION

1.1 Basic Introduction of Solar Cells

A solar cell is a photovoltaic device which converts light into energy. In this process the absorption of light raises electrons to a higher energy state. The electrons dissipate their energy in the external circuit and return to the solar cell. The solar cells made up of different semiconductor materials like Si, CdTe, CIGS, GaAs etc., use photovoltaic energy conversion.

In order to describe the properties and use of photovoltaic solar cells, it is helpful to consider absorption, radiation, generation and transport of charge carriers in the semiconductor. The carriers are separated by the junction and collected at the contacts to the device and finally to the various power conditioning devices. These power conditioning devices are used for storage along with the actual utilization of power generated.

1.1.1 Solar Cell Operation and Its Parameters

A solar cell is simply a p-n junction diode as shown in Figure 1.1 (a). It consists of a potential energy barrier at the junction which creates an electric field. When light shines on a solar cell (Figure 1.1 (b)) the photons with energy greater than the band gap create electron-hole pairs (Anderson, 2005). The dark I-V characteristics of a diode are well known and are shown in Figure 1.2. Because of the electric field present at the junction, the electrons in the p-region move towards the n-side of the junction and the holes in the n-region move towards the p-side of the junction. The result is an extra component of current flowing in opposite direction to a solar cell. This is called light induced current (I_L) or short circuit current (I_{sc}). Because I_L flows in the opposite direction under light, the light I-V characteristics of the solar cell shift downwards as shown in Figure 1.2.

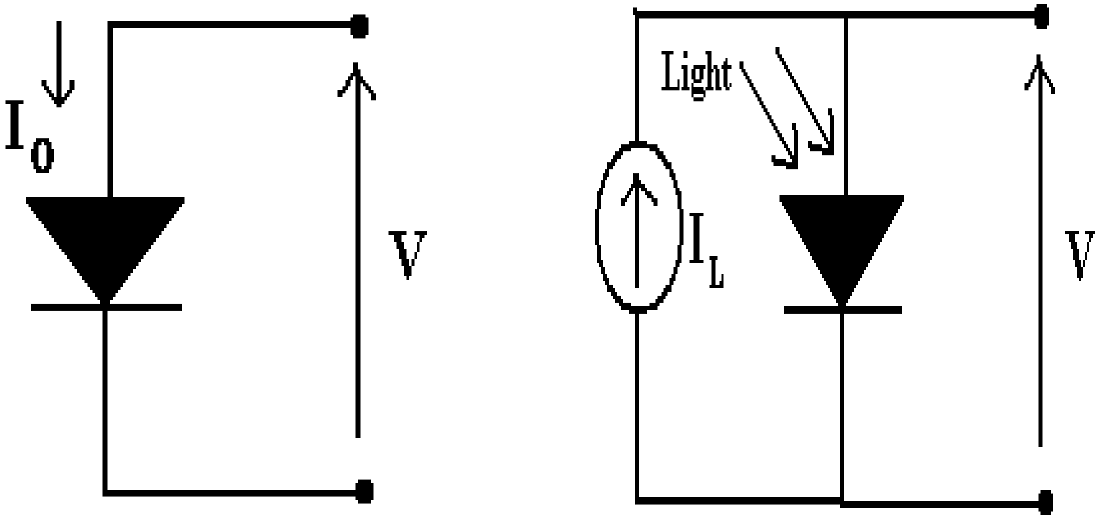

(a) **(b)**

Figure 1.1 (a) P-N junction diode (solar cell), (b) P-N junction diode (solar cell) under light.

The basics steps in the operation of solar cells are the generation of light generated carriers, the collection of those carriers to generate current, and the generation of a large voltage across the solar cell, as well as the dissipation of power in the load and in parasitic resistances (Green, 1998).

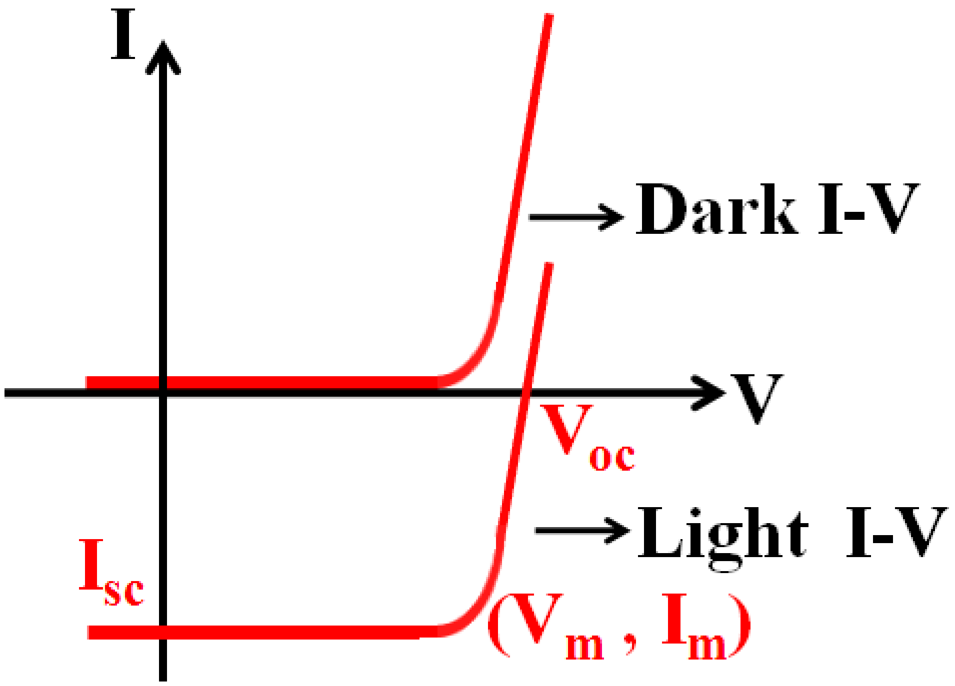

Figure 1.2 I-V characteristics of a solar cell under dark and light.

The important parameters of solar cells are I_{sc}, V_{oc} (open-circuit voltage), FF (fill factor) and η (efficiency). The I_{sc} is the current through the solar cell when the voltage across the solar cell is zero. The short-circuit current is due to the generation and then separation of light-generated carriers. The V_{oc} is the maximum voltage available from the solar cell. This occurs at zero current. The V_{oc} corresponds to the amount of forward bias on the solar cell due to the bias of the solar cell junction with the light-generated current. FF determines the maximum power from a solar cell. The FF is defined as the ratio of the maximum power from the solar cell to the product of I_{sc} and V_{oc}. The η is the important parameter to compare the performance of one solar cell to another. η is defined as the ratio of energy output from the solar cell to the input energy from the sun (Green, 1998).

The expressions for the cell parameters are given in following equations:

$$I_L=qAG\,(L_n+W+L_p) \tag{1.1}$$

$$V_{oc} = \frac{kT}{q}\ln\left(\frac{I_L}{I_0}+1\right) \tag{1.2}$$

$$FF = \frac{V_m\,I_m}{V_{oc}\,I_{sc}} \tag{1.3}$$

$$\eta = \frac{V_{oc}\,I_{sc}FF}{P_{in}} \tag{1.4}$$

The p-n junction solar cell can be expressed by the two diode model (as shown in Figure 1.3) in which the diode current is given by Equation 1.5. In the analysis of solar cells and to calculate their parameters some research groups analyzed solar cell by the single exponential diode model (Ding, 2008), (Lal, 2006), (Agarwal, 1981). Some other groups analyzed solar cells by the two diode model (Pysch, 2007), (Dyk, 2004), (Aberle, 1993), (Nielsen, 1982).

Most of the people analyzed solar cells by the single diode model to determine the ideality factor and series resistance. It is difficult to analyze the properties by the single equivalent diode model (Nishioka, 2007), (Kurobe, 2005).

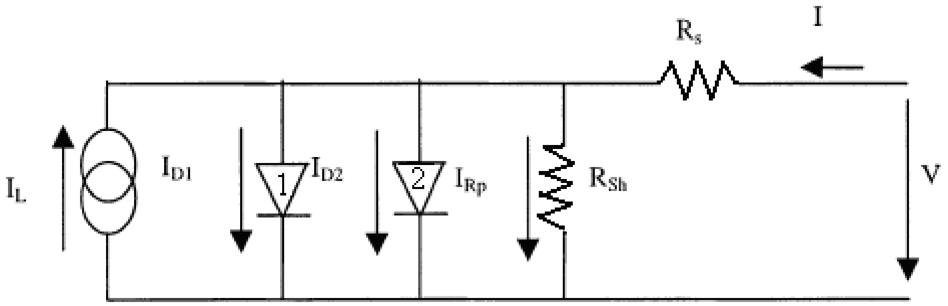

Figure 1.3 Two diode model of a solar cell (Hussein, 2001).

$$I = I_{01}\left\{\exp\left(\frac{q(V-IR_s)}{kT}\right)-1\right\} + I_{02}\left\{\exp\left(\frac{q(V-IR_s)}{2kT}\right)-1\right\} + \left(\frac{V-IR_s}{R_{sh}}\right) - I_L \qquad (1.5)$$

where I_{01} & I_{02} are the saturation currents, k is Boltzman's constant, T is the temperature, q is the electronic charge, R_s is the series resistance and R_{sh} is the shunt resistance. The first term in Equation 1.5 is due to the recombination current in the quasi neutral region (from the first diode) and the second term is due to the recombination current in the depletion region (from the second diode). The correct values of these parameters are very important to find in large area solar cells because these parameters provide the information about various losses.

1.1.2 Comparison of Solar Cells Made on Different Semiconductors

Despite various solar cells were processed on new and an exotic material, the reality is that the majority of photovoltaics market is dominated by crystalline silicon solar cells. This means that most of the solar cell manufacturers are producing their cells on silicon wafer. Moreover, a large scale of research is being done all over the world on silicon that help to produce silicon solar cells at low production cost.

The ultimate goal for photovoltaic concepts is to produce solar electricity at a cost comparable to the current market-dominant coal, natural gas, and nuclear power in order to make it the leading primary energy source (Swanson, 2006). To achieve this it may be necessary to reduce the cost of installed solar systems from about the current US$ 1.80 (for bulk Si technologies) to about US$ 0.50 per Watt peak power. Since a major part of the final cost of a silicon module is related to the high cost of solar grade polysilicon feedstock (about US$ 0.4/Watt peak) there exists a substantial drive to reduce the thickness of silicon wafer or to make solar cells from upgraded metallurgical silicon which is also called dirty Si. Figure 1.4 compares the best achievable efficiencies of different solar cells.

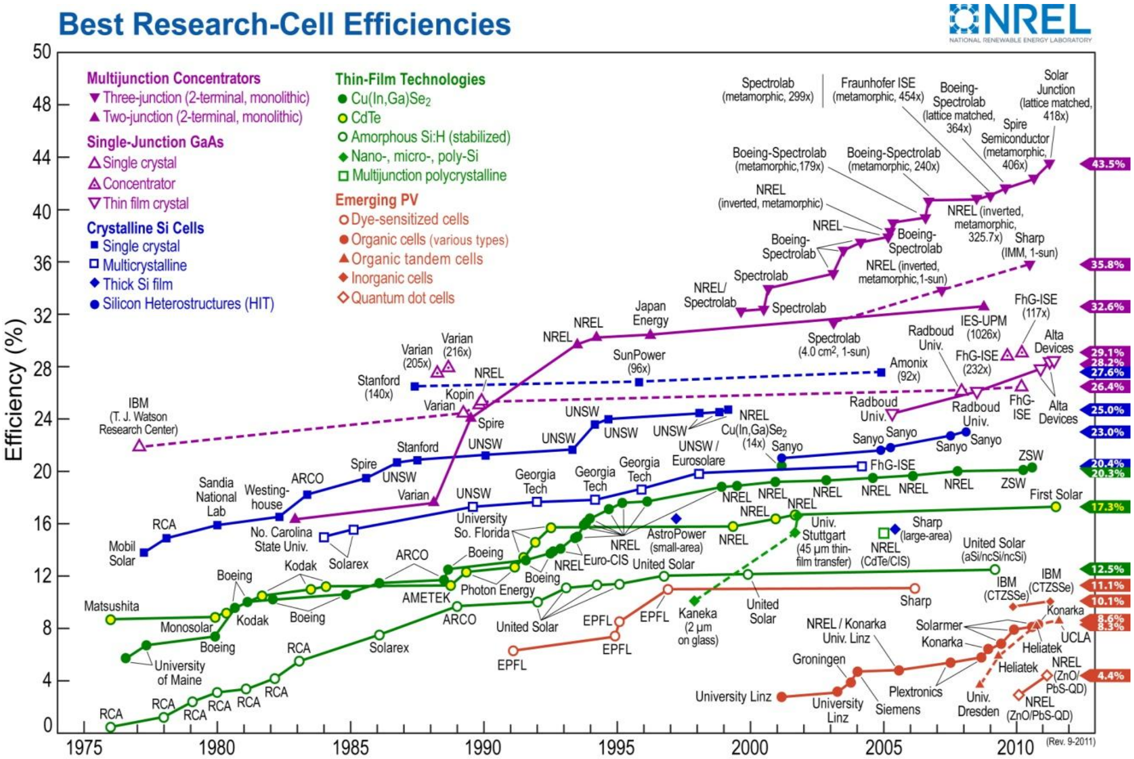

Figure 1.4 Schematic of best achievable efficiencies in different types of solar cells (Kazmerski, 2011).

1.1.3 Overview of Crystalline Silicon Solar Cells

Not only do different materials give different efficiencies, even cell efficiencies may differ for the same technology. The performance of silicon solar cell also depends on the purity of the solar wafer that is used as raw material to print solar cells, besides whether it is monocrystalline or multicrystalline solar cells. Table 1.1 shows the various types of crystalline silicon which are discriminated according to the grain size (Basore, 1994).

Table 1.1 Terminology for Various Types of Crystalline Silicon(c-Si) (Basore, 1994)

Descriptor	**Symbol**	**Grain size**	**Growth technique**
Single crystal	Sc-Si	>10 cm	Czochralski(Cz), Float Zone(FZ)
Multicrystalline	Mc-Si	1mm-10 cm	Casting
Polycrystalline	Pc-Si	1µm-1mm	Chemical Vapor Deposition
Microcrystalline	µc-Si	<1µm	Plasma Deposition

Crystalline silicon solar cells and modules have dominated photovoltaic (PV) technology from the beginning. They consists more than 85% of the PV market today. One of the reasons for the domination of crystalline silicon in photovoltaics is the fact that microelectronics has greatly developed silicon technology. Another advantage associated with silicon solar cells are that cheap silicon feedstock and second-hand equipment are available at reasonable prices.

The schematic view of a commercially fabricated crystalline silicon solar cell is shown in Figure 1.5 (Budhraja, 2011a). The processing steps that are adopted for the fabrication of silicon solar cells (Wenham, 1985), (Johnson, 1984) are as follows: (i) Starting material: p-type silicon with resistivity 1 Ω-cm, (ii) Gettering process is done to remove both areal and in-depth nonuniformities, (iii) Texturing in an acidic solution containing nitric acid, hydrofluoric acid and some additives., (iv) P (Phosphorous) diffusion (typically 900 ^{0}C to 950 ^{0}C for 5-15 minutes), (v) Junction isolation to remove n-region from the wafer edges, (vi) AR (anti-reflection) coating of silicon nitride or TiO_2 to reduce reflection losses, (vii) Front contact print (typically Ag paste is used), (viii) Back contact print (typically Al is used), and (ix) Firing of metallic contacts (front and back) in addition to achieve proper Back Surface Field (BSF). These fabrication techniques are similar in most of the crystalline silicon solar cells except for some variations are used at certain steps.

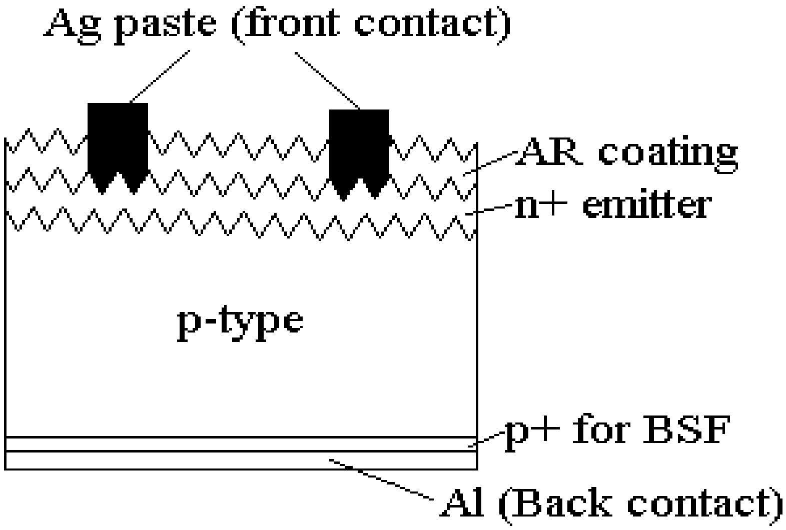

Figure 1.5 Schematic view of crystalline silicon solar cell.
(Budhraja, 2011a)

1.2 Background Information of Multicrystalline Silicon (Mc-Si) Solar Cells

The use of multicrystalline silicon solar cells has increased in the past decade because of its associated reduced cost and high efficiency (Tobias, 2003). For the past several decades, the PV market was dominated by p-type Czochralski silicon substrates. Continuous improvements in research, yields and reliability have allowed an important cost reduction and the subsequent expansion of the PV market. Because of the lower cost of mc-Si wafers, mc-Si solar cells emerged in the 1980s as an alternative to single-crystal ones.

The techniques used for the production of mc-Si are simpler, and therefore cheaper, than those required for single crystal material. However, the material quality of the multicrystalline material is lower than that of the single crystalline material due to the presence of crystal defects like grain boundaries, dislocations etc. Grain boundaries introduce high localized regions of defects which have the high recombination rate. The minority carrier life time of the wafers reduces due to the presence of grain boundaries. In addition, grain boundaries reduce solar cell performance by blocking carrier flows and providing shunting paths for current flow across the p-n junction.

To avoid significant recombination losses at grain boundaries, grain sizes on the order of at least a few mm are required (Card, 1977). The grains which extend from the front to the back of the cell provide less resistance to the path of carrier flow. Such multicrystalline silicon materials are widely used for commercial solar cell production.

1.2.1 Advancements in Mc-Si Solar Cells from 1980 to 2010

The use of mc-Si solar cells has increased in the past decade because of its associated reduced cost and high efficiency. There are a lot of improvements that have been done in various fabrication and characterization techniques to advance the technology. The improvements and research in scientific understandings helped to improve the cell efficiency from approximately 7% in 1980 to 20.3% in 2004.

A short description of the fabrication techniques (of mc-Si solar cells) that have been followed by various groups and the reported efficiencies are presented in Table 1.2. This table summarizes the changes that were introduced in the process steps and the evolution in the nature of the material over time in world-record cells.

In order to fabricate high efficiency mc-Si solar cells, process steps such as H-passivation, oxide passivation for emitter, or PECVD nitride must be followed in addition to general process steps discussed in Subsection 1.1.3. There are several other variations in the process steps such as high temperature annealing, deposition of porous silicon layer, laser fired contact etc. Mc-Si material growth from several methods such as HEM (Heat Exchange Method), EMC (Electromagnetic Casting) and DSS (Direct Solidification System) have led to promising materials to make high efficiency mc-Si solar cells (Wu, 2008).

Table 1.2 Summary of Process Recipes of Several Groups from 1980-2010

Year, Author	**Main steps in process except general steps discussed above**	**Results obtained**
1980, T. Saitoh	Impurity gettering by N_2 annealing	Efficiency: 6.14 %
1981, C.H. Seager	Hydrogen passivation	Values of cell parameters (Jsc, Voc, FF & η) increase
1984, S.M.Johnson	They used the general steps discussed above but in different order, two layer of antireflective coating was used (material: semi crystalline, area: 4 cm^2)	Efficiency: 15.7% (world record cell) this value corrected latter w.r.t AM 1.5G [13]
1985, S.R.Wenham	Plasma hydrogenation, plasma etching of emitter between contact fingers, plasma deposition of silicon nitride, PESC process (material: poly-Si, area: 4.1 cm^2)	Efficiency: 15.8% (world record cell)
1986, S. Narayanan	Passivated emitter solar cell with P-pretreatment with sheet resistivity 100-150 Ω/□	Efficiency: 15.9% (world record cell)
1988, B.L. Sopori	Backside hydrogenation during high temperature processing	Values of cell parameters increased
1989, J.C. Zolper, M.A. Green	Laser texture, laser grooved, buried contact process (material: poly-Si, area: 10 cm^2)	Efficiency: 16.7% (world record cell)
1990, D. Gilles	Internal gettering of interstitial impurities	Dissolution of oxygen precipitate
1993, A. Rohatgi	Oxide passivation after phosphorous gettering (material: OTC, area: 1 cm^2)	Efficiency: 17.7% (world record cell)
1996, D.S.Ruby	RIE, PECVD nitride, Hydrogen plasma for bulk passivation	Values of cell parameters increased
1996, A. Rohatgi	Oxide passivation after phosphorous gettering (material: HEM, area: 1 cm^2)	Efficiency: 18.6% (world record cell)
1997, S.A. McHugo	Two step P-gettering, Al gettering	Diffusion length increased
1998, J. Zhao, M.A. Green	Honeycomb textured, enshrouding cell surface in thermally grown SiO_2 (material: DS, area: 1 cm^2)	Efficiency: 19.8% (world record cell)
1999, D.Macdonald	P-gettering on top, middle, bottom regions of ingot	Lifetime of wafers increased
2002, F. Duerinckx	PECVD silicon nitride deposition	Values of cell parameters increased
2002, L.Mittelstadt	Front and rear SiN_x passivation	Efficiency >18% achieved
2003, S. Martinuzzi	Hydrogen passivation	Values of cell parameters increased
2004, O. Schultz	Laser fired contacts, Front contact textured by plasma process, wet oxidation (material: mc-Si Kawasaki steel, area: 1 cm^2)	Efficiency: 20.4% (world record cell)
2006, H.F.W. Dekkers	High temperature rapid annealing of SiN_x:H	V_{oc} and lifetime increased with respect to SiN dose
2008, T. Buonassisi	High temperature annealing of mc-Si wafer	Dislocation density reduced
2009, H. Nouri	Formed porous silicon layer on front and back sides of mc-Si wafer	cell parameters and IQE increased

Budhraja, 2010a

1.2.2 Types of Defects and its Influence on Cell Performance

Present-day crystalline silicon for photovoltaic applications usually contains a variety of defects ranging from point defects of various origins such as vacancy, substitution impurity etc. to extended defects like dislocations, grain boundaries, micro defects or second phase precipitates. Mainly the defects are due to the imperfection in crystal structure. Various types of defects like point defects, line defects, plannar defects and bulk defects have major effect on solid state devices. The effect of point defects like vacancy, interstitial etc., is mainly seen in single crystalline cells. The performance of mc-Si solar cells are mainly affected by the presence of line defects, plannar defects and bulk defects like dislocations, grain boundaries and impurities respectively. The electrical performance of such materials i.e., mainly their minority carrier lifetime, is closely related to metal impurities present in the feedstock or introduced during crystal growth and/or solar cell processing (Istratov, 2003), (Buonassisi, 2006). These impurities strongly interact with existing crystal defects to form complexes, accumulate at dislocations or grain boundaries in different forms, or even form silicide precipitates which simultaneously contain several metal impurities (Buonassisi, 2007). However, there exist two important issues in the fabrication of low cost mc-Si solar cells, the electrical loss due to recombination defects and the breakage of thin wafers due to residual strain.

The conversion efficiency of mc-Si is 2%–4% lower than that of mono crystalline Si due to the existence of crystal defects, mainly grain boundaries (GBs) (Zook, 1980), Bary, 1998), (Wang, 1999). Metallic impurities are incorporated in low grade Si feedstock precipitates at crystal defects, and enhance the recombination activities

(Maurice, 1989), (Rizk, 1994), (Kittler, 1995), (McHugo, 1998). In addition, the recombination properties of decorated crystal defects or multi-metal-precipitates have to be known if their effect on the material performance for photovoltaic applications is to be estimated.

Commercial silicon solar cells show the nonuniformities in the cell response. These nonuniformities depend on the type of material and the processes used for cell fabrication. Moreover these inhomogenities change the minority carrier diffusion length and causes device shunting (Sopori, 1980), (Fossum, 1980) which have adverse effects on large area solar cells.

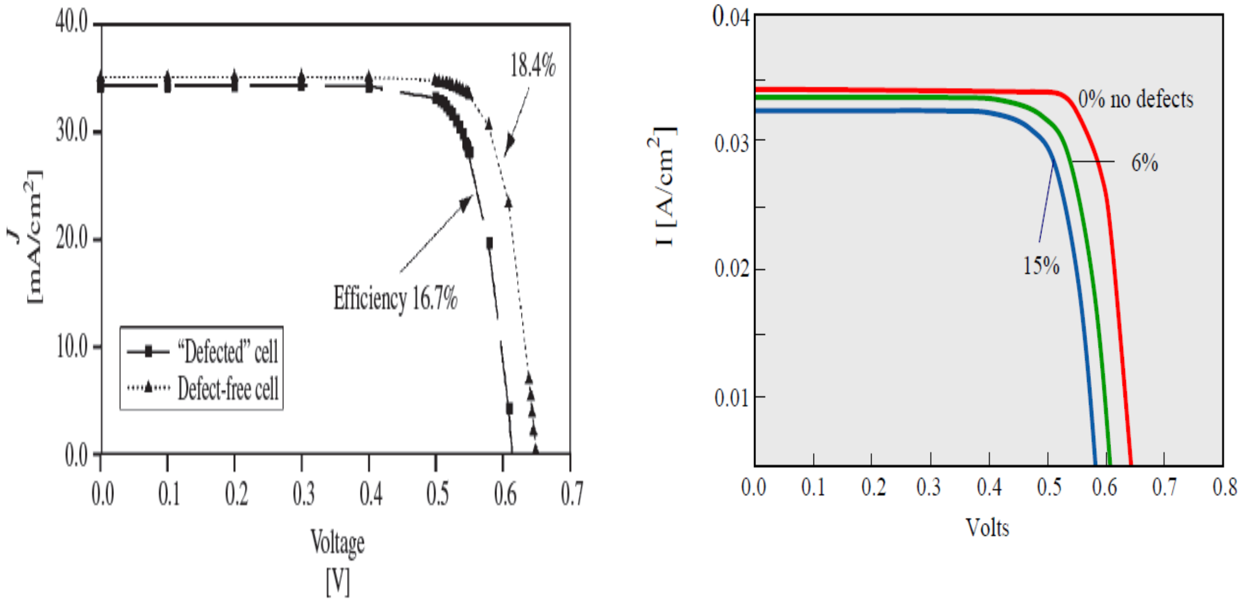

(a)

(b)

Figure 1.6 (a) I-V curves of defect free and defected cell showing degradation due to defect regions (Sopori, 2003), (b) A comparison of calculated I-V characteristics of three cells with 0%, 6%, and 15% of area covered by defects (Sopori, 2009b).

Figure 1.6 (a) shows the comparison of two large area solar cells of the same material. The cell that has the 18.4% efficiency is defect free while the other cell which has 20% of the areas covered by defects, reduces the cell efficiency (to 16.7%) and other parameters. This reduction in parameters was caused by increased recombination, which manifests as shunting due to defected regions. Such shunts represent sources of internal power dissipation within the cell (Sopori, 2003). A similar effect was seen by B.L.Sopori (Sopori, 2009b) in the comparison of three cells as shown in Figure 1.6 (b). The performance of a solar cell improves as the area covered by the defects is reduced.

Defects have the major effect on different parameters of solar cell and its performance. Solar cell performance is typically evaluated based on its efficiency. Since the high defect density in the wafer has direct impact on cell efficiency the relation between cell efficiency and dislocation density needs to be closely evaluated. This was estimated by Dimitriadis et al. (Dimitriadis, 1985) as shown in Figure 1.7 at different values of product of recombination activity S_d and dislocation core radius (Read radius) r_0. At the product of S_d and r_0 equals to one, there is a marginal change in cell efficiency when the dislocation density increases from 10^2 to 10^3 cm^{-2}. There is a rapid decrease in efficiency once the dislocation density goes above 10^4 cm^{-2}. For lower values of dislocation density, efficiency decreases slowly according to the relation $\eta \sim N_d^{-0.5}$, and for higher values of dislocation density, efficiency decreases more rapidly according to the law $\eta \sim N_d^{-1}$.

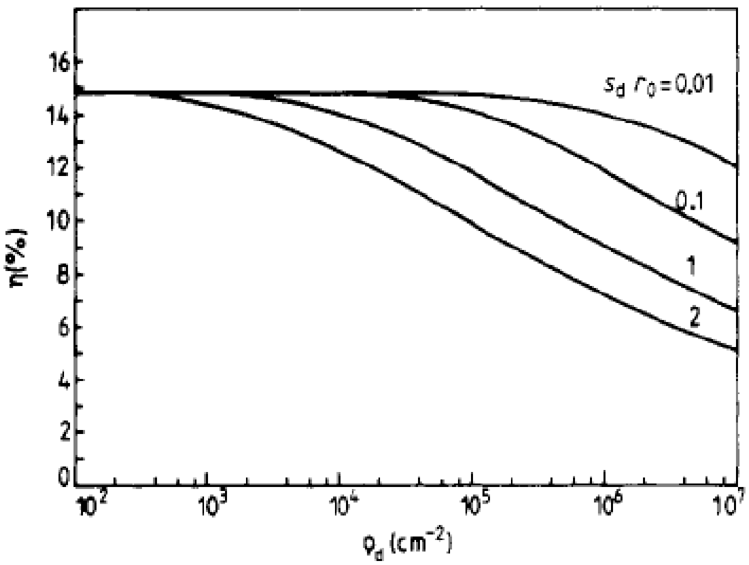

Figure 1.7 Dependence of the efficiency on the dislocation density at as a function of product of S_d and r_0 (Dimitriadis, 1985).

1.2.3 Role of Mc-Si Solar Cells in Present Technology

Mc-Si based devices dominate the present solar cell industry due to their durability, their relatively low cost, and the vast silicon knowledge base developed by the microelectronics industry (Fauchet, 2003). Mc-Si solar cells account for around 50% of total solar cell production (Macdonald, 2004). According to the January 2011 issue of *Solar Industry Magazine*, mc-Si technology represents roughly 80% of the c-Si market on a dollar per watt basis against thin film silicon, CdTe and CIGS. Mc-Si is produced from poor quality material that's why the cost of mc-Si solar cells is lower than monocrystalline silicon solar cells. The mc-Si solar cells are the best alternative to solar cells made on monocrystalline silicon because they maintain a tradeoff between cost and efficiency (Tobias, 2003). The mc-Si technology will continue to be profitable throughout the value chain from $1.45/W in 2009 to $0.93/W in 2015, assuming poly pricing at $70/Kg (Magazine article, 2011).

Mc-Si solar cells keep their market dominance due to the significant lower cost of ingot growth process compared to the mono-crystal process. In the current technology the efficiency difference mono and multicrystalline silicon solar cells remains about 1 to 2% but a continuous enhancement in the efficiency of solar cell has been done (Wan, 2010).

Table 1.3 Breakdown of Cost of Fabrication of Single and Multicrystalline Solar Cells (Tobias, 2003)

Itern	**Singlecrystalline solar cells**	**Multicrystalline solar cells**
Pure Si	38	38
Ingot information	115	35
Sawing	77	77
Wafer cost	230	150
Cell fabrication	80	80
Total components	310	230
Yield	0.95	0.9
Cell cost	326	256
Module assembling	75	75
Lamination	75	75
Module cost (Euro m^{-2})	476	406
Efficiency	0.19	0.17
Module Cost (Euro Wp^{-1})	3.4	3.38

The cost information of the fabrication of single and multicrystalline solar cells are given in Table 1.3 (Tobias, 2003).

A combination of material quality and process improvement has allowed higher efficiencies at a still lower cost which increases the share of multicrystalline in the PV market, ahead of monocrystalline. The evolution of the market can be seen in Table 1.4 (Tobias, 2003).

Table 1.4 Market Share of Single Crystalline and Multicrystalline Solar Cells (Tobias, 2003)

Year	**Cz-Si solar cells**		**Mc-Si solar cells**	
	Output [MW]	**Market share** [%]	**Output** [MW]	**Market share** [%]
1996	48.7	55	28.4	32
2000	92	32	146.7	51

1.3 Motivation

In this thesis the main focus is on mc-Si solar cell cells because of their associated advantages like largest market share, high efficiency, low cost of wafers, vast silicon knowledge, etc., as discussed in section 1.2. Among various photovoltaic materials, multi crystalline silicon (mc-Si) is now the most promising material, due to its excellent stability and reliability. The only one disadvantage is the high production cost in comparison to cells made on other semiconducting materials. To overcome this disadvantage, one scheme is to use cheap silicon feedstock. Another scheme is to reduce wafer thickness. There exists several defects like grain boundaries, dislocations, defect clusters etc. in solar grade silicon.

The effect of grain boundaries is neglected in present mc-Si solar cells because of the use of large grain size material by solar industries (Ghitani, 1989a), (Halder, 1983). Dislocations are the most harmful out of various defects. Defect clusters are also harmful but they can be assumed as the regions of very high dislocation density. When the dislocations are decorated with impurity precipitates they form regions of very high defect density and in those regions the dislocations appeared to be clustered. That's why those regions are also called dislocation cluster regions (Sopori, 2009a), (Sopori, 2010). Because of these reasons effect of dislocations on the performance of mc-Si solar cells was studied.

In the present mc-Si solar cell technology it is highly desirable to have the characterization technique by which the effect of defects on the performance of solar cell can be quantified.

It is highly desirable to have the suitable mathematical model by which the electrical characteristics of the solar cell can be compared.

1.4 Objectives

The primary objective of this research is to propose a model that will be able to provide a physical insight into the effect of dislocations on the performance of solar cells and to compare the J-V characteristics of present mc-Si solar cells. To this end, the goals are (1) to understand the advancements in mc-Si solar cells, (2) to understand the physics of the effect of defects on the performance of solar cells, (3) to understand the characterization technique called mesa diode analysis proposed by B.L.Sopori (Sopori, 1988a) to get the quantitative information of the effect of defect on cell parameters, and

(4) to fabricate diode arrays on silicon substrate to compare the different regions of wafers that have different dislocation densities. The following chapters describe the findings from the studies that were carried out in this dissertation to meet these objectives.

1.5 Dissertation Outline

There are mainly discussions on the influence of dislocations on the performance of mc-Si solar cells and the characterization techniques for defects like mesa diode analysis in this dissertation. There are other techniques like Lock in Thermography (Breitenstein, 2004), Electron Beam Induced Current (Seager, 1982), Light Beam Induced Current (Kaminski, 2004), Electroluminescence (Hinken, 2007) etc. exist which can characterize defects but mesa diode analysis is the only way to obtain spatially resolved measurements of the open circuit voltage and fill factor.

Chapter 2 discusses the physics and literature review of the nature of defects that exist in mc-Si and their influence on the performance of cells as a whole. Moreover, the applications of the defect study on the characterization of cells will be presented.

Chapter 3 discusses the dislocation model of mesa diodes, which is the extension of old dislocation model proposed by H. Al. Ghitani (Ghitani, 1989a). In the old model the effect of front and back surface recombination velocities were neglected but in the proposed model these effect are being included. The assumptions and parameters which are used in the improved dislocation model are discussed in this chapter. The derivation of current equations in different regions in the case of dark and light is given in this chapter.

Chapter 4 gives the experimental details of mesa diode arrays. The processing steps and dimensions used in the fabrication of mesa diode arrays are shown in this chapter. The mesa diode arrays are used to characterize the substrates in this work.

Chapter 5 discusses the simulation results of the improved dislocation model with the effect of front and back surface recombination velocity. These simulation results are shown under the different cases with the variations of several parameters used in the model. To confirm the reliability of the model, the comparison of modeling and experimental results is shown in this chapter.

Chapter 6 discusses the conclusions of the dissertation from Chapter 1 to Chapter 5. Suggested future work is also described in this final chapter.

CHAPTER 2

DISLOCATION STUDY ON THE PERFORMANCE OF SILICON SOLAR CELLS

2.1 Introduction

In large grain size material, defects are mainly due to dislocation. The multicrystalline silicon solar cell will have high efficiency if most of its area is covered by low dislocation density regions. High dislocation density regions are responsible for an increase in dark forward current and a, decrease in efficiency and cell parameters (Sopori, 1991), (Hartman, 2008). Two different large grain-sized multicrystalline silicon wafers will give the same average dislocation density if one wafer has most of the area covered by low dislocation density regions with only a small amount of high dislocation density regions, and the other wafer is covered by moderate dislocation density regions. The efficiency and other cell parameters will be high in the second wafer because the dark leakage current across the high dislocation density regions will be high in the first wafer. That is why it is necessary to minimize the high dislocation density regions from multi crystalline silicon. In the past few decades several methods have been adopted by researchers and solar industries to minimize the defects from multicrystalline silicon during the crystal growth and during the processing of silicon solar cells which are given as follows:

(i) The controlled nucleation mechanism during crystal growth results in low dislocation densities by doing directional solidification (Stokkan, 2010), (Moller, 2009). This utilizes dendritic growth during crystal growth to achieve multicrystalline silicon with preferred orientation and large grain size (Takahashi, 2010), (Fujiwara, 2006), (Fujiwara, 2008a), (Fujiwara, 2008b).

(ii) Reduction in dislocation density by doing high temperature annealing (Hartman, 2008).

(iii) Dislocations in the areas of low life time in multicrystalline silicon can cause life time enhancement upon phosphorous diffusion (Bentzen, 2009), (Cuevas, 1997).

(iv) Hydrogen passivation in multicrystalline silicon solar cell processing reduces defects (Tarasov, 2004), (Dekkers, 2006), (Duerinckx, 2002), (Sopori, 1988b).

2.2 Electrical Properties of Dislocations

In the study of dislocations the mid-band levels are especially active. This can be derived from the fact that holes and electrons require about equal energies to move halfway from valence band and conduction band.

Dislocations can be considered as missing electronic charges or a charge accumulation that has a stronger effect on the local band structure. The dislocations with their free bond charges have a wide range of electric field influence.

According to W. Schottky (Schottky, 1945) donor atoms can exist in both neutral and positive donor states. Similarly, acceptor atoms can exist in both neutral and negatively charged states. Schottky proposes to discriminate between states near the conduction or valence bands by the prefix “trans-” for higher states, “cis-” for states below the Fermi level as shown in Figure 2.1. For mid-band terms near the Fermi level medial donors and medial acceptors are connected to the appearance of dislocations. The influence on recombination mechanisms is shown in Figure 2.1. Such mid-band levels may be located a few kT from the Fermi level and therefore can easily be converted from a donor to an acceptor (Matare, 1970a).

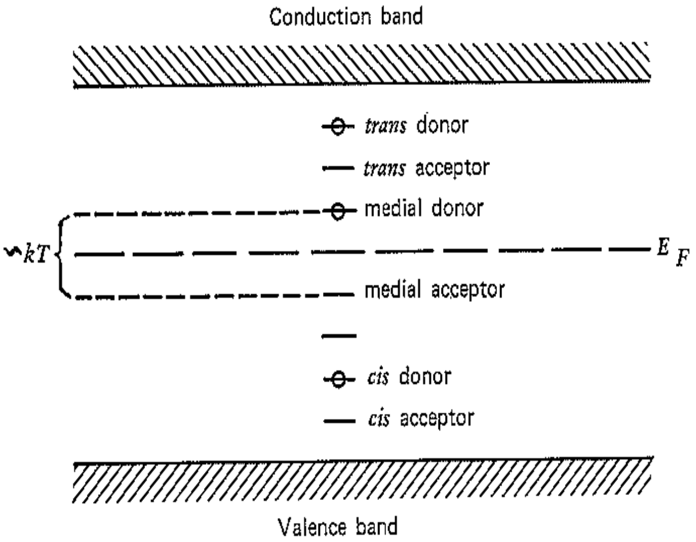

Figure 2.1 Schottky terminology for inter-band energy levels (Schottky, 1945).

Suppose a trans- acceptor exists near the conduction band in a material as shown in Figure 2.2 (a). After accepting a free electron, this band changes to cis- acceptor below the middle of the gap but near Fermi level (Figure 2.2 (b)). In the case of a dangling bond, it is thinkable that electrons are added as long as the energy is gained to lower the energy below the Fermi level. This explains the behavior of dislocations to act as hole sinks after they have been able to build a space charge cloud around themselves (Figure 2.2 (c)).

The simple recombination process is shown in Figure 2.3 (a). Either an intrinsic recombination takes place across the bandgap or by way of a recombination center.

Electrons can also reach the recombination center from the valence band or a filled recombination center can release electrons to both valence and conduction bands.

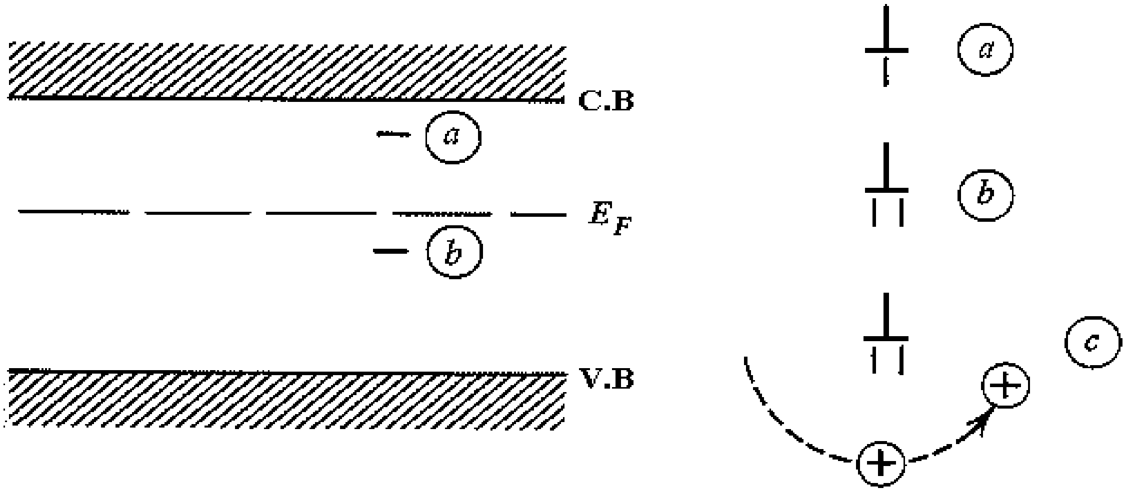

Figure 2.2 Energy level of a dangling bond that is (a) unfilled, (b) filled, and (c) compensated (Matare, 1970a).

A dislocation that has an energy level in the forbidden gap may have the following functions (Figure 2.3 (b)): (1) Accept an electron from the conduction band which is shown as process 1, (2) Release a hole to the valence band which is shown as process 4, (3) Filled levels can release an electron to the conduction band which is shown as process 2, (4) Accept a hole from the valence band which is shown as process 3.

2.2.1 Scattering Around Dislocation

Dislocations are the main sources of moving charges in real crystals. The energy difference between the Fermi level and the lower edge of the conduction band is given by

$$\zeta = E_F - E_C \approx kT \left(\frac{3}{4}\right)^{2/3} \frac{h^2}{m_{eff}} n^{2/3} \tag{2.1}$$

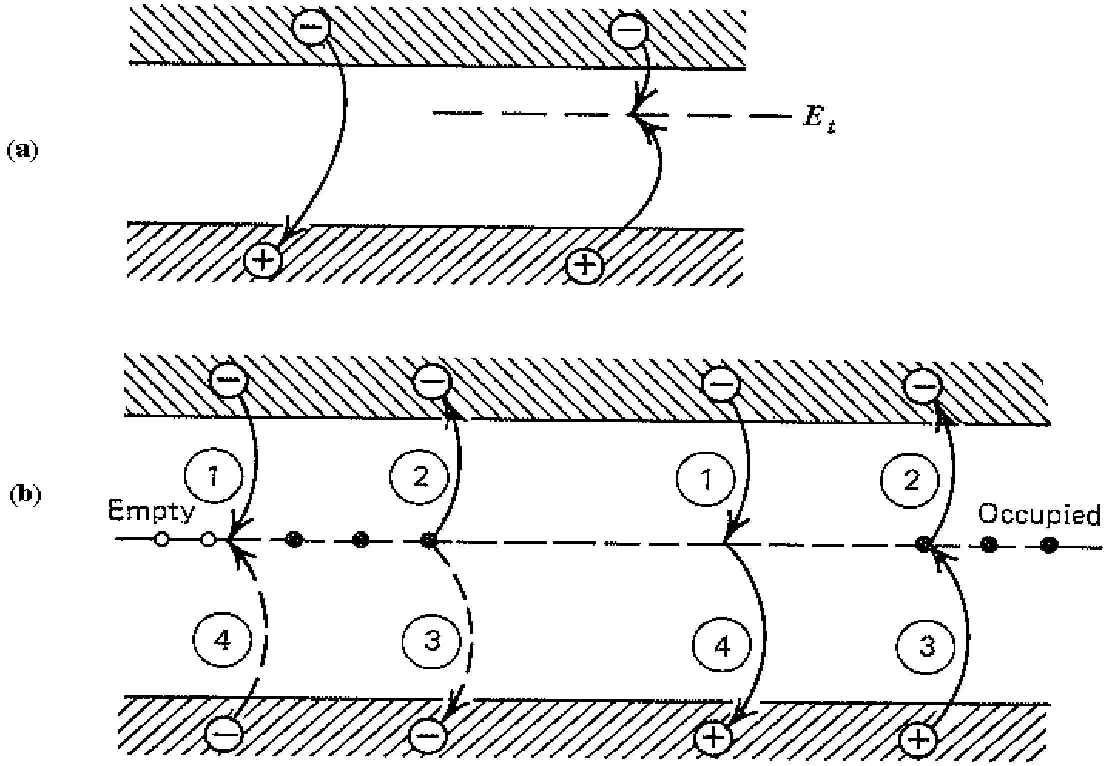

Figure 2.3 (a) Hole electron recombination, (b) Different recombination processes via empty and filled centers in the forbidden gap (Matare, 1970a).

In an electric field the particle acceleration is

$$a = -\frac{eE}{m} \tag{2.2}$$

The drift velocity is given by

$$v_d = -\frac{e\tau}{m} E \tag{2.3}$$

The current carried by n charges in a three-dimensional sample is

$$i = e\mu nE \tag{2.4}$$

where μ is the mobility of the sample. Aside from charge defects, lattice vibrations are the strongest disturbance for the electronic charge transport.

In three-dimensional space the scattering leads to three components of current for the electron. In momentum space a group n_i of electrons in a volume element produces a current density

$$\delta I = -\frac{ev_i}{V}\delta n_i \tag{2.5}$$

where v_i is the velocity component of group n_i and V is the crystal volume under consideration.

The fraction of carriers scattered into new directions with velocity v_j during time dt changes the current increment to

$$d\delta I = dt\int_0^{\Omega(E)} \frac{-e(v_j - v_i)}{V}\int \frac{-e(v_j - v_i)}{V}\delta n_i W_{ij} d\Omega_j \tag{2.6}$$

where $\Omega(E)$ is the energy surface and, W_{ij} is the transition probability from state i to j.

The current change can be expressed by

$$d\delta I = -dt\, \delta I\, W_0 < 1 - \cos\theta > \tag{2.7}$$

where $< 1 - \cos\theta >$ is introduced as the average scattering parameter for all collision processes.

Figure 2.4 shows the cases of scattering electrons for fixed scattering angle θ.

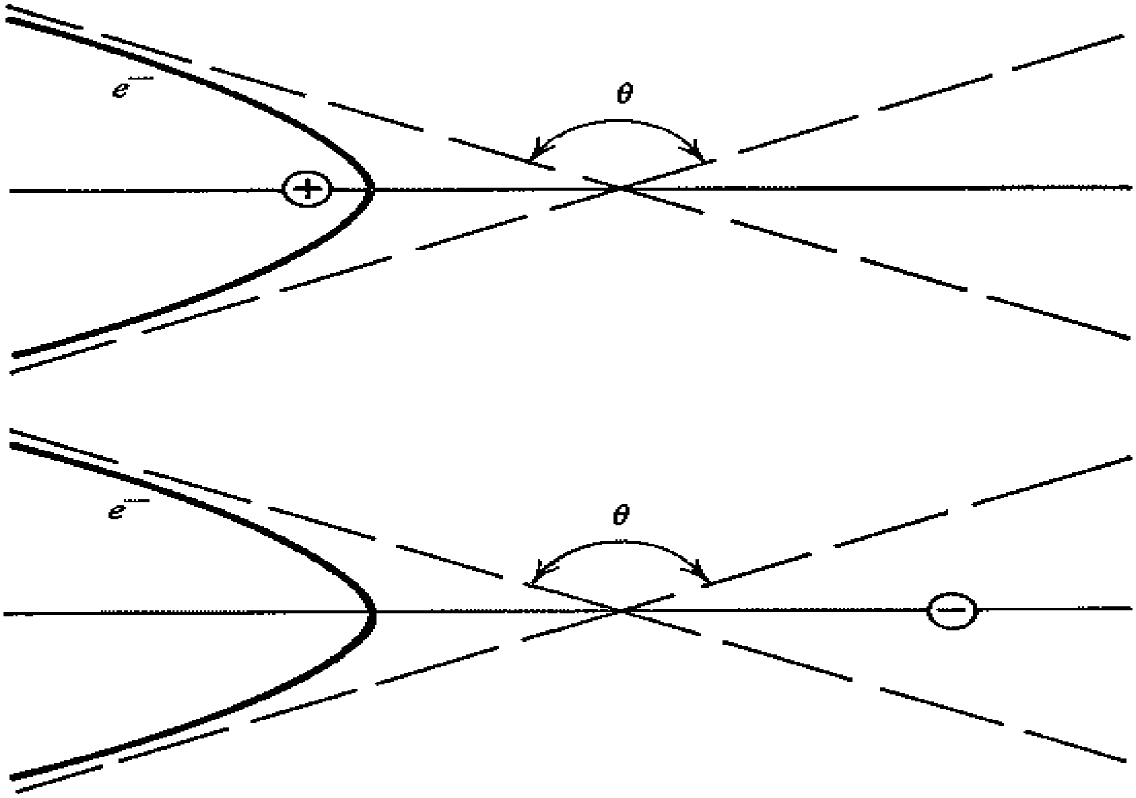

Figure 2.4 Electron scattering at positive and negative ions (Matare, 1970a).

Dislocation sites are charge centers either because of doping mismatch when lattice dilation and compression react as sink for specific ions, or because of dangling bonds. In either case a strong core charge can be accomplished by a space charge.

2.2.2 Formation of a Dislocation Pipe or a Dislocation Cylinder

If more dislocation arrays are generated instead of point defects, dislocation space charge pipes are formed and have a strong scattering influence on carriers that can be assessed in the same way as done for neutral impurities. In this case, one can assume that a dislocation acts as an inpenetrable cylinder.

Dislocations in semiconductors act as electrically active defects. They can be acceptors or donors, recombination centers reducing the life time of minority carriers or scattering centers. Electrically charged dislocations are surrounded by a screening space charge that causes local band bending and therefore may change the charge state of point defects in this region. Plastic deformation of semiconductor crystals introduces deep states into the gap. They are due to the dislocations themselves. The pioneering work in this field was published by W.T.Read (Read, 1954). Dislocations are the lines of variable charge. Read calculates the occupation of the dislocation for a given doping and temperature from the minimum energy of the system. A certain probability for electron hopping along the dislocation must be taken into account. Entropy will lead to a minimum of free enthalpy at a non-equidistant arrangement of the charges. The electrostatic potential around a charge dislocation is given by

$$\Psi(r) = A \ln r + \frac{Q}{4\varepsilon} r^2 + C \tag{2.8}$$

where Q is the space charge around the line. The divergence for r→0 can be overcome by taking into account in the vicinity of the dislocation line and the discrete nature of charges. The screening of a charged line by a space charged cylinder of the opposite sign prevents the divergence of the potential for r→∞. The screening by ionized donors contained in a cylindrical region with a sharp radius R can be assumed as

$$R = (a\,\pi\, l\, N_D - N_A l)^{-1/2} \tag{2.9}$$

where R is the Read radius. Outside R the potential Ψ vanishes. Likewise the electric field disappears for $r \geq R$.

2.2.3 Charge Carrier Transport Across Edge and Screw Dislocation

There is considerable lattice disturbance due to the following: (1) The local stress around dislocations, (2) The disrupted or dangling bond with its specific charge and energy level, and (3) The space charge domain that forms immediately in semiconductors and surrounds the dislocation lieu in the form of a space charge pipe.

The edge dislocation introduces a strong discontinuity in the local stress pattern changing from pure compression to pure dilation. This has the effect of changing the forbidden gap of the semiconductor because of the resulting local compression increment in the deformation potential.

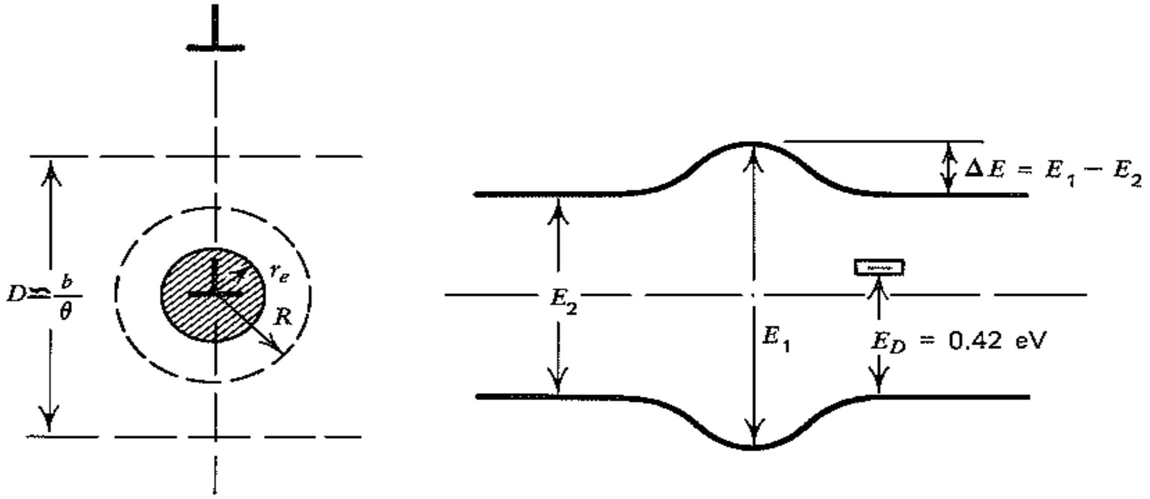

Figure 2.5 Electronic energy level of an edge dislocation and band scheme (Matare, 1970b).

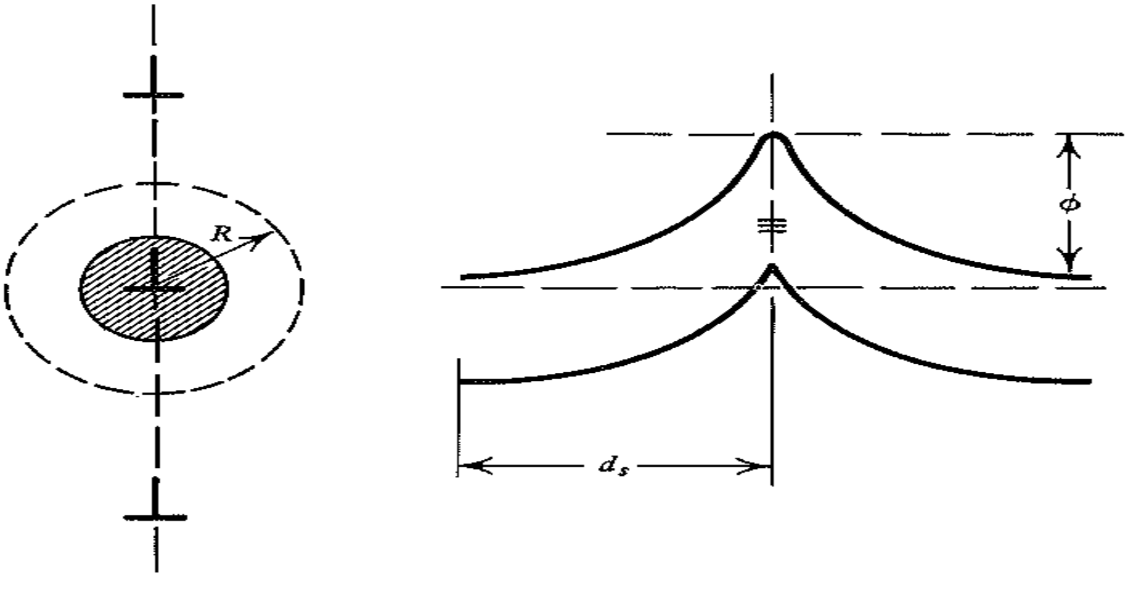

Figure 2.6 Dislocation barrier layer and resulting space charge (Matare, 1970b).

If the distance between the individual sites is larger than the lattice constant, alternating bandgap widening and narrowing occurs as shown in Figures 2.5. 2.6 and 2.7.

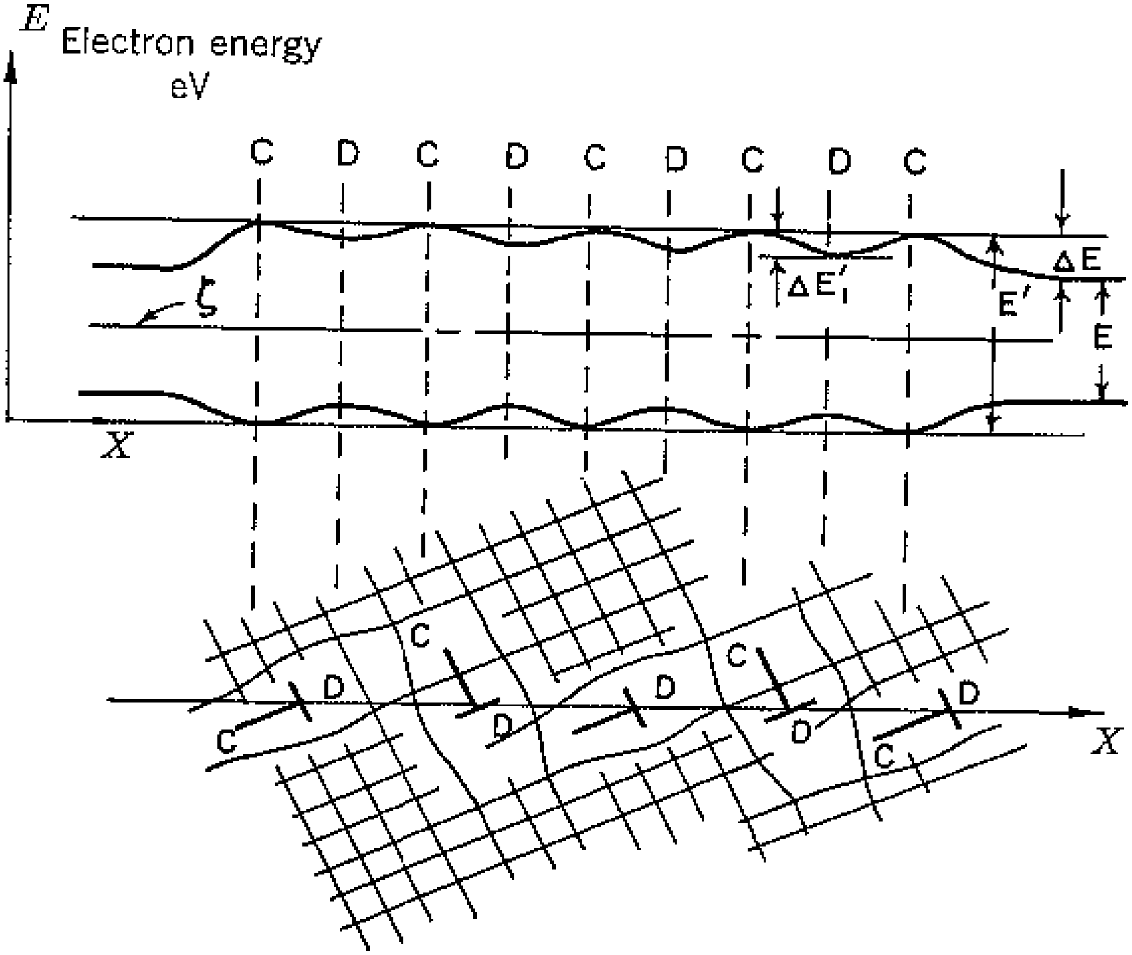

Figure 2.7 Compression and dilation influence on gap (Matare, 1970b).

In p-type crystals there exist p+ behavior of the dislocations and thus a formation of a space charge region. Similarly in n-type crystals there exist n+ behavior of the dislocations (Matare, 1970c). The mobility is direction-dependent, smaller when perpendicular to the dislocation pipe, and larger along the pipe. W.T. Read (Read, 1954) makes a distinction between parallel and perpendicular current flow (Figure 2.8).

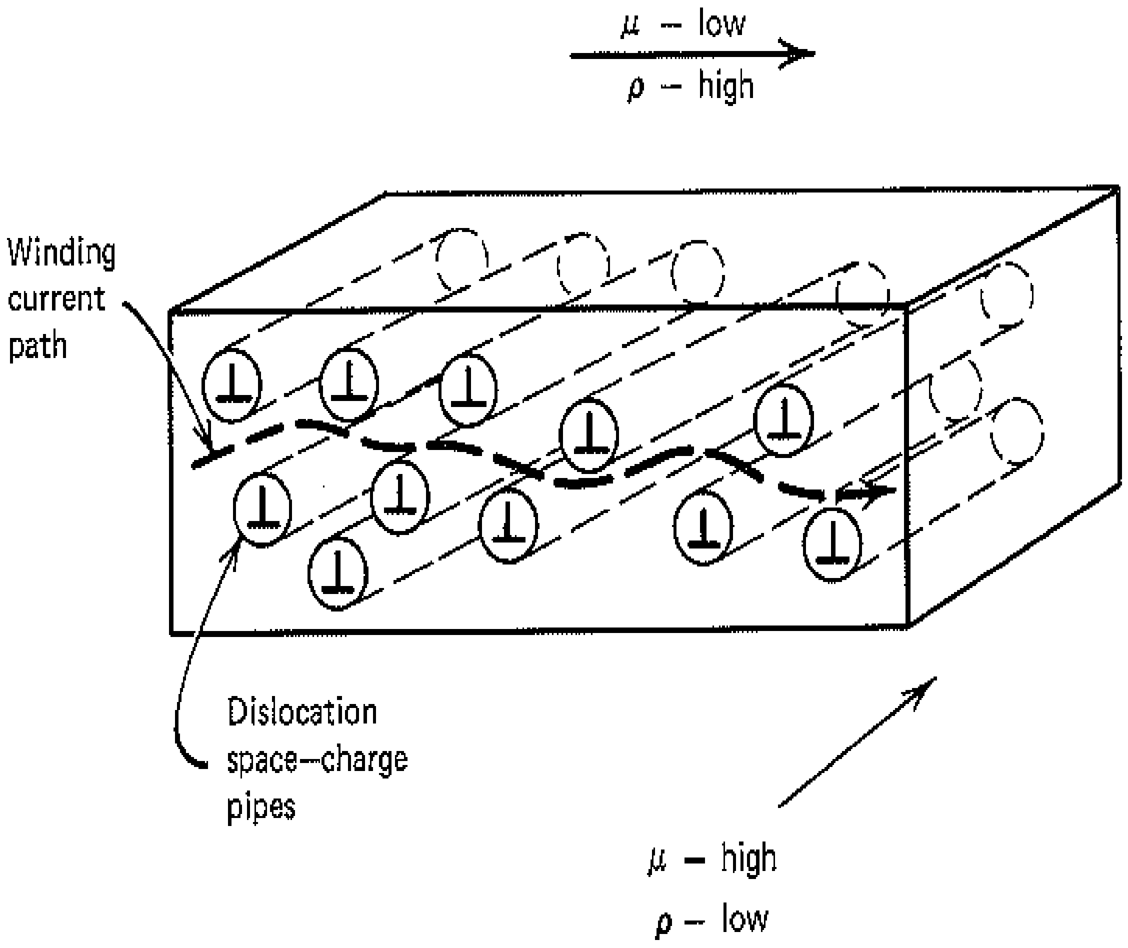

Figure 2.8 Current flow in a crystal with dislocation along one major axis (Matare, 1970c).

In screw dislocations the strain is mostly pure shear, hence the atoms are represented by undisturbed cubes slipped over one another. Two twisted seed crystals with a lattice translation vector as a slip vector form a screw boundary (Figure 2.9). Since the energy of the screw dislocation is smaller than that of the edge dislocation, the lattice disturbance due to strain and the resultant band change are similar.

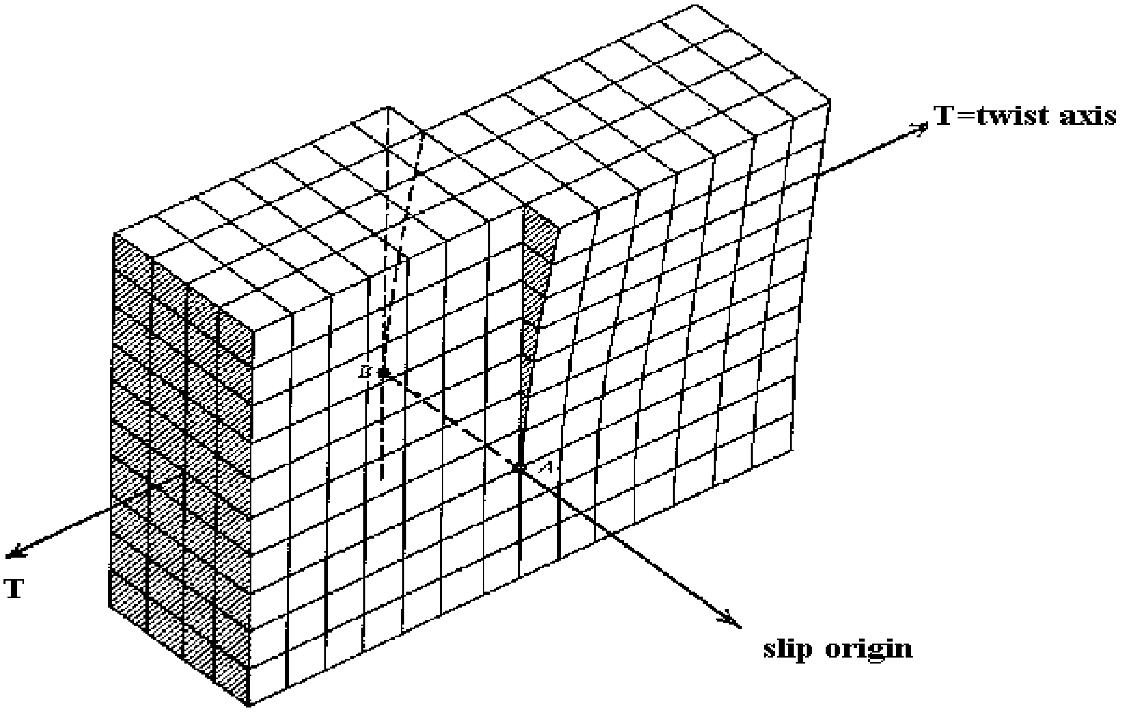

Figure 2.9 Two twisted crystals with slip vector = lattice translation vector (Matare, 1970b).

An ideal screw dislocation, however does not show the special aspect of the disrupted bond with its acceptor (donor) level and the consequent buildup of a space charge. Figure 2.10 (a) shows the model of the ideal screw dislocation and its electronic band picture. Figure 2.10 (b) shows, for comparison, the disturbed screw dislocation, which does not lie in a single plane parallel to the slip vector. In this case the boundary of the slipped area is an edge dislocation. Since slip occurs preferentially on densely-packed crystallographic planes, the growth of screw dislocation from twisted seeds is subjected to forces that tend to divert the slip plane into lower energy positions, thereby creating edge dislocations.

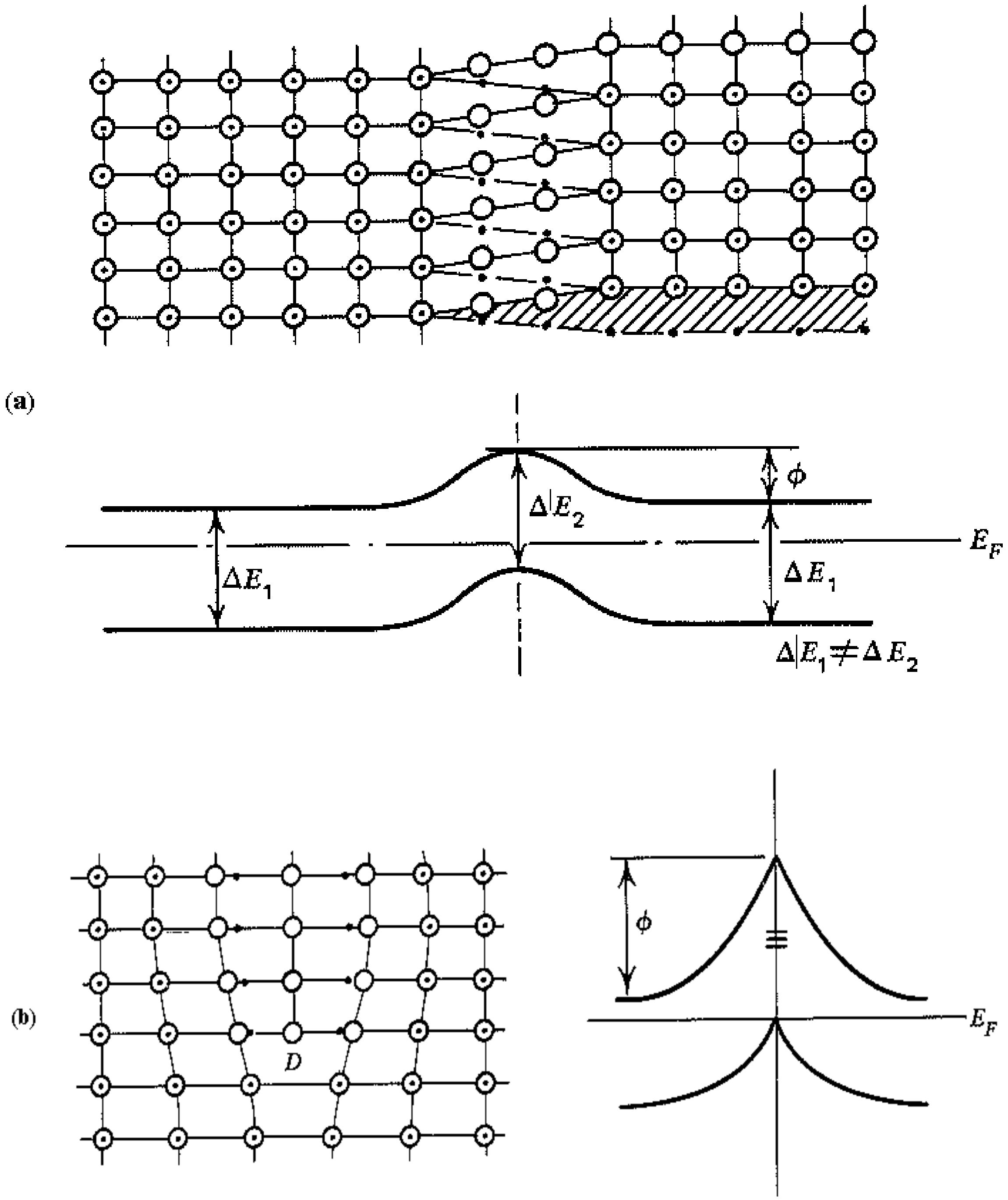

Figure 2.10 (a) Model of an ideal screw dislocation and band scheme, and (b) Disturbed screw dislocation (Matare, 1970b).

2.2.4 Dislocations in Junction Devices in General

There are effects of dislocations in the properties of bulk crystals like resistivity, mobility, lifetime, etc. (Pauls, 1993). In general, dislocations do not add free electrons to the amount of free carriers available but they actually withdraw free electrons from the free carrier pool to form a space charge. The radial resistivity gradient in Czochralski-grown crystals can be kept smaller when such normal dislocation density is counted and compared with dislocation-free crystals (Matare, 1970d). On one hand, decreased device size itself improves the chances of high performance but the devices like solar cells processed on a large area has significant effect on dislocations.

A large amount of pictures of crystals before and after processing by typical microelectronic production steps show that dislocations are generated by the following: (1) Surface damage, (2) Thermal oxidation, (3) Diffusion of impurities like phosphorous and boron, (4) Diffusion generated strain in adjacent areas not subject to the diffusion, (5) Ion implantation, (6) Alloying, and (7) Metal deposition.

The dislocation arrays behave like a degenerate piece of semiconductor, the degeneracy being a function of the lateral field across the space charge domain. A dislocation pipe situated between a p-n junction and a contact area acts in two ways:

1. It carries excess current with increased field between the p-type layer and the contact.

2. The amount of current is dependent on the lateral field across the space charge and increases for increasing lateral field.

This situation can be the main cause of difficulty in junction devices, for example, in a case where the dislocation runs across p-n junction space charge layer (Figure 2.11).

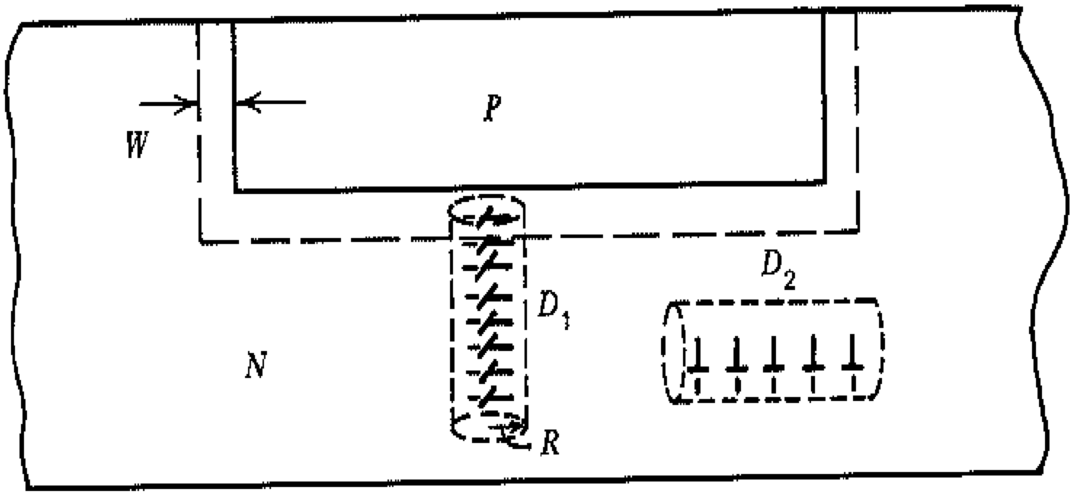

Figure 2.11 Dislocation D_1, as shunt in a p-n junction, and Dislocation D_2 which is inactive (Matare, 1970c).

The edge dislocations form a space-charge pipe in the p-n junction as shown in Figure 2.12. Actually, the space-charge pipe comprises hundreds of lattice points but is reduced here. The application of a field of the sign indicated biases one side of the n-p-n structure in the forward direction, limiting the space-charge, depressing the barrier, and decreasing the number of carriers generated by electron impact. The high carrier generation-recombination rate enhances the sample current it draws.

A dislocation pipe acts as a highly conducting path because of wave function overlap but establishes blocking properties in a direction perpendicular to the pipe. Therefore the orientation of the dislocation is of importance for its behavior in depletion layers where its influence is mostly felt. The high field region in all junction devices or the intrinsic layers is most sensitive in this respect. If the array is located (a) in the direction of the field lines between the n- and p- layers, it establishes an efficient breakdown region and forms the origin for excitation (case a in Figure 2.13).

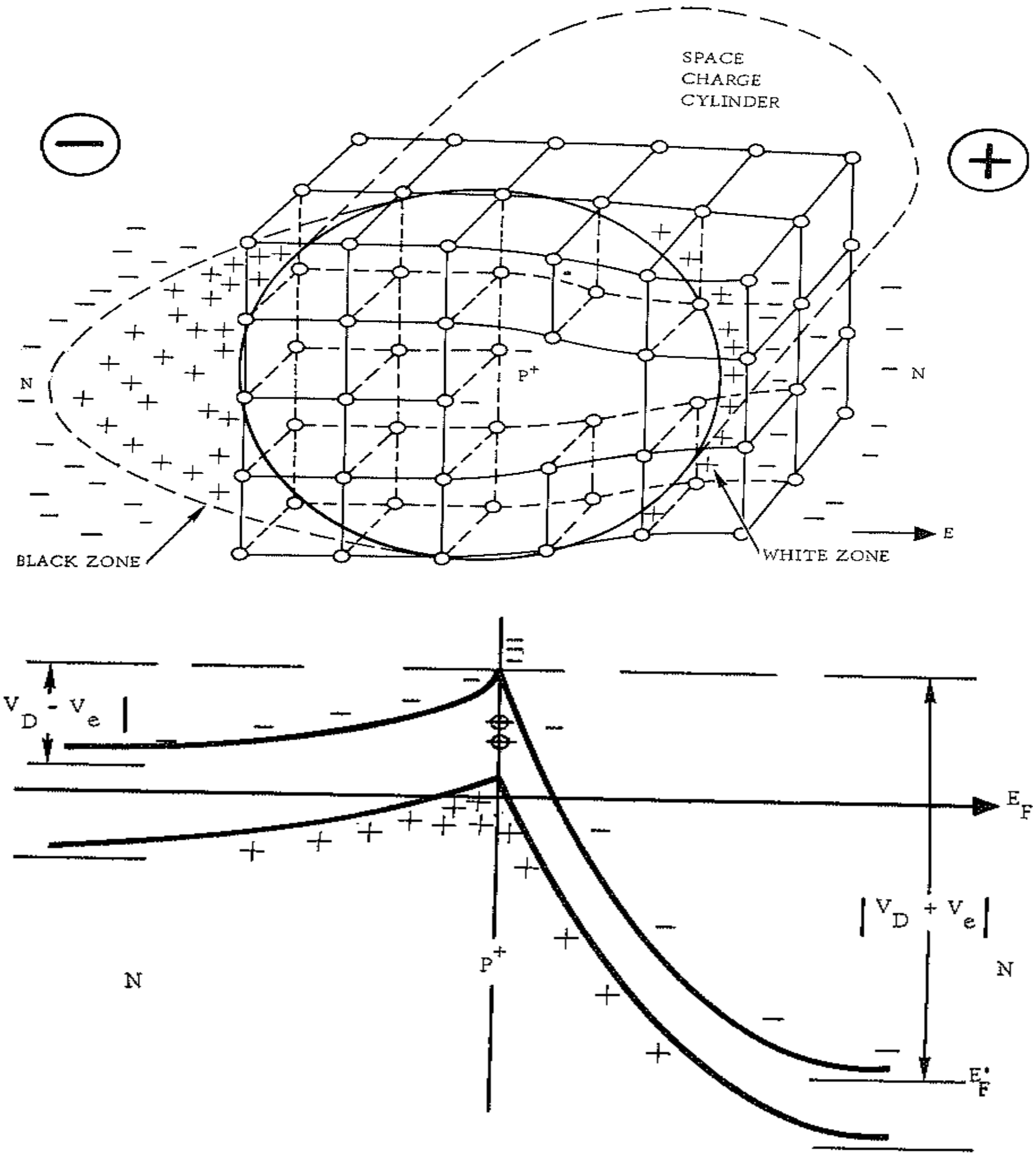

Figure 2.12 Edge dislocation space charge pipe in the cubic case and its equivalent band structure (Matare, 1970c).

If the dislocation is running parallel to the p-n layer, it may not interfere with the junction properties, but its space-charge widens considerably because of the bias effect (case b in Figure 2.13). In case a (Figure 2.13), a high current density also leads to local heating effects and eventually to a destruction of the crystal properties like segregation, second phase formation, melting etc.

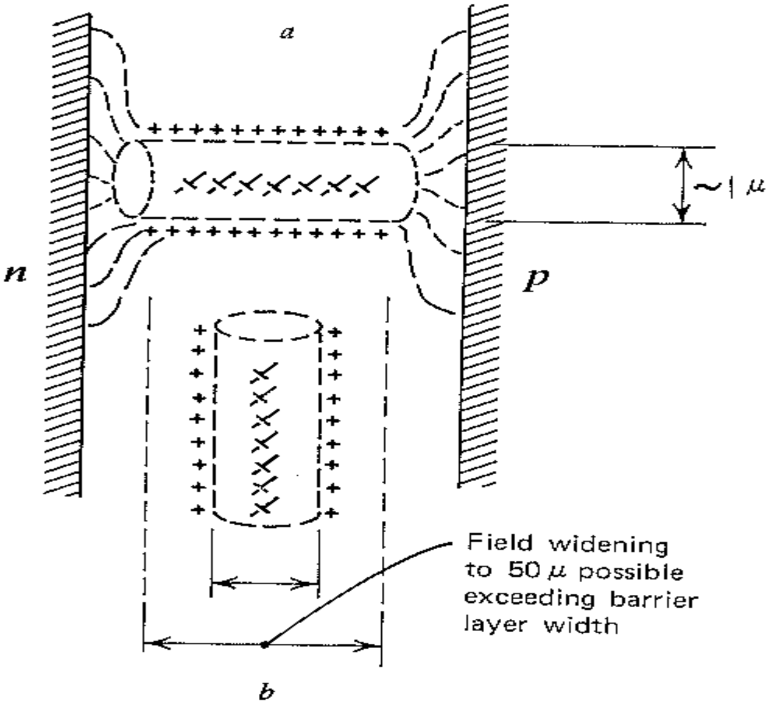

Figure 2.13 Dislocation arrays with a space-charge pipe in two positions within the barrier layer region (Matare, 1970d).

Process induced dislocations have the same effects as in-grown defects when they are located within the high field regions of the devices. But this does not mean that the original wafer perfection is less important. Interface dislocations change the band structure as shown in Figure 2.14. The recombination flux through the interface decreases the efficiency.

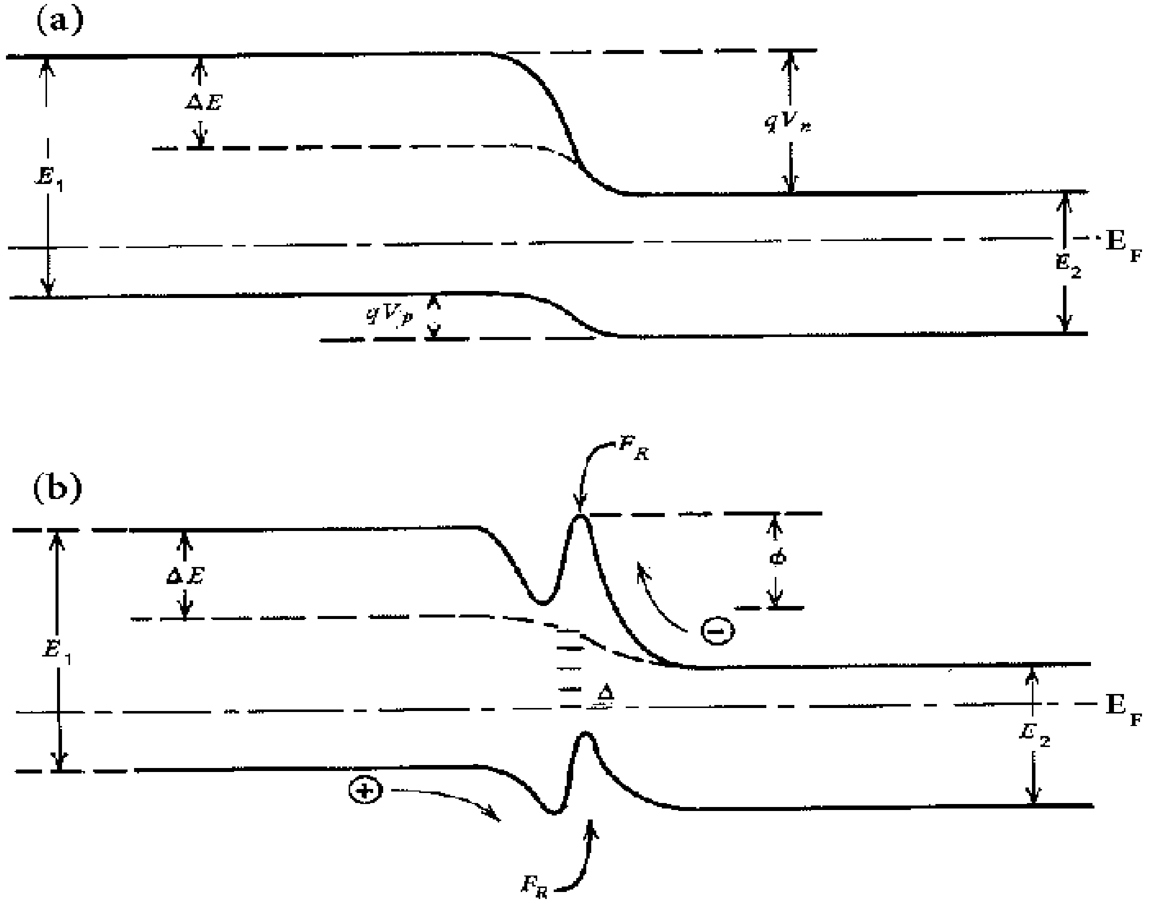

Figure 2.14 Band structure (a) with no interface dislocations, and (b) with interface dislocations (Oldham, 1964).

2.3 Application of Defect Study Including Dislocations in Different Projects on Mc-Si Solar Cells

Earlier in this chapter it was shown that the dislocation has adverse effect on devices as it reduces the lifetime, mobility, resistivity etc. The effect of dislocations was observed on different projects in solar cells, the details of which are mentioned in this section.

2.3.1 Comparison of Low and High Efficiency Cell

Cells and wafers provided by different vendors were characterized optically and electrically. J-V measurements of the cells were taken to get the cell parameters from a commercially available solar simulator under the spectral irradiance of 1000.0 W/m^2 at room temperature. The area of tested cells was 243.36 cm^2, i.e. 6” X 6”. Dark Lock-in thermography (DLIT) method was used to see the distribution of dislocations in multi crystalline silicon. The details of the instrument (www.thermosensorik.com) are available in literature and published by O. Breitenstein (Lanenkamp, 2002), (Breitenstein, 2003). Lock-in thermography (LIT) is a standard technique use to detect shunts and hot spots. Shunts are the regions of high dislocation density. LIT images were taken in multi crystalline silicon cells at different bias voltages to see the regions of dislocations and impurity precipitates. Under high reverse bias, high dislocation density regions show the large thermal signal due to the high power dissipation in those regions.

Three cells, namely cells A, B and C made up of mc-Si and having different distribution of defects were characterized electrically. After calibrating the light intensity from a standard reference cell with respect to one sun, the J-V measurement of cells A, B and C were done under dark and illuminated (AM1.5) conditions. Dark and illuminated J-V measurements of cells A, B and C are shown in Figure 2.15 and their corresponding cell parameter values are given in Table 2.1. Cell A has higher efficiency and higher values of cell parameters than cell B and cell C. The reason for this is described when lumped parameters (like saturation currents, series resistance and shunt resistance) of these three cells were calculated by fitting the dark J-V curves using the two diode model.

Table 2.1 Electrical Parameters at 25^{O}C (Area: 243.36 cm^2)

Solar Cell	**V_{oc} (V)**	**J_{sc} (mA/cm^2)**	**FF**	**η (%)**
Cell A	0.6196	34.79	72.8	15.72
Cell B	0.6127	34.47	70.5	14.88
Cell C	0.6046	33.15	67.6	13.56

The fitting results of cells A, B and C are shown in Figure 2.16 and their corresponding lumped parameter values are shown in Table 2.2 The series and shunt resistances of the cell influence fill factor, maximum power point, and efficiency of the cell (Nielsen, 1982), (Pysch, 2007), (Dyk, 2004), (Kurobe, 2005). In a good silicon solar cell the series resistance must be low and shunt resistance must be high. Cell A has lower series resistance, higher shunt resistance and lower saturation currents than cell B and cell C, which makes it the highest efficiency cell. The high values of J_{02} in multi crystalline cells A, B and C are due to the recombination in space charge region associated with defects.

Table 2.2 Parameters Obtained from Dark J-V Characteristics

Solar Cell	**R_s (mΩ)**	**R_{sh} (kΩ)**	**J_{01}(mA/cm^2)**	**J_{02}(mA/cm^2)**
Cell A	4.021658	14.796350	6.61E-10	3.29E-05
Cell B	4.350242	11.002230	1.04E-09	3.51E-05
Cell C	4.510488	0.230615	1.01E-09	4.93E-05

Cells A, B and C have different efficiencies because of the different distribution of defects in the bulk. In multi crystalline silicon dislocations are randomly distributed and form a region of increased dark forward current. These regions are called shunts. O. Breitenstein (Breitenstein, 2004) has described mainly two types of shunts: process-induced shunts and material-induced shunts.

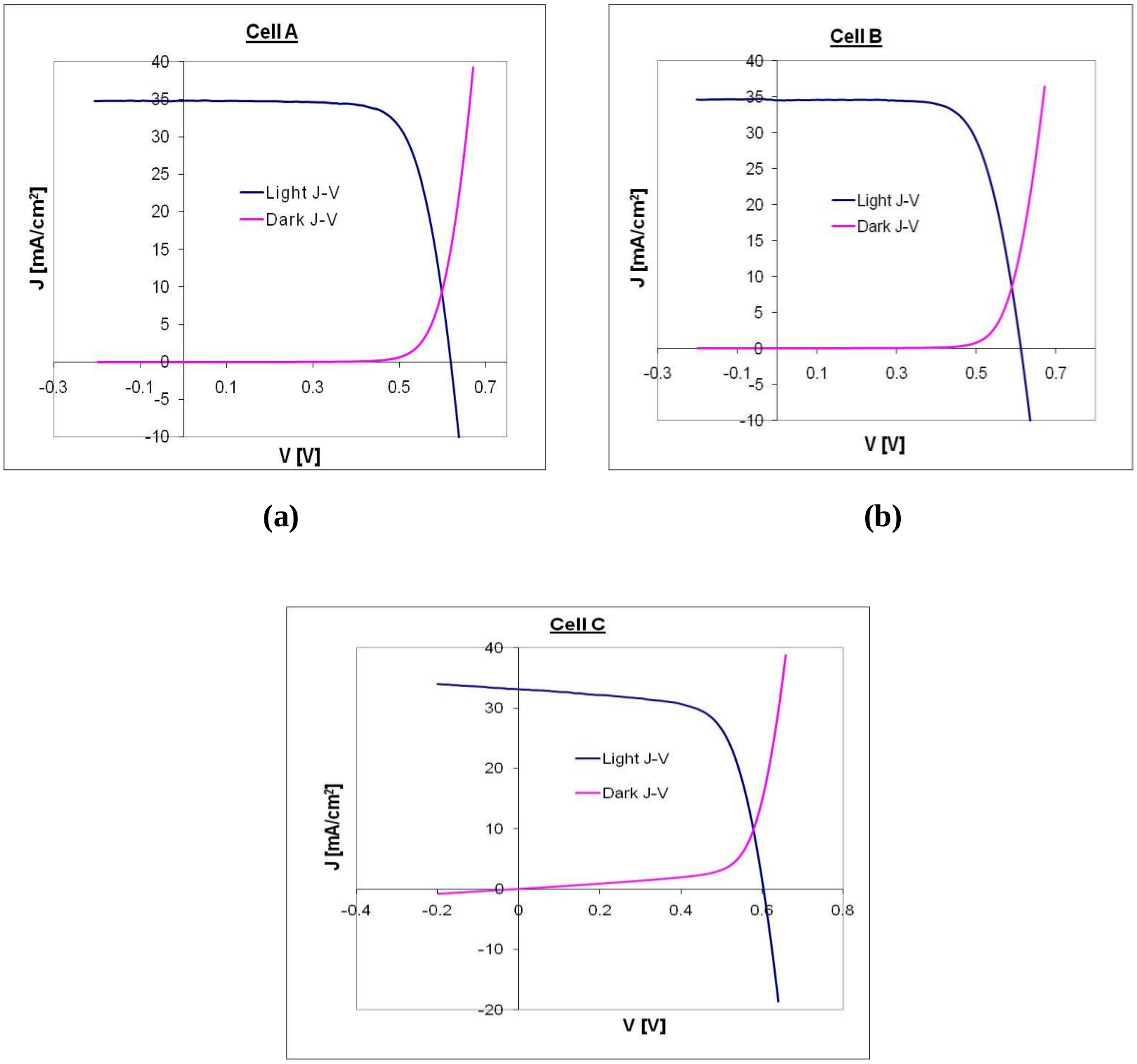

(a)

(b)

(c)

Figure 2.15 Dark and illuminated characteristics of (a) Cell A, (b) Cell B and (c) Cell C.

Process-induced shunts can be minimized but it is hard to remove material-induced shunts. In other words shunts are the regions of high defect density.

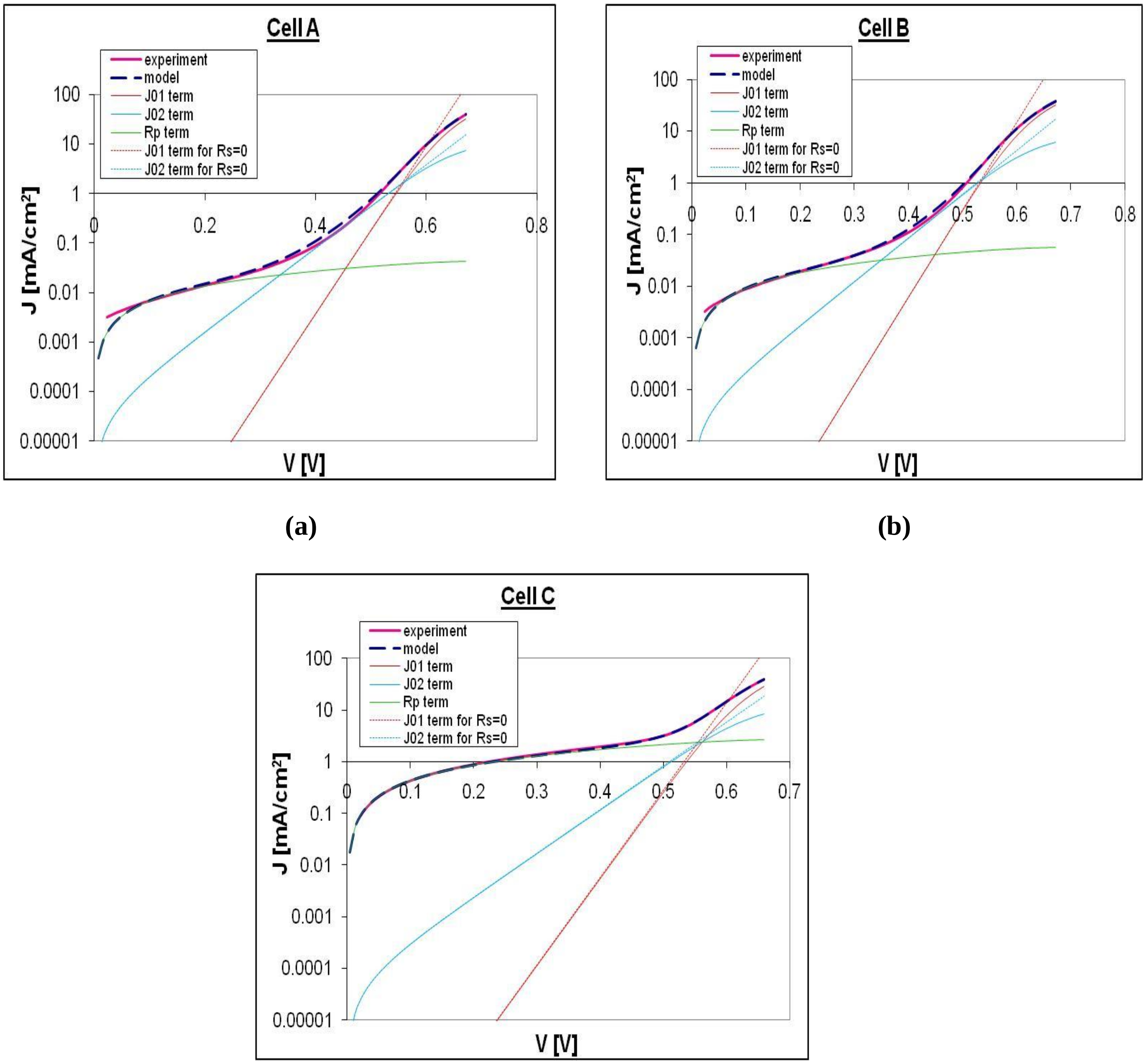

(a) (b)

(c)

Figure 2.16 Illustration of dark log J-V characteristics (a) Cell A, (b) Cell B and (c) Cell C.

By applying high reverse bias, electric field effects are enhanced in high dislocation density regions that behave as sites for localized avalanche breakdown. In these local regions high power is dissipated under high reverse bias because of increased dark reverse current which results in local excessive heating of the cells. These regions are called hot spots which can be seen from Dark Lock-in Thermography (DLIT). DLIT is used to see defects. DLIT images of cells A, B and C was taken at -5V (as shown in Figure 2.17) and -10V (as shown in Figure 2.18).

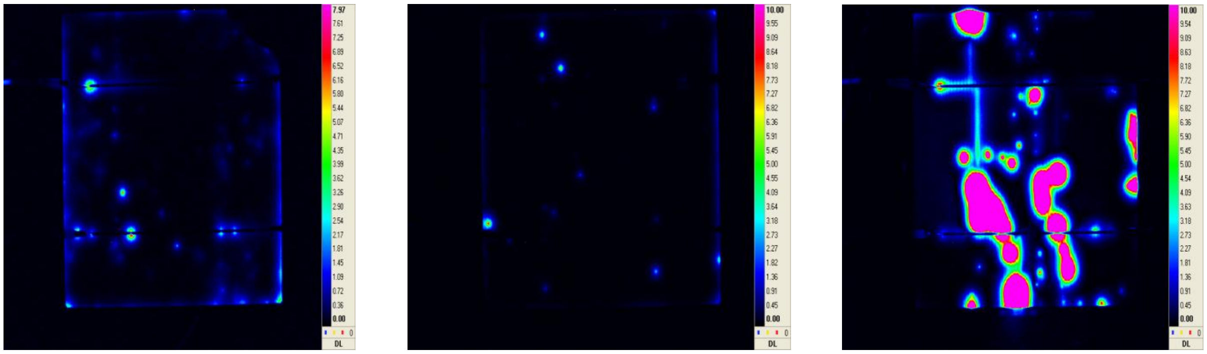

(a) **(b)** **(c)**

Figure 2.17 Dark Lock-in Thermography at -5V, 2.3 Hz of (a) Cell A, (b) Cell B and (c) Cell C.

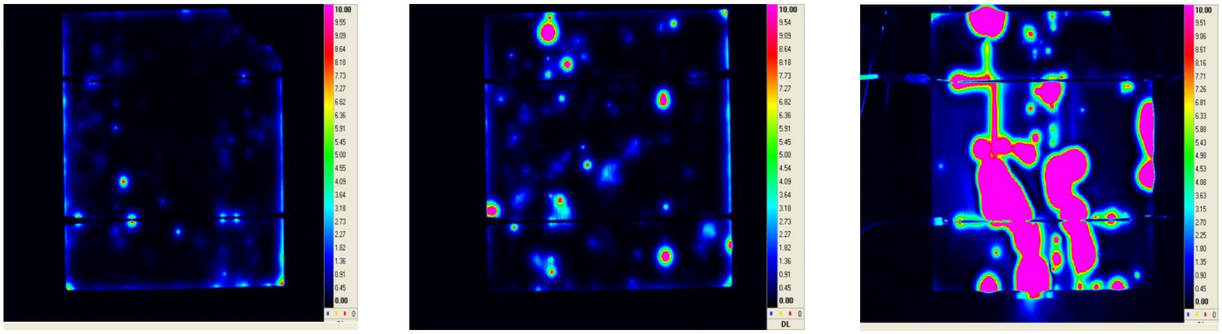

(a) **(b)** **(c)**

Figure 2.18 Dark Lock-in Thermography at -10V, 2.3 Hz of (a) Cell A, (b) Cell B and (c) Cell C.

From Figures 2.17 and 2.18 it is clearly seen that there is a high distribution of defects in cell C that is responsible for its lower efficiency than cell A and cell B. When the voltage is increased from 5V to 10 V in reverse bias, local heating of high dislocation density regions increases due to the higher power dissipation at higher voltages in reverse bias. In Figure 2.18a and 2.18b the pink circles and other small light circles correspond to etch pits. When the impurities get precipitated at dislocation sites the defects clump together in those regions and form defect clusters, which are shown as pink region in Figure 2.18c. The characterization of defect clusters has been described by B.L. Sopori (Sopori, 2009b). This confirms that cell A must have the highest efficiency because of the lowest dislocation density.

2.3.2 Dislocation Propagation in Mc-Si

Grains of certain orientations with the lowest yield stress undergo plastic deformation producing local dislocation regions and causing the thermal stresses to diminish (Chen, 2008), (Sopori, 2009). As a result, other grains of higher yield stress do not form dislocations or have very low dislocation density. This causes formation of dislocation clusters in the mc-Si (Sopori, 2009). Unfortunately, dislocations multiply (and some of them also annihilate) causing the dislocations to spread from the initial grains into the adjacent regions. Dislocation clusters are decorated with precipitated metallic impurities, which are not gettered or passivated during solar cell processing. Thus, dislocations have a very strong influence on the solar cell performance. It is important for wafer versus brick versus ingot suppliers to know how the dislocations are propagated in the ingot and how they influence the solar cell performance (Sopori, 2010).

Experimental studies were also performed to investigate the influence of defects in mc-Si wafers on solar cell performance and to study changes associated with defect propagation within a brick of mc-Si. Selected wafers (156-mm-size) were characterize which taken from mc-Si bricks from different parts of ingots. These selected wafers were then processed into solar cells. The cell data from current-voltage characteristics, light-beam-induced current, electroluminescence (EL), and hot-spot thermal image maps were analyzed.

Figure 2.19 shows an example of LBIC, dislocation, and EL maps for wafers and cells taken from top, middle, and bottom of a brick. The cell parameters (V_{oc}, J_{sc}, and FF), average LBIC current (in A/W), and defect densities are listed in Tables 2.3 and 2.4. It is seen that there is a progressive degradation of V_{oc} and J_{sc} for cells from top to bottom.

Table 2.3 Solar Cell Parameters Measured at 25^0C (Sopori, 2010)

Solar Cell	**V_{oc} [V]**	**J_{sc} [mA/cm^2]**	**LBIC @ 980 nm [A/W]**	**LBIC @ 633 nm [A/W]**	**FF [%]**	**η [%]**	**Defect density [X 10^5/cm^2]**
TOP	0.6217	32.89+0.035	0.500	0.400	76.8	15.7	0.78
MIDDLE	0.6209	33.0+0.035	0.504	0.416	77.4	15.9	0.64
BOTTOM	0.6198	33.0+0.035	0.496	0.415	77.1	15.8	1.52

Table 2.4 Parameters Obtained from Dark I-V Characteristics (Sopori, 2010)

Solar Cell	**R_s (mΩ)**	**R_{sh} (kΩ)**	**J_{01}(mA/cm^2)**	**J_{02}(mA/cm^2)**
TOP	2.48	13.2	7.5E-10	3.1E-05
MIDDLE	2.41	17.2	8.51E-10	2.6E-05
BOTTOM	2.34	13.4	8.39E-10	2.9E-05

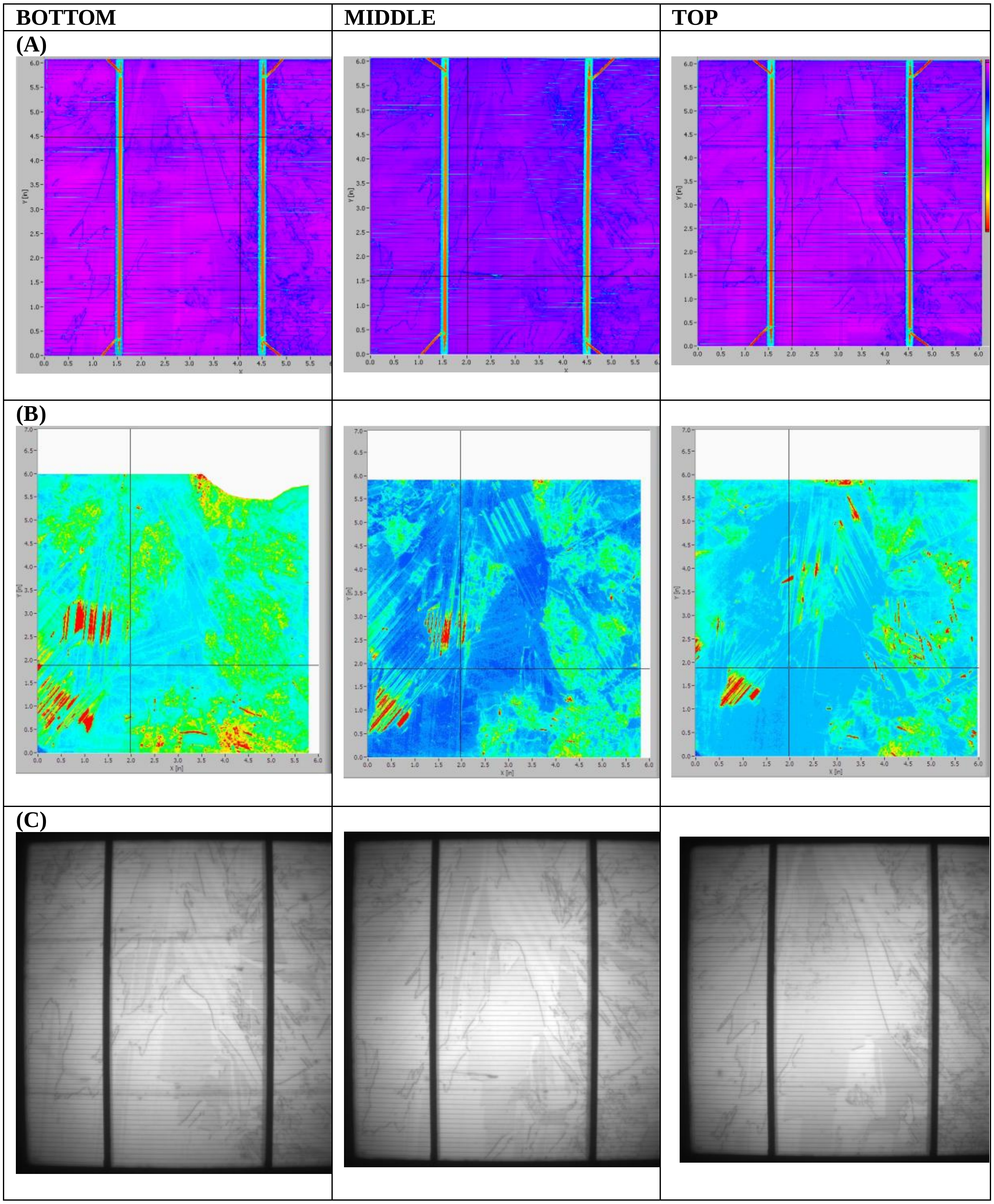

Figure 2.19 Maps of 980nm LBIC (A), defect density (B) and electro-luminescence (C) for three wafers from bottom, middle and top part of an ingot (Sopori, 2010).

CHAPTER 3

DISCUSSION OF THE MODEL OF A SILICON MESA DIODE

3.1 Introduction

In crystalline silicon there are several defects that exist such as grain boundaries, dislocations, defect clusters etc. The effect of grain boundaries is negligible in the performance of solar cells because of the use of large grain size material by solar industries in present technology (Ghitani, 1989), (Halder, 1983). Defect cluster regions can be assumed as regions of high dislocation densities (Sopori, 2009a). Among various defects, dislocations and impurity precipitates are the most harmful in the performance of mc-Si solar cell. Dislocations have adverse effects on cell parameters such as short-circuit current density (J_{sc}) and spectral response (S.R) in polycrystalline silicon solar cells.

The three-dimensional continuity equation of the minority carriers with the effect of dislocations has been solved by assuming the boundary condition of the front surface recombination velocity on the quasi neutral region of the n side and back surface recombination velocity on the quasi neutral region of the p-side. The dislocation was considered to be a space charge cylinder that extends perpendicular from the front to back surface of the n^+-p junction. In this work the influence of front and back surface recombination velocities at the front and back surfaces of the n^+-p junction silicon solar cells have been computed, respectively, on the spectral response and short-circuit current density using identical dislocation models.

3.1.1 Assumptions Used in Suggested Model

The three-dimensional continuity equation of the minority carriers in a solar cell which has a periodic array of dislocations and with front and back surface recombination was solved. Each dislocation was considered to be a space charge cylinder perpendicular to the surface and extending through the entire cell.

The suggested model assumes the uniform distribution of dislocations as shown in Figure 3.1. Dislocations have their influence in all three dimensions. The thickness of the cell is d. The influence of defects exists in the horizontal direction because of recombination activity. The influence of defects exists in the vertical direction because of dislocation density as well as front and back surface recombination.

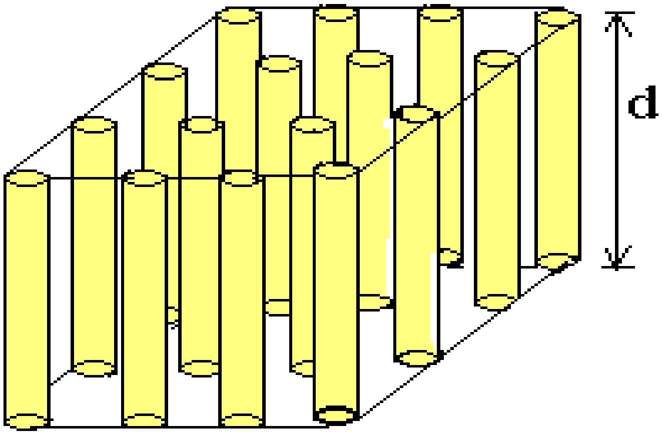

Figure 3.1 Three-dimensional view of the distribution of dislocations.

In the model a unit cell surrounded by four dislocations was considered. The dislocations are located on the corners of the cube as shown in Figure 3.2 (a).

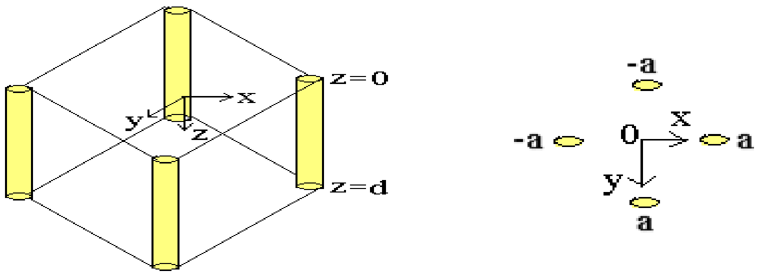

(a) **(b)**

Figure 3.2 (a) The distribution of dislocations in a unit cell; (b) Front view of the distribution of dislocations in a unit cell at z=0.

Figure 3.2 (b) shows the front view of the distribution of dislocations at the z=0 plane which is the front surface of the cell. The carriers can recombine at a dislocation from all three dimensions. In this work the calculations were done under the following assumptions:

(i) The contribution of the emitter was considered.

(ii) Shunt and series resistance effects were neglected.

(iii) The grains contained a regular array of homogenously recombining dislocations that were perpendicular to the junction area.

(iv) The dislocation was considered to be a space charge cylinder that extends perpendicular from the front to back surface of the n^+-p junction.

(v) The effect of front and back surface recombination velocity cannot be neglected because the current mc-Si technology provides surface passivation by SiN:H on the front surface and very effective back surface field on the back surface.

(vi) The effect of recombination activity at dislocations was considered.

(vii) The diameter of the space charge region around cylindrical dislocation was smaller than the distance between two dislocations.

All these calculations were done at the cell thickness of 200 µm and the term S_d was varied from 10^2- 10^6 cm/sec.

The distance between two dislocations is 2a. The dislocation density is given by

$$N_d=1/\pi a^2 \tag{3.1}$$

In the calculations the dislocation density was varied from $10^2 – 10^6$ /cm^2, and front and back surface recombination velocities were varied from 10^2 cm/sec to infinity.

3.1.2 Comparison of Suggested Model with Other Dislocation Models

The effect of dislocations on the performance of mc-Si solar cells has been studied by several groups (Hartman, 2008), (Cousins, 2006), (Kieliba, 2006) but still no direct relation between dislocation density and cell parameters has been established even though some correlation under the assumption of uniform distribution of dislocations (Opdorp, 1977), (Lax, 1981), (Yamaguchi, 1986), (Ghitani, 1989a), (Donolato, 1993) has been reported. The effect of front and back surface recombination velocity was, however, neglected in these dislocation models. In other words, the surface recombination velocities in the above models assumed to be infinity where all the carriers that arrive at the surface, completely recombine. This can cause a significant error, particularly because current mc-Si technology provides surface passivation by SiN:H and very effective back surface fields.

3.2 Continuity Equation of Minority Carriers

A continuity equation in physics is a differential equation that describes the transport of a conserved quantity. Since mass, energy, momentum, electric charge and other natural quantities are each conserved under its own appropriate condition, a vast variety of physics may be described with continuity equations. All the examples of continuity equations express that: the total amount (of the conserved quantity) inside any region can only change by the amount that passes in or out of the region through the boundary. Any continuity equation can be expressed in an "integral form" (in terms of a flux integral), which applies to any finite region, or in a "differential form" (in terms of the divergence operator) which applies at a point.

In a semiconductor, both electrons and holes can enter a volume at one end and leaves at other end. Carriers may also pile up or disappear in the volume. Therefore their number leaving at any time may not be the same as the number entering. The continuity equation takes into account all the sources and sinks of electrons and holes (Shockley, 1962), (Anderson, 2005).

In the differential volume, the rate of increase in the conduction band electron concentration is given by

$$\frac{\partial \Delta n}{\partial t} dx = -\frac{\partial F_n}{\partial x} dx + (G_n - R_n) dx \tag{3.2}$$

where G_n is the electron generation rate and R_n is the electron recombination rate (number of carriers per unit volume per unit time). The term $(\partial F_n / \partial x)\, dx$ represents the difference in electron flux at either end of the region dx. Since the electron flux density is given by

$$F_n = -(J_n / q) \tag{3.3}$$

where J_n is the electron current density is given by

$$J_n = qD_n \frac{\partial n}{\partial x} \tag{3.4}$$

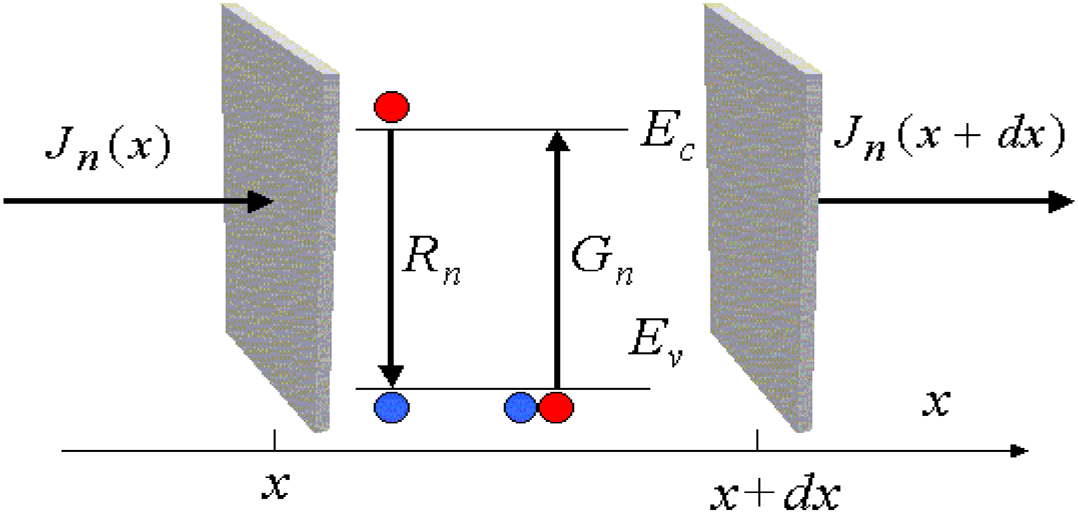

Figure 3.3 Geometry for determining the continuity equation of electrons. The rate at which electrons accumulate in the incremental volume depends on the incoming and outgoing currents as well as the recombination and generation within the region dx (website: ecee.colorado.edu).

In the differential volume, the rate of increase in the conduction band electron concentration is given by

$$\frac{\partial \Delta n}{\partial t} dx = -\frac{\partial F_n}{\partial x} dx + (G_n - R_n) dx \tag{3.5}$$

where G_n is the electron generation rate and R_n is the electron recombination rate (number of carriers per unit volume per unit time). The term ($\partial F_n / \partial x$) dx represents the difference in electron flux at either end of the region dx. Since the electron flux density is given by

$$F_n = -(J_n / q) \tag{3.6}$$

where J_n is the electron current density is given by

$$J_n = qD_n \frac{\partial n}{\partial x} \tag{3.7}$$

So the continuity for electrons will become

$$\frac{\partial \Delta n}{\partial t} = D_n \frac{\partial^2 \Delta n}{\partial x^2} + (G_n - R_n) \tag{3.8}$$

$$R_n = \Delta n / \tau_n \tag{3.9}$$

Similarly the continuity equation for hole is given by

$$\frac{\partial \Delta p}{\partial t} = -D_p \frac{\partial^2 \Delta p}{\partial x^2} + \left(G_p - R_p\right) \tag{3.10}$$

In the steady state $\frac{\partial \Delta n}{\partial t} = \frac{\partial \Delta p}{\partial t} = 0$, because the electron and hole concentrations do not change with time.

3.3 Introduction of Green's function

It is important to understand the Green's function as it is used to solve the system of equations. The theoretical approach involves a solution of the three dimensional continuity equation by Green's function method bounded by boundary conditions.

In mathematics, a Green's function is a type of function used to solve inhomogeneous differential equations subject to specific initial conditions or boundary conditions. The term is also used in physics, specifically in quantum field theory, electrodynamics and statistical field theory, to refer to various types of correlation functions, even those that do not fit the mathematical definition.

Let *L* be the Sturm–Liouville (McQuarrie, 2003) operator, a linear differential operator of the form

$$L = \frac{d}{dx}\left[p(x)\frac{d}{dx}\right] + q(x) \tag{3.11}$$

Let D be the boundary condition operator

$$\mathrm{Du} = \begin{cases} \alpha_1 u'(0) + \beta_1 u(0) \\ \alpha_2 u'(l) + \beta_2 u(l) \end{cases} \tag{3.12}$$

Let f(x) be a continous function in [0,1].

$$\mathrm{Lu} = \mathrm{f} \tag{3.13}$$

$$\mathrm{Du} = 0 \tag{3.14}$$

$$\mathrm{u(x)} = \int_0^1 \mathrm{f(s)G(x,s)ds} \tag{3.15}$$

where $G(x,s)$ is the Green's function satisfying the following conditions:

1. $\mathrm{G(x,s)}$ is the continous function in x,

2. For s≠0, $\mathrm{DG(x,s)} = 0,$

3. $G'(s+0,s) - G'(s-0,s) = 1/p(s)$

4. Symmetry: $G(x,s) = G(s,x)$

3.4 Current Density Calculations in the Light Case

The solar cell was considered as a p-n junction for its modeling. The dislocations are uniformly distributed and extend from top to bottom of p-n junction as shown in Figure 3.4.

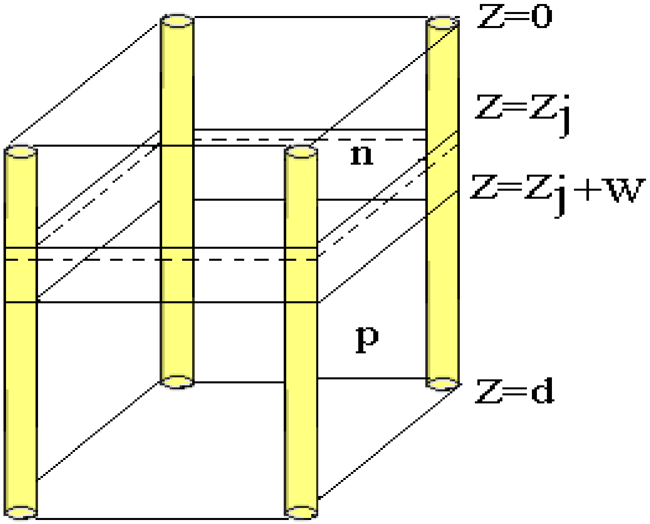

Figure 3.4 Schematic view of a n-p junction.

For a multicrystalline n-p junction cell the continuity needs to be solved in the n and p regions. Here the assumptions are made that the recombination velocity is the same at all points on the boundaries and that the density change is occurring at the boundaries in an analogous fashion to that at the surfaces of the junction. Green's function method is used to obtain the solution of the continuity equations in the n and p regions.

3.4.1 Derivation of the Current Equations in the N-Region

The continuity equation to be solved in the n-region of the cell is a partial differential equation of the form (Halder, 1983):

$$\nabla^2(p_n - p_{n0}) - (p_n - p_{n0})/L_p^2 = -\frac{\alpha F(1-R)\, e^{-\alpha Z}}{D_p} \tag{3.16}$$

The right hand side of Equation (3.16) is the generation rate and the boundary conditions of this upper n-region are:

$$\frac{\partial(p_n - p_{n0})}{\partial z} = \frac{S_1}{D_p}(p_n - p_{n0}) \quad \text{at } Z = 0 \tag{3.17}$$

$$(p_n - p_{n0}) = 0 \quad \text{at } Z = Zj \tag{3.18}$$

$$\frac{\partial(p_n - p_{n0})}{\partial x} = \pm\frac{S_d}{D_p}(p_n - p_{n0}) \quad \text{at } x = \pm\, a \tag{3.19}$$

$$\frac{\partial(p_n - p_{n0})}{\partial y} = \pm\frac{S_d}{D_p}(p_n - p_{n0}) \quad \text{at } y = \pm a \tag{3.20}$$

Green's function method was used to obtain a solution with the above boundary conditions. The hole density may be expressed as:

$$(p_n - p_{n0})(x', y', z') = < G, f > \tag{3.21}$$

where the prime variables represent arbitrary points in the volume. The right hand volume integral is integrated with respect to the unprimed variables x, y and z. G is the symbol for the Green’s function and f is defined as,

$$f = -\frac{\alpha F(1-R)\, e^{-\alpha Z}}{D_p} \tag{3.22}$$

The Green’s function is found by solving the following equation:

$$\nabla^2 G - G/L_p^2 = \delta(x-x')\,\delta(y-y')\,\delta(z-z') \tag{3.23}$$

with the boundary conditions:

$$\frac{\partial G}{\partial z} = \frac{S_1}{D_p} G \quad \text{at } Z=0 \tag{3.24}$$

$$G = 0 \quad \text{at } Z=Z_j \tag{3.25}$$

$$\frac{\partial G}{\partial x} = \pm \frac{S_d}{D_p} G \quad \text{at } x=\pm a \tag{3.26}$$

$$\frac{\partial G}{\partial y} = \pm \frac{S_d}{D_p} G \quad \text{at } y=\pm a \tag{3.27}$$

The solution of Equation (3.23) is expressed by

$$G(x,y,z \vdots x',y',z') = \sum_{m,n}^{\infty} \frac{1}{a^2} \cos(mx)\cos(ny) \text{ X}$$

$$\begin{cases} A \sinh(z/L_2) + B \cosh(z/L_2) & \text{if } z < z' \\ C \sinh(z/L_2) + D \cosh(z/L_2) & \text{if } z > z' \end{cases} \tag{3.28}$$

where $1/L_2^2 = n^2 + m^2 + 1/L_p^2$

The substitution for G in the boundary conditions given by Equations (3.26) and (3.27) leads to

$$ma \tan(ma) = -S_d\, a/D_p \tag{3.29}$$

$$na \tan(na) = -\, S_d\, a/D_p \tag{3.30}$$

The Green's function G is continuous at z' which leads to

$$G\,(z < z') = G(\, z > z') \text{ at } z = z' \tag{3.31}$$

$$\lim_{\epsilon \to 0} \frac{\partial(G(z' + \epsilon) - G\,(z' - \epsilon))}{\partial z} = M_a N_a \cos(mx')\cos(ny') \tag{3.32}$$

where $M_a = m/(ma + \left(\frac{1}{2}\right)\sin(2ma))$ and $N_a = n/(na + \left(\frac{1}{2}\right)\sin(2na))$

The values of A, B, C and D are obtained by solving Equations (3.24), (3.25), (3.31) and (3.32).

This gives $B = M_a\, N_a\, \cos(mx')\cos(ny') \dfrac{[\sinh\left(\frac{Z'}{L_2}\right) - \tanh\left(\frac{Z'}{L_2}\right)\cosh\left(\frac{Z'}{L_2}\right)]}{(\frac{1}{L_2} + \frac{S_1}{D_p}\tanh\,(\frac{Z_j}{L_2})}$ and

$$C = M_a\, N_a\ \cos(mx')\cos(ny')\,\frac{[\frac{S_1 L_2}{D_p}\sinh\left(\frac{Z'}{L_2}\right)+\cosh\left(\frac{Z'}{L_2}\right)]}{[\frac{1}{L_2}+\frac{S_1}{D_p}\tanh\left(\frac{Z_j}{L_2}\right)]}$$

The excess of minority carriers (holes) is given by the volume integral:

$$\delta p\ (x,y,z)\ =\int_0^{Z_j}\int_{-a}^{a}\int_{-a}^{a} G\ f\ dx\ dy\ dz$$

$$= \sum_{m,n}^{\infty}\frac{-4q\alpha F(1-R)M_a N_a \sin(ma)\sin(na)}{mna^2}\left\{A\left[L_2e^{-\alpha z}\cosh\left(\frac{z}{L_2}\right)+\alpha L_2^2e^{-\alpha z}\sinh\left(\frac{z}{L_2}\right)-L_2\right]+ B\left[L_2e^{-\alpha z}\sinh\left(\frac{z}{L_2}\right)+\alpha L_2^2e^{-\alpha z}\cosh\left(\frac{z}{L_2}\right)-\alpha L_2^2\right]+C\left[\ I_{12}-L_2e^{-\alpha z}\cosh\left(\frac{z}{L_2}\right)- \alpha L_2^2e^{-\alpha z}\sinh\left(\frac{z}{L_2}\right)\right]D\left[I_{11}-L_2e^{-\alpha z}\sinh\left(\frac{z}{L_2}\right)- \alpha L_2^2e^{-\alpha z}\cosh\left(\frac{z}{L_2}\right)\right]\right\}\cos(mx)\cos\ (ny)$$

(3.33)

The average photocurrent density at a given wavelength is obtained by

$$J_p(\lambda) = \frac{1}{4a^2}\int_{-a}^{a}\int_{-a}^{a} q\ D_p\left(\frac{\partial \delta p}{\partial z}\right)_{z=z_j}\ dx\ dy$$

$$= \sum_{m,n}^{\infty}\frac{-4q\alpha F(1-R)M_a N_a \sin^2(ma)\sin^2(na)}{m^2n^2a^2(1-\alpha^2L_2^2)[\frac{1}{L_2}+\frac{S_1}{D_p}\tanh\left(\frac{Z_j}{L_2}\right)]}\{\frac{S_1}{D_p}\cosh\left(\frac{Z_j}{L_2}\right)\left[-L_2+I_{12}-\tanh\left(\frac{Z_j}{L_2}\right)I_{11}\right]- \alpha L_2\cosh\left(\frac{Z_j}{L_2}\right)+\tanh\left(\frac{Z_j}{L_2}\right)\sinh\left(\frac{Z_j}{L_2}\right)\left[\frac{S_1 L_2}{D_p}+\alpha L_2-\frac{I_{11}}{L_2}\right]+\frac{I_{12}}{L_2}\sinh\left(\frac{Z_j}{L_2}\right)+\ \alpha e^{-\alpha Z_j}[L_2+ \tanh\left(\frac{Z_j}{L_2}\right)\frac{S_1 L_2^2}{D_p}]\}$$

(3.34)

where

$$I_{11} = L_2 \exp(-\alpha Z_j) \sinh\left(\frac{Z_j}{L_2}\right) + \alpha L_2^2 \exp(-\alpha Z_j) \cosh\left(\frac{Z_j}{L_2}\right) \quad (3.35)$$

$$I_{12} = L_2 \exp(-\alpha Z_j) \cosh\left(\frac{Z_j}{L_2}\right) + \alpha L_2^2 \exp(-\alpha Z_j) \sinh\left(\frac{Z_j}{L_2}\right) \quad (3.36)$$

3.4.2 Derivation of the Current Equations in the Depletion Region

The electric field in the depletion region is high enough that virtually all of the carriers generated are accelerated out of the region before they can recombine, so all contribute to photocurrent. The current can be found in the depletion region by integrating the absorption over the junction width:

$$J_{dr}(\lambda) = \int_{Z_j}^{Z_j+W} q\alpha F_L(z)\,dz \quad (3.37)$$

where the photon flux at a given distance into the material $F_L(z)$ is given by

$$F_L(z) = F\,(1-R)e^{-\alpha z} \quad (3.38)$$

The current density in the depletion region is calculated as

$$J_{dr}(\lambda) = q\,F\,(1-R)\exp(-\alpha Z_j)\,\{1-\exp(-\alpha W)\} \quad (3.39)$$

Surface states cause the photogenerated carriers in the depletion region to have a high probability of recombining at the surface and thus the contribution of this region to the photocurrent is low. Because of the high field in the depletion region, the response time is much faster for carriers generated there than for the carriers generated in the quasi neutral regions.

3.4.3 Derivation of the Current Equations in the P-Region

The continuity equation to be solved in the p-region of the cell is a partial differential equation of the form:

$$\nabla^2(n_p - n_{p0}) - (n_p - n_{p0})/L_n^2 = -\frac{\alpha F(1-R)\, e^{-\alpha Z}}{D_n} \qquad (3.40)$$

where the boundary conditions of this lower p-region are:

$$(n_p - n_{p0}) = 0 \quad \text{at } Z=Z_j+W \qquad (3.41)$$

$$\frac{\partial(n_p - n_{p0})}{\partial z} = -\frac{S_z}{D_n}(n_p - n_{p0}) \quad \text{at } Z=d \qquad (3.42)$$

$$\frac{\partial(n_p - n_{po})}{\partial x} = \pm\frac{S_d}{D_n}(n_p - n_{p0}) \text{ at } x = \mp a \qquad (3.43)$$

$$\frac{\partial(n_p - n_{po})}{\partial y} = \pm\frac{S_d}{D_n}(n_p - n_{p0}) \text{ at } y = \mp a \qquad (3.44)$$

The Green's function is found by solving the following equation:

$$\nabla^2 G - G/L_n^2 = \delta(x-x')\,\delta(y-y')\,\delta(z-z') \quad (3.45)$$

with the boundary conditions

$$G = 0 \text{ at } Z=Zj+W \quad (3.46)$$

$$\frac{\partial G}{\partial z} = -\frac{S_2}{D_n} G \quad \text{at } Z=0 \quad (3.47)$$

$$\frac{\partial G}{\partial x} = \pm\frac{S_d}{D_n} G \quad \text{at } x=\mp a \quad (3.48)$$

$$\frac{\partial G}{\partial y} = \pm\frac{S_d}{D_n} G \quad \text{at } y=\mp a \quad (3.49)$$

The solution of Equation (3.42) is expressed by

$$G(x,y,z \,\vdots\, x',y',z') = \sum_{m,n}^{\infty} \frac{1}{a^2} \cos(mx)\cos(ny) \text{ X}$$

$$\begin{cases} A \sinh(z/L_2) + B \cosh(z/L_2) & \text{if } z < z' \\ C \sinh(z/L_2) + D \cosh(z/L_2) & \text{if } z > z' \end{cases} \quad (3.50)$$

where $1/L_2^2 = n^2 + m^2 + 1/L_n^2$

The substitution for G in the boundary conditions given by Equations (3.48) and (3.49) leads to

$$ma\tan(ma) = S_d\, a/D_p \qquad (3.51)$$

$$na\tan(na) = S_d\, a/D_p \qquad (3.52)$$

The Green's function G is continuous at z' which leads to

$$G\,(z < z') = G(\,z > z')\ \text{ at }\ z = z' \qquad (3.53)$$

$$\lim_{\epsilon\to 0}\frac{\partial(G(z'+\epsilon)-G\,(z'-\epsilon))}{\partial z} = M_a N_a \cos(mx')\cos(ny') \qquad (3.54)$$

where $M_a = m/(ma + \left(\frac{1}{2}\right)\sin(2ma))$ and $N_a = n/(na + \left(\frac{1}{2}\right)\sin(2na))$

The values of A, B, C and D are obtained by solving the Equations (3.46), (3.47), (3.53) and (3.54).

The excess minority carrier (electrons) concentration is given by the volume integral:

$$\delta n\ (x, y, z) = \int_{z_j+w}^{d}\int_{-a}^{a}\int_{-a}^{a} G\, f\, dx\, dy\, dz$$

$$= \sum_{m,n}^{\infty} \frac{-4q\alpha F(1-R)M_g N_g \sin(ma)\sin(na)}{mna^2} \{A\left[L_2 e^{-\alpha z}\cosh\left(\frac{z}{L_2}\right) + \alpha L_2^2 e^{-\alpha z}\sinh\left(\frac{z}{L_2}\right) - I_{12}\right] + B\left[L_2 e^{-\alpha z}\sinh\left(\frac{z}{L_2}\right) + \alpha L_2^2 e^{-\alpha z}\cosh\left(\frac{z}{L_2}\right) - I_{11}\right] + C\left[I_{222} - L_2 e^{-\alpha z}\cosh\left(\frac{z}{L_2}\right) - \alpha L_2^2 e^{-\alpha z}\sinh\left(\frac{z}{L_2}\right)\right] + D[I_{111} - L_2 e^{-\alpha z}\sinh\left(\frac{z}{L_2}\right) - \alpha L_2^2 e^{-\alpha z}\cosh\left(\frac{z}{L_2}\right)]\}$$

(3.55)

The average photocurrent density at a given wavelength is obtained by

$$J_n(\lambda) = \frac{1}{4a^2}\int_{-a}^{a}\int_{-a}^{a} q\, D_n\left(\frac{\partial \delta n}{\partial z}\right)_{z=z_j+w}\, dx\, dy$$

$$= \sum_{m,n}^{\infty} \frac{4q\alpha F(1-R)M_g N_g \sin^2(ma)\sin^2(na)}{m^2 n^2 a^2 (1-\alpha^2 L_2^2)\left[\frac{1}{L_2} - \frac{1}{L_2}\frac{A_1}{A_2}\coth\left(\frac{H}{L_2}\right)\right]} \{\coth\left(\frac{H}{L_2}\right) \cosh\left(\frac{H}{L_2}\right)\left[\frac{I_{12}}{L_2} + \frac{A_1}{A_2}\frac{I_{111}}{L_2} - \frac{I_{222}}{L_2}\right] - \frac{I_{11}}{L_2}\cosh\left(\frac{H}{L_2}\right) + \sinh\left(\frac{H}{L_2}\right)\frac{A_1}{A_2}\left[-\frac{I_{12}}{L_2}\coth\left(\frac{H}{L_2}\right) + \frac{I_{11}}{L_2} - \frac{I_{111}}{L_2}\right] + \frac{I_{222}}{L_2}\sinh\left(\frac{H}{L_2}\right) - \alpha e^{-\alpha H}\left[-L_2 + \frac{A_1}{A_2}\coth\left(\frac{H}{L_2}\right) L_2\right]\}$$

(3.56)

where

$$H = Z_j + W \qquad (3.57)$$

$$I_{11} = L_2 \exp(-\alpha H)\sinh\left(\frac{H}{L_2}\right) + \alpha L_2^2 \exp(-\alpha H)\cosh\left(\frac{H}{L_2}\right) \qquad (3.58)$$

$$I_{12} = L_2 \exp(-\alpha H)\cosh\left(\frac{H}{L_2}\right) + \alpha L_2^2 \exp(-\alpha H)\sinh\left(\frac{H}{L_2}\right) \qquad (3.59)$$

$$I_{111} = L_2 \exp(-\alpha d)\sinh\left(\frac{d}{L_2}\right) + \alpha L_2^2 \exp(-\alpha d)\cosh\left(\frac{d}{L_2}\right) \qquad (3.60)$$

$$I_{222} = L_2 \exp(-\alpha d) \cosh\left(\frac{d}{L_2}\right) + \alpha L_2^2 \exp(-\alpha d) \sinh\left(\frac{d}{L_2}\right) \tag{3.61}$$

$$A_1 = \frac{1}{L_2} \cosh\left(\frac{d}{L_2}\right) + \frac{S_2}{D_n} \sinh\left(\frac{d}{L_2}\right) \tag{3.62}$$

$$A_2 = \frac{1}{L_2} \sinh\left(\frac{d}{L_2}\right) + \frac{S_2}{D_n} \cosh\left(\frac{d}{L_2}\right) \tag{3.63}$$

The total photocurrent density is given by

$$J_{total}(\lambda) = J_p(\lambda) + J_n(\lambda) + J_{dr}(\lambda) = J_{sc}(\lambda) \tag{3.64}$$

3.5 Current Density Calculations in the Dark Case

The continuity equation in n- and p- regions is solved using the Green's function by putting the generation rate equal to zero.

3.5.1 Derivation of the Current Equations in the N-Region

The continuity equation to be solved in the n-region of the cell is a partial differential equation of the form:

$$\nabla^2(p_n - p_{n0}) - (p_n - p_{n0})/L_p^2 = 0 \tag{3.65}$$

where the boundary conditions of this upper n-region are:

$$\frac{\partial(p_n - p_{n0})}{\partial z} = \frac{S_1}{D_p}(p_n - p_{n0}) \quad \text{at } Z=0 \tag{3.66}$$

$$p_n = p_{n0} \exp\left(\frac{qV_j}{kT}\right) \text{ at } Z=Zj \tag{3.67}$$

$$\frac{\partial(p_n - p_{no})}{\partial x} = \pm\frac{S_d}{D_p}(p_n - p_{n0}) \text{ at } x=\mp a \tag{3.68}$$

$$\frac{\partial(p_n - p_{no})}{\partial y} = \pm\frac{S_d}{D_p}(p_n - p_{n0}) \text{ at } y=\mp a \tag{3.69}$$

The excess minority carrier concentration (holes) is given by the surface integral:

$$\delta p\ (x, y, z) = \int_{-a}^{a}\int_{-a}^{a}(p_n - p_{n0})\,\frac{\partial G}{\partial z}\}_{z=z_j}\ dx\ dy \tag{3.70}$$

The average dark current density at a given voltage is obtained by

$$J_p(V_j) = \frac{1}{4a^2}\int_{-a}^{a}\int_{-a}^{a} q\ D_p\left(\frac{\partial \delta p}{\partial z}\right)_{z=z_j}\ dx\ dy \tag{3.71}$$

$$=\sum_{m,n}^{\infty}\frac{qD_p M_a N_a \sin^2(ma)\sin^2(na)}{m^2 n^2 a^2}\, p_{n0}\ \left\{\exp\left(\frac{qV_j}{kT}\right) - 1\right\}\left\{\frac{\left(\frac{S_1}{D_p}\right)\cosh\left(\frac{Z_j}{L_2}\right)+\left(\frac{1}{L_2}\right)\sinh\left(\frac{Z_j}{L_2}\right)}{\left(\frac{S_1 L_2}{D_p}\right)\sinh\left(\frac{Z_j}{L_2}\right)+\cosh\left(\frac{Z_j}{L_2}\right)}\right\} \tag{3.72}$$

3.5.2 Derivation of the Current Equations in the P-Region

The continuity equation to be solved in the p-region of the cell is a partial differential equation of the form:

$$\nabla^2(n_p - n_{p0}) - (n_p - n_{p0})/L_n^2 = 0 \tag{3.72}$$

where the boundary conditions of this lower p-region are:

$$n_p = n_{p0}\ \exp\left(\frac{qV_j}{kT}\right) \text{ at } Z=Zj+W \tag{3.73}$$

$$\frac{\partial(n_p - n_{p0})}{\partial z} = -\frac{S_z}{D_n}\left(n_p - n_{p0}\right) \text{ at } Z=d \tag{3.74}$$

$$\frac{\partial(n_p - n_{p0})}{\partial x} = \pm\frac{S_d}{D_n}\left(n_p - n_{p0}\right) \text{ at } x=\mp a \tag{3.75}$$

$$\frac{\partial(n_p - n_{p0})}{\partial y} = \pm\frac{S_d}{D_n}\left(n_p - n_{p0}\right) \text{ at } y=\mp a \tag{3.76}$$

The excess minority carrier concentration (electrons) is given by the surface integral:

$$\delta n\ (x,y,z) = \int_{-a}^{a}\int_{-a}^{a} -\left(n_p - n_{p0}\right)\frac{\partial G}{\partial z}\}_{z=z_{j+W}}\ dx\ dy \tag{3.77}$$

The average dark current density at a given voltage is obtained by

$$J_n\left(V_j\right) = \frac{1}{4a^2}\int_{-a}^{a}\int_{-a}^{a} q\ D_n\left(\frac{\partial \delta n}{\partial z}\right)_{Z=z_{j+W}}\ dx\ dy \tag{3.78}$$

$$=\sum_{m,n}^{\infty}\frac{-qD_n M_a N_a \sin^2(ma)\sin^2(na)}{m^2 n^2 a^2}\, n_{p0}\ \left\{\exp\left(\frac{qV_j}{kT}\right) - 1\right\}\left\{\frac{\left(\frac{1}{L_2}\right)\cosh\left(\frac{H}{L_2}\right) - \left(\frac{1}{L_2}\right)\frac{A_1}{A_2}\sinh\left(\frac{H}{L_2}\right)}{\sinh\left(\frac{H}{L_2}\right) - \frac{A_1}{A_2}\cosh\left(\frac{H}{L_2}\right)}\right\} \tag{3.79}$$

The total dark current density is given by

$$J_{total}\left(V_j\right) = J_p\left(V_j\right) + J_n\left(V_j\right) \tag{3.80}$$

3.6 Calculation of Spectral Response

Spectral response (S.R) is same as the quantum efficiency of the solar cell. The quantum efficiency (Q.E) is defined as the ratio of the number of electrons output by the solar cell to the number of photons incident on the device, while the spectral response determines the ratio of current generated by the solar cell to the power incident on the solar cell. Quantum efficiency can be determined from S.R by replacing the power of light at a particular wavelength with the photon flux for that wavelength, which gives

$$S.R = \frac{q\lambda}{hc}\,Q.E \tag{3.81}$$

The absorption coefficient was calculated as (Ghitani, 1989a):

$$\alpha\,(\lambda) = \exp(81.84 - 516.5\,\lambda + 1540\,\lambda^2 - 2421\,\lambda^3 + 2056\,\lambda^4 - 871.4\,\lambda^5 + 135.4\,\lambda^6)\ \mathrm{cm}^{-1}$$

(3.82)

where λ is in µm.

The S.R at different values of wavelength was calculated as:

$$\text{S.R}\,(\lambda) = \frac{J_{sc}(\lambda)}{q\,F(\lambda)} \tag{3.83}$$

where F is the photon flux reached at the surface and its unit is photons-cm^{-2} -sec^{-1} In these calculations F is taken as corresponding to AM1.5.

3.7 Limitations of the Model

Although the suggested model shows the effect of dislocations in all three dimensions, the model has several limitations. The main limitations associated with the model are as follows:

(i) The distance between two dislocations is taken to be more than Read radius so that the effect of electric field surround dislocation can be neglected.

(ii) The front and back surface recombination velocities were assumed to be independent function of dislocation density.

(iii) Similarly recombination activity is assumed to be an independent function of dislocation density.

(iv) The effect of dislocations is neglected in space charge region.

3.8 Summary

In this chapter the complete description of the dislocation model was discussed. The assumptions made in the creation of the model were also included in the discussion. Moreover the effect of front and back surface recombination velocities were considered in the model calculations which makes it unique in comparison to other dislocation models reported earlier by different research groups. The three-dimensional continuity equation for minority carriers was solved in n- and p- regions under the different cases of dark and light using Green's function. The expressions calculated for current density in dark and light cases can be compared with the experimental results of mesa diodes as well as with the results of commercial multicrystalline silicon solar cells. The simulation results of the dislocation model discussed in this chapter will be shown in chapter 5.

CHAPTER 4

DETAILS OF MESA DIODE ARRAYS

4.1 Introduction

The predictions of the dislocation model discussed in the earlier chapter are tested by means of the set of diode arrays called mesa diodes because the area of the diode is small. These diodes give quantitative information of defects and are used to characterize various substrate and cell parameters. Moreover these diodes are used to determine variations in device characteristics which are suitable for characterizing various solar cell fabrication processes. These diodes can be characterized under dark as well as light conditions in a manner similar to a solar cell. Although the fabrication of mesa diodes has been done by some research groups (Stirn, 1972), (Sopori, 1988a), (Ghitani, 1989b) and (Habler, 1995), this approach did not flourish because of lack of suitable processes for the fabrication of small mesa diodes.

Mesa diode analysis was used to see the effect of dislocations on solar cell performance. This technique was first reported by Sopori (Sopori, 1987, 1988b) for photovoltaics applications. Mesa diode analysis is a useful tool for the characterization of local electrical properties of the p-n junction of solar cells. Figure 4.1 shows the top view of mesa diode arrays on a circular silicon wafer. Suppose the Area 1 of this wafer has low defect density and Area 2 has high defect density. The diodes which are covered over Area 1 would have better performance and higher cell parameters than the diodes which are covered over Area 2.

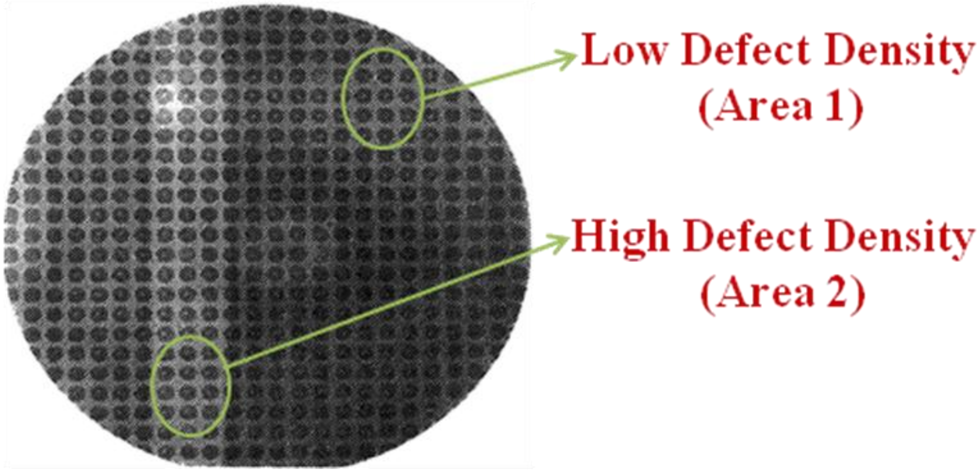

Figure 4.1 Top view of small mesa diode arrays (Sopori, 1988a).

4.2 Advantages of Mesa Diode Arrays

There are many advantageous features associated with mesa diode arrays. Mesa diode processing gives quantitative information about the defects and other substrate parameters of solar substrates. Mesa diode arrays are used for monitoring material quality and junction formation processes.

The advantages of mesa diode arrays are given as follows:

(i) The substrate parameters like resistivity, minority carrier diffusion length, etc. can be measured from mesa diode arrays.

(ii) Local photocurrent losses at different types of crystal defects can be determined. Moreover, photocurrent losses can be determined due to increased recombination of charge carriers via energy levels, segregation of impurities at defect sites and change in band structure due to localized stresses.

(iii) It gives the numerical value of dark forward and dark reverse current at each point of the cell and wafer.

4.3 Experimental Details of Fabrication of Mesa Diode Arrays

Figure 4.2 shows the process flow of the fabrication of mesa diode arrays. The starting material of the fabrication of mesa diode arrays is a p-type silicon wafer.

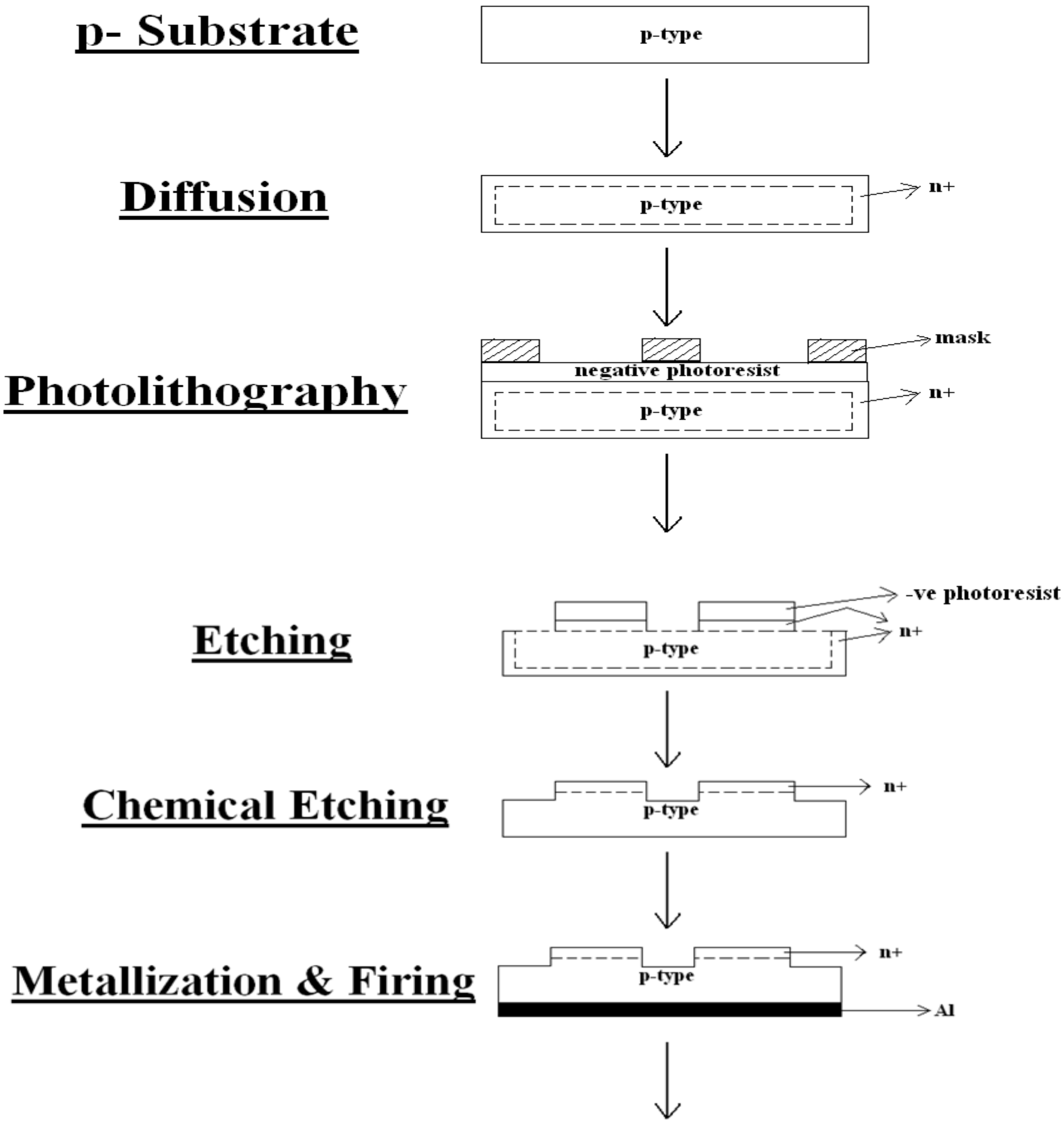

Figure 4.2 Schematic view of process flow of mesa diode arrays.

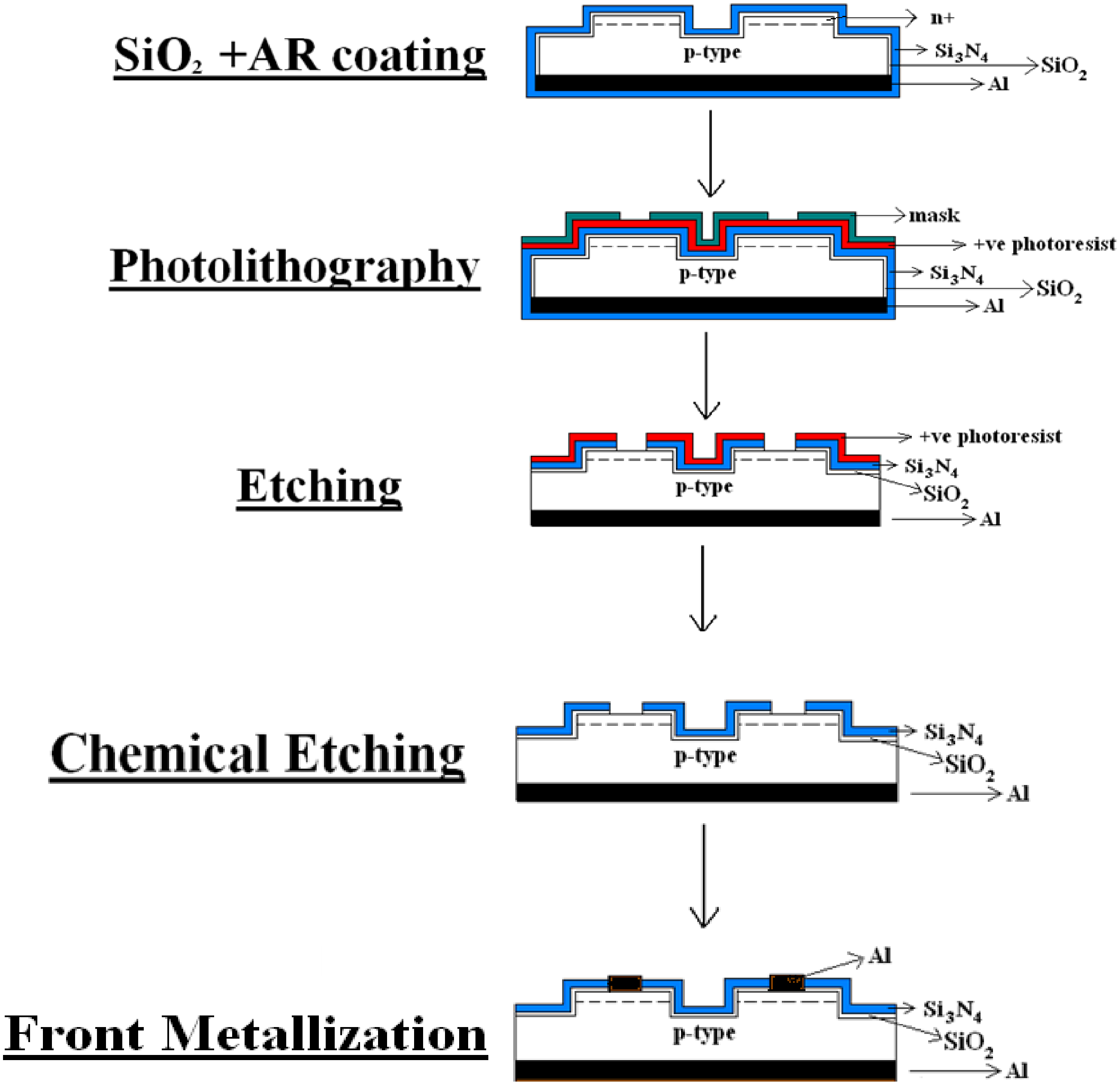

Figure 4.2 Schematic view of process flow of mesa diode arrays (continue).

First, the gettering techniques are being used on a p-type silicon wafer to remove surface damage. A solution of HNO_3: HF: CH_3COOH in the volume ratio of 3:2:2 is used to etch the samples to produce a shiny surface. After surface preparation the substrates are cleaned in piranha solution (H_2SO_4:H_2O_2= 3:1), rinsed in de-ionized water and dried in nitrogen. Then the diffusion of phosphorous is done at 850-900^{o}C to make the p-n junction. The diffused substrates are coated with negative photoresist. In the photolithography process the samples are first dehydrated. To dehydrate the surface, the samples are baked at 130^{o}C for 10 minute on a hotplate.

SU-8 was used as negative photoresist. SU-8 is a high contrast, epoxy-based photoresist designed for micromachining and other microelectronic applications, where a chemically thick and thermally stable image is desired (Taff, 2006). To deposit the layer of SU-8, the spin coating is performed at 3000 rpm for 30 seconds. After the spin coating, the samples are soft baked to evaporate the solvent and make the film to be dense. This step is called pre-baking. For the pre-baking the samples are heated at 95^{o}C for 60 seconds.

Table 4.1 Details of The Steps Used for Photolithography

Dehydration	Spin Speed	Pre Bake	Expose	Post exposure Bake	Development	Hard Bake
170^{o}C, 10 minutes	3000 rpm, 30 seconds (1.5 µm)	95^{o}C, 1 minute	60 seconds	95^{o}C, 90 seconds	80 seconds	225^{o}C, 11 minutes

After pre-baking the samples are exposed to UV radiation. Upon exposure, cross linking proceeds in the formation of a strong acid during the exposure process, followed by acid initiated, thermally driven epoxy cross linking during the post exposure bake (PEB) step. A PEB is performed to selectively cross-link the exposed portions of the film. After PEB the samples are developed for 80 seconds in SU-8 developer to remove the photoresist from unexposed areas. After development, the samples are hard baked at 225^{o}C for 11 minutes to further cross link the material. This completes the photolithography process. Figure 4.3 shows the images taken after photolithography by an optical microscope. The thickness of the photoresist film was measured to be 1.5 µm.

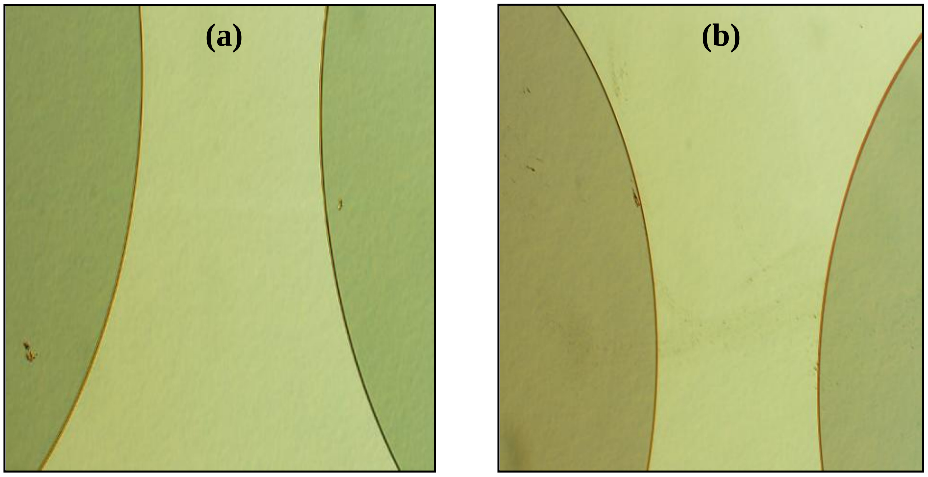

Figure 4.3 (a) Image taken after the photolithography from one area of the sample, and (b) Image taken after the photolithography from another area of the sample.

Figure 4.3 shows the outside region of the circles. Inside the circle there is a film of photoresist on the silicon substrate. The portion outside the circle was unexposed during photolithography. This portion etched after development. Inside the circle there is a negative photoresist which acts as a mask for the next step of etching to isolate the two diodes. The diameter of the circles is 0.254 cm. The brief details of the steps used for photolithography are shown in Table 4.1.

After photolithography, mesa etching of the masked substrates was done typically for 30 seconds using Sopori etch (Sopori, 1984). Sopori etch consists of a solution of HF: CH_3COOH: HNO_3 in the volume ratio of 36:20:1. This etching process also removes the unwanted diffused regions from the back side of the sample. After the Sopori etch process the photoresist mask is removed in piranha solution. Figure 4.4 shows the images taken after mesa etching from optical microscope.

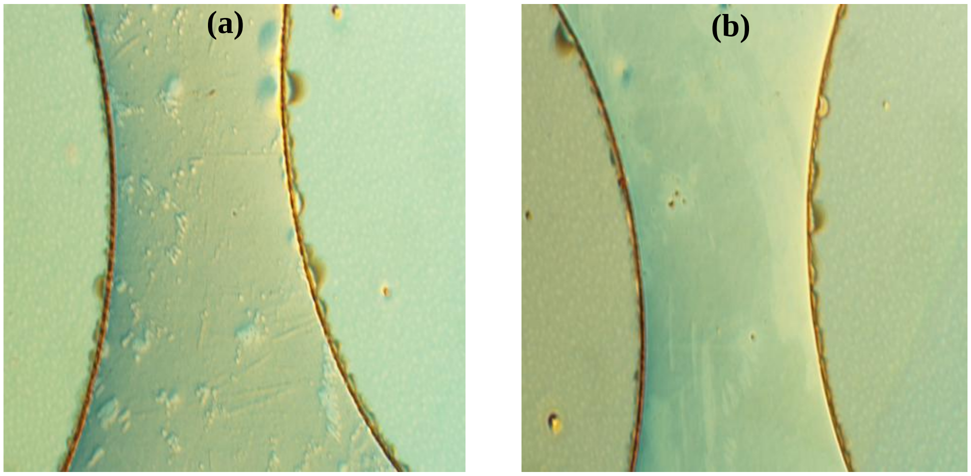

Figure 4.4 (a) Image taken after the mesa etching from one area of the sample, (b) Image taken after the mesa etching from another area of the sample.

After the mesa etching process the samples go for back metallization consisting of an aluminium deposition and subsequent alloying. The aluminium alloying is done in an optical processing furnace (OPF) (Sopori, 1993). The samples are placed with the mesa facing the lamps. The light intensity is controlled so that a uniform Si-Al alloy layer is formed on the back side, which provides a back surface field (Roos, 1978).

The front surface of the sample is oxidized for 60 seconds in the same furnace by flowing oxygen in the furnace. The oxidation results in ~100 Å of SiO_2. Samples for mesa diodes go through a deposition of 100 Å of SiO_2 and 850 Å of Si_3N_4 after the mesa etching step. This coating not only acts as a mask for metallization but also provides an antireflection (AR) coating.

After SiO_2+Si_3N_4 deposition, photolithography is again done using AZ1400 photoresist to open the front pattern. The front metallization pattern is opened up by etching SiO_2+Si_3N_4 in buffered HF. For the front metallization the lift-off technique is used to remove Al over the photoresist, leaving metal in the desired regions of the contact.

4.4 Characterization Results on Mesa Diode Arrays

The characterization of mesa diode arrays was done on several devices. The diodes were fabricated on a single silicon wafer. The details of fabrication steps are already being discussed in section 4.3. Figure 4.5 shows the short circuit current densities of six diodes. After the measurement it was observed that diode 3 had the highest short circuit current and the lowest short circuit current was observed in diode 6. This suggests that diode 3 was fabricated over a region of low defect density and diode 6 was over a region of high defect density. Figure 4.6 shows the open circuit voltage measurements on the same diodes. It can be noted that the observed open circuit voltages follow the similar trend as that of the short circuit currents in Figure 4.5. This further suggests that the location of diode 3 is over a region of low defect density whereas diode 6 is over a region of high defect density.

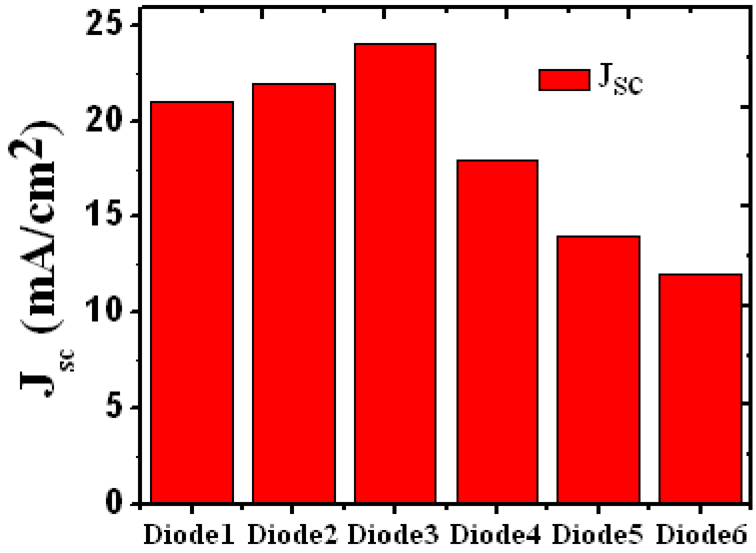

Figure 4.5 J_{sc} measurements on six different diodes.

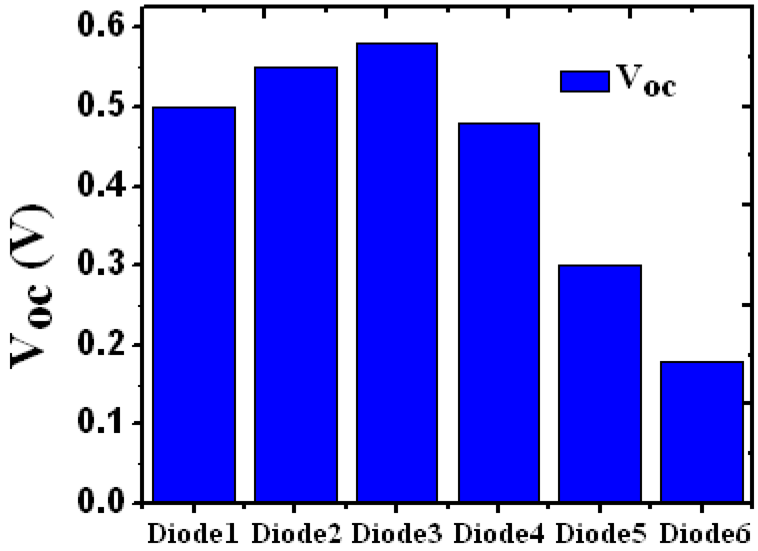

Figure 4.6 V_{oc} measurements on six different diodes.

CHAPTER 5

IDENTIFICATION OF DISLOCATIONS USING MESA DIODES

5.1 Introduction

In the earlier chapters the theoretical and experimental details of mesa diode arrays have been shown. Moreover, how the mesa diode analysis gives the quantitative information of the defects have been discussed in earlier chapters. The dislocation model described in chapter three has the capability to compare the theoretical results with the experimental results on mesa diodes. The fabrication details of processing of mesa diodes have been discussed in chapter 4. This chapter discusses the experimental results achieved on mesa diode arrays and the simulation results of dislocation model.

5.2 Simulation of Dislocation Models

In this model the effect of several parameters like dislocation density (N_d), recombination activity at dislocations (S_d), minority carrier diffusion length in n and p region etc have been considered. The influence of front (S_1) and back (S_2) surface recombination velocities have been computed at front and back surfaces of n^+-p junction silicon solar cells respectively, on spectral response and short circuit current density. All these calculations were done at the cell thickness of 200 µm. The values of Z_j, L_p and L_n were taken to be 0.3 µm, 10 µm and 400 µm respectively.

5.2.1 Effect of Variation in N_d and S_d

The effect of dislocation density and recombination activity was seen on spectral response, J-V characteristics and short circuit current density. Figure 5.1 a shows the variation of S.R vs. wavelength at different values of S_d, in the case of low dislocation density and Figure 5.1 b shows the variation of S.R vs. wavelength at different values of S_d, in the case of high dislocation density. In both cases the S.R shifted downward as the recombination activity increases. The peak of S.R photocurrent is shifted towards the longer wavelengths as the dislocation density decreases. The front and back surface recombination velocities were taken to be finite.

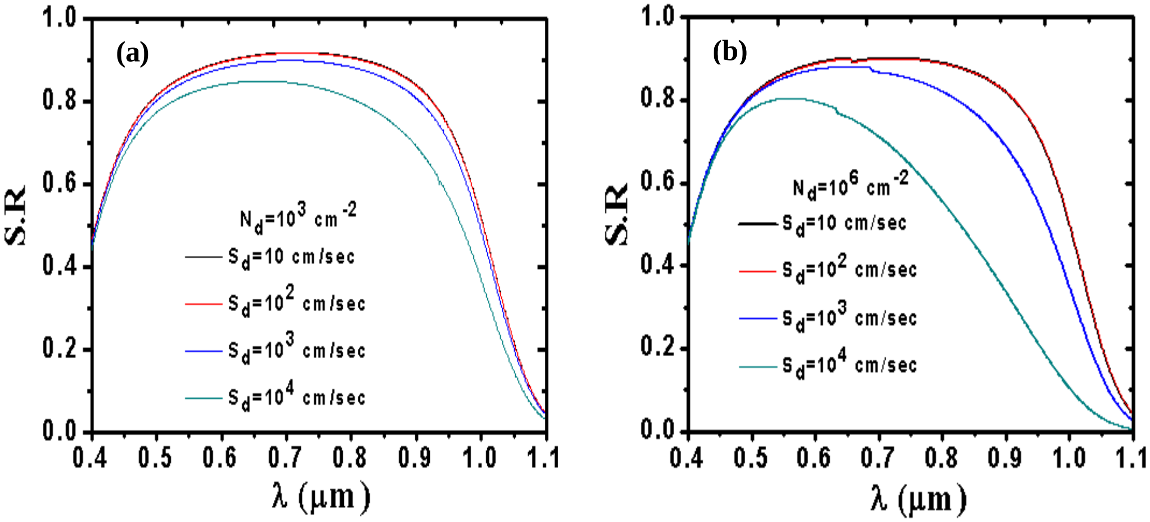

Figure 5.1 S.R vs. wavelength at different values of S_d, $S_1=10^3$ cm/sec, $S_2=10^4$ cm/sec, $Z_j=0.3$ μm, (a) $N_d=10^3$ cm^{-2}; (b) $N_d=10^6$ cm^{-2}.

The short circuit current is calculated from S.R values at different wavelengths under the assumption of air mass (AM) 1.5. The spreadsheet of Solar Spectral Irradiance for AM 1.5 gives the power density 1000 W/m^2. All the calculations were done at this power density. This spread sheet is provided by NREL and available publically. The variation of J-V characteristics is shown in Figure 5.2 at different recombination activities. This figure is plotted by assuming the average dislocation of 10^4 cm^{-2} and finite values of front and back surface recombination velocities.

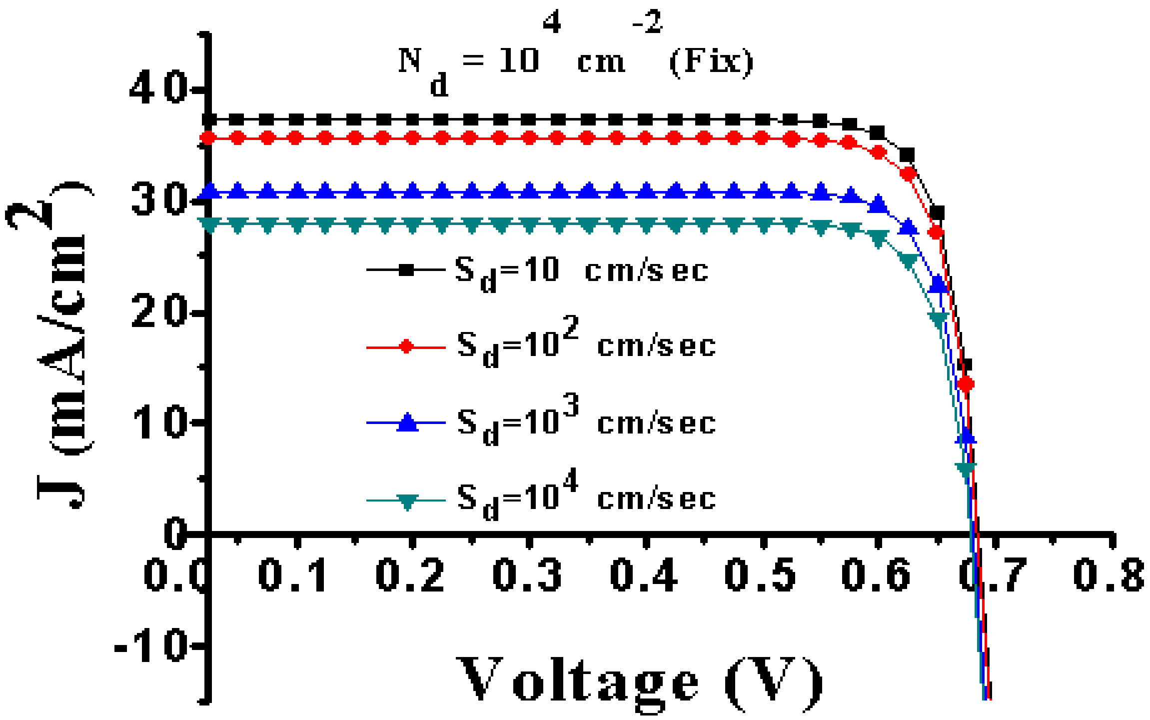

Figure 5.2 Calculated J-V characteristics in the case of N_d fix and S_d vary.

Figure 5.3 shows the variation of S.R vs. wavelength at different values of N_d and other parameters like S_d, S_1, S_2 etc. are fixed. The peak of S.R is shifted towards the longer wavelengths as the dislocation density decreases and the maximum of S.R is shifted towards the shorter wavelengths when N_d increases. There is negligible change in S.R with dislocation density at shorter wavelengths because of the low blue response at $S_d = 10^4$ cm/sec.

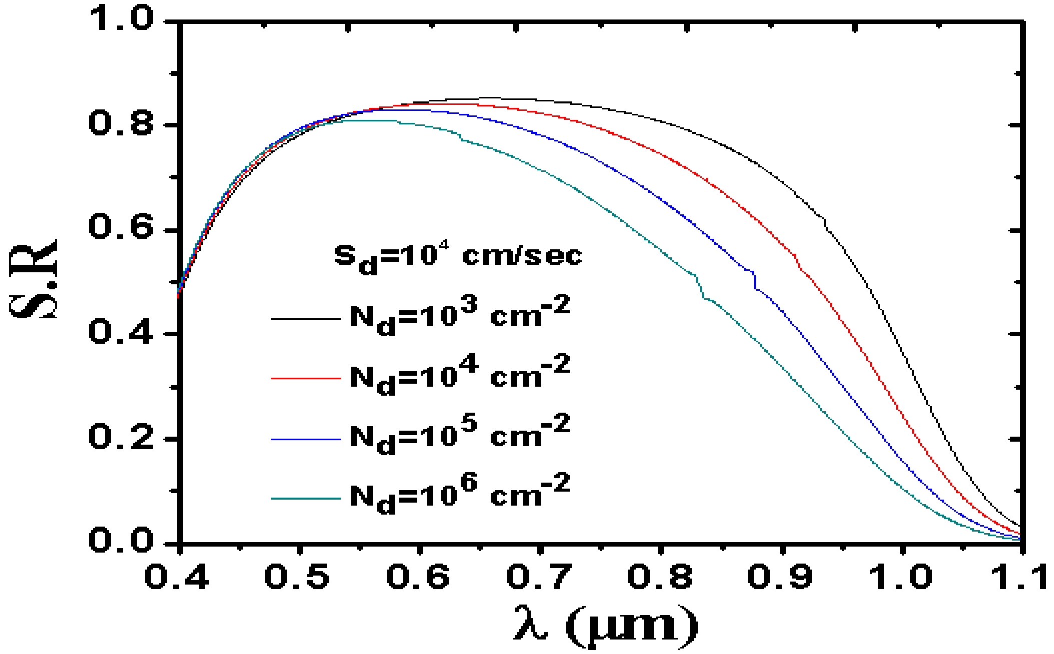

Figure 5.3 S.R vs. wavelength at different values of N_d, $S_1=10^3$ cm/sec, $S_2=10^4$ cm/sec, $Z_j=0.3$ μm, $S_d= 10^4$ cm/sec.

Figure 5.4 shows the calculated J-V characteristics at different dislocation densities. The curves of Figure 5.4 indicate as N_d increases, the recombination at dislocations becomes the dominant factor.

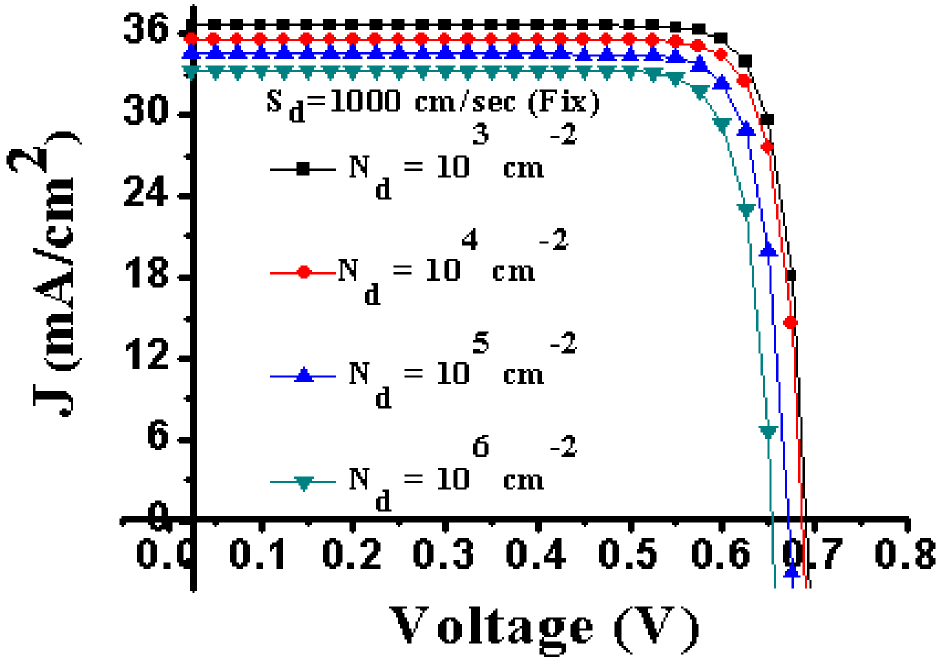

Figure 5.4 Calculated J-V characteristics in the case of S_d fix and N_d vary.

The increase in N_d and S_d not only causes a decrease in the maximum value of S.R, but also a shift of the maximum towards shorter wavelengths.

5.2.2 Effect of Variation in S_1

Figures 5.5 a and 5.5 b show the variation of S.R vs. wavelength at different values of S_1. The difference in S.R values at different values of S_1 was seen at shorter wavelength. This happens because at shorter wavelength the absorption depth is low. The light having shorter wavelength give the recombination properties of the front surface as it will absorb at the surface. S.R shifts upward as S_1 decreases because it gives better blue response at lower values of S_1. At longer wavelengths there is no change in S.R values with respect to S_1. This effect can be clearly seen in Figure 5.5, where the value of S.R becomes constant with S_1 after the wavelength of 0.7 µm. At shorter wavelengths one can clearly see the difference in the curves with respect to S_1.

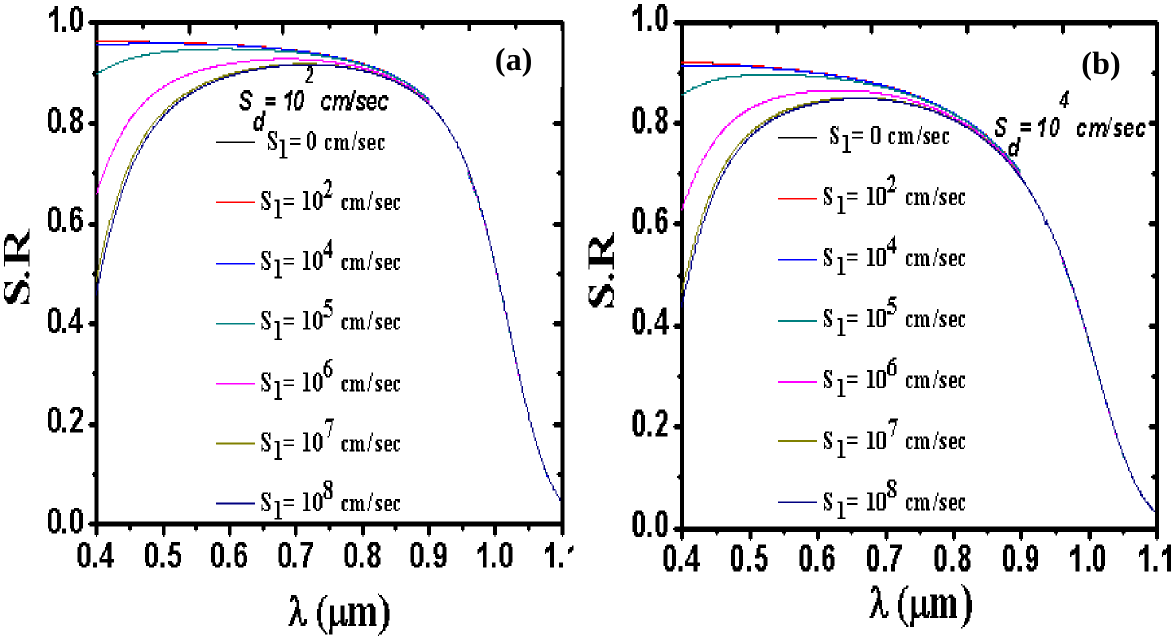

Figure 5.5 The variation of S.R vs. wavelength at different values of S_1, N_d= 10^3 cm^{-2} (fix) (a) S_d=10^2 cm/sec; (b) S_d=10^4 cm/sec.

To see the further effect of S_1, J_{sc} values were plotted at two different dislocation densities. The higher value of J_{sc} was obtained at lower dislocation density and is shown in Figure 5.6. The change in J_{sc} values is negligible below the S_1 values of 10^4 cm/sec and above the S_1 values of 10^8 cm/sec. The change in J_{sc} value is more pronounced when S_1 varies from 10^4-10^7 cm/sec.

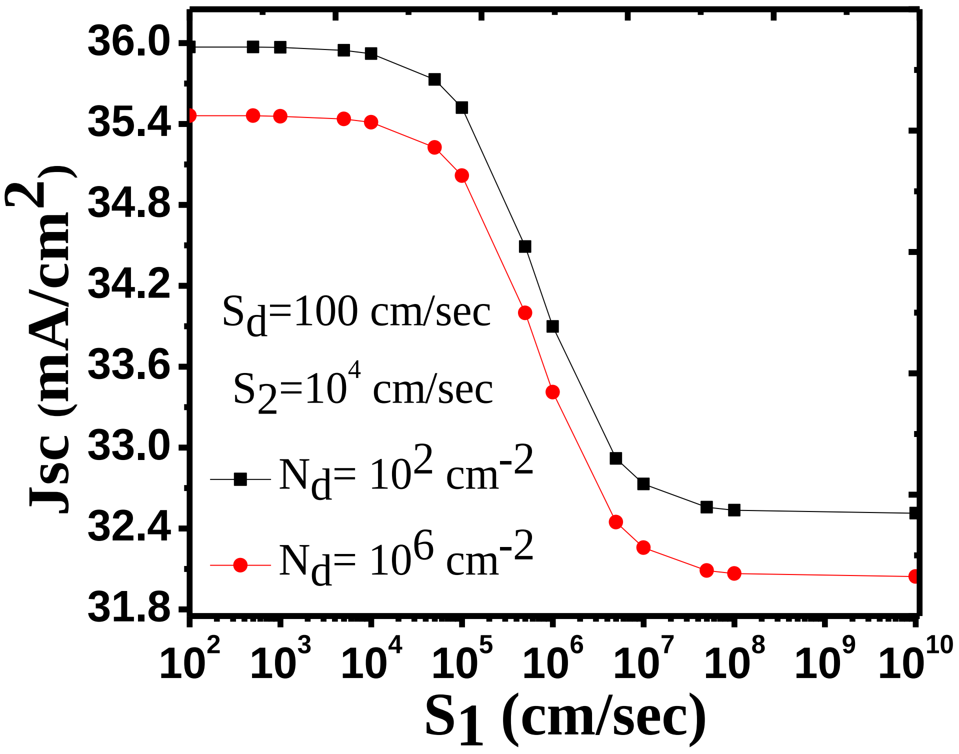

Figure 5.6 Comparison of J_{sc} values at different dislocation densities with respect to the variation in S_1.

5.2.3 Effect of Variation in S_2

Figures 5.7 a and 5.7 b show the variation of S.R vs. wavelength at different values of S_2. The difference in S.R values at different values of S_2 was seen at longer wavelength. This happens because at longer wavelength the absorption depth is high. The light having longer wavelength give the recombination properties of the bulk. As the S_2 decreases the spectral response shifts upward. At shorter wavelengths there is no change in S.R values with respect to S_2. This effect can be clearly seen in Figures 5.7 a and 5.7 b, where the value of S.R is constant with S_2 below the wavelength of 0.7 µm. At longer wavelengths one can clearly see the difference in the curves with respect to S_2.

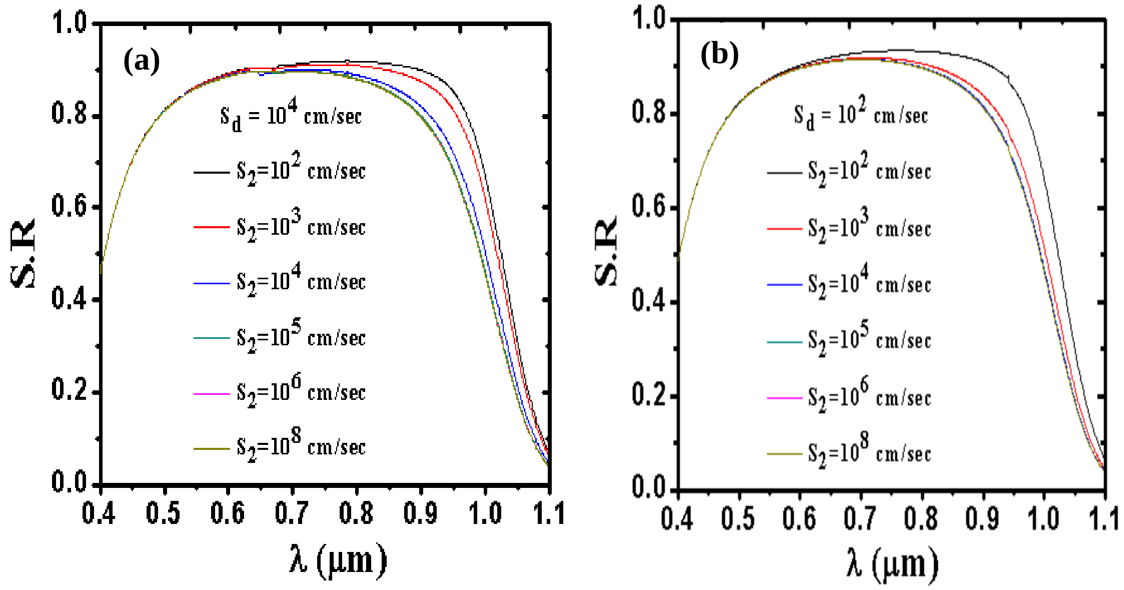

Figure 5.7 The variation of S.R vs. wavelength at different values of S_2, N_d= 10^3 cm^{-2} (fix) (a) S_d=10^2 cm/sec; (b) S_d=10^4 cm/sec.

To see the further effect of S_2, J_{sc} values were plotted at two different dislocation densities. The higher value of J_{sc} was obtained at lower dislocation density and is shown in Figure 5.8. The change in J_{sc} values is negligible above the S_2 values of 10^6 cm/sec. The change in J_{sc} value is more pronounced when S_2 varies from 10^2 -10^6 cm/sec.

The change in S.R with respect to S_2 will be more pronounced when the thickness of cell is further reduced by the solar industries. This will happen because in thinner wafer the generation rate will be significant at the back surface and no longer be neglected. In Figure 5.9 the cell thickness was varied from 150 µm to 50 µm to see the change in S.R values with respect to S_2.

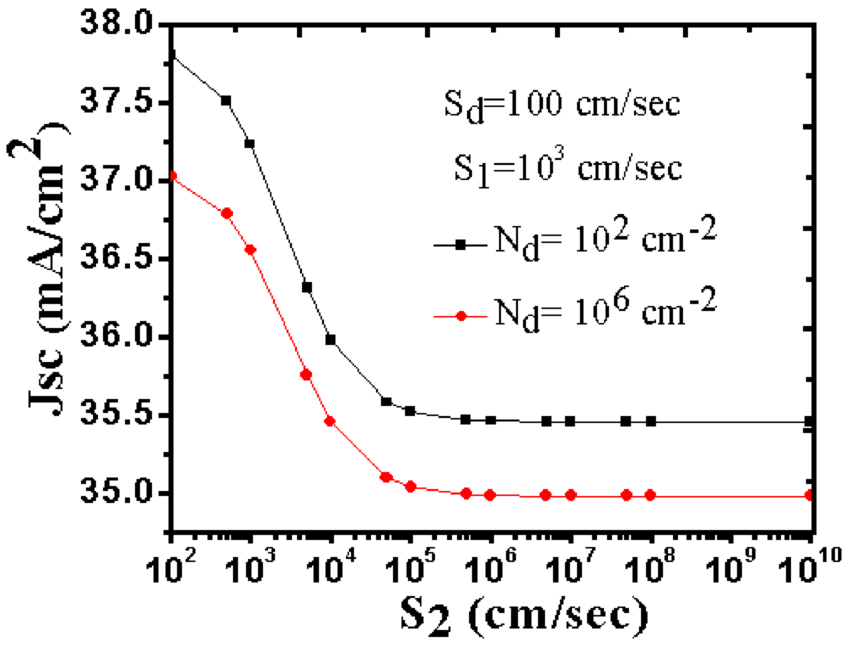

Figure 5.8 Comparison of J_{sc} values at different dislocation densities with respect to the variation in S_2, when S_1= 10^3 cm/sec.

Figures 5.9 a1, 5.9 b1 and 5.9 c1 show the variation of S.R at different values of S2 in wavelength range of 0.4 µm to 1.1 µm. When the cell thickness is 150 µm there is no change in S.R values with respect to S_2 at wavelengths below 0.67 µm as shown in Figure 5.9 a1. When the cell thickness is 100 µm there is no change in S.R values with respect to S_2 at wavelengths below 0.64 µm as shown in Figure 5.9 b1. When the cell thickness is 50 µm there is no change in S.R values with respect to S_2 at wavelengths below 0.57 µm as shown in Figure 5.9 c1. The change in S.R values between high and low value of S_2 increases as the thickness of cell reduces. Figures 5.9 a2, 5.9 b2 and 5.9 c2 show the variation of S.R with respect to S_2 at a cell thickness of 150 µm, 100 µm and 50 µm respectively. In Figure 5.9 a1, 5.9 b1 and 5.9 c1 the wavelengths below

0.7 μm have been excluded so that one can clearly see the difference in S.R values between the lowest and highest value of S_2.

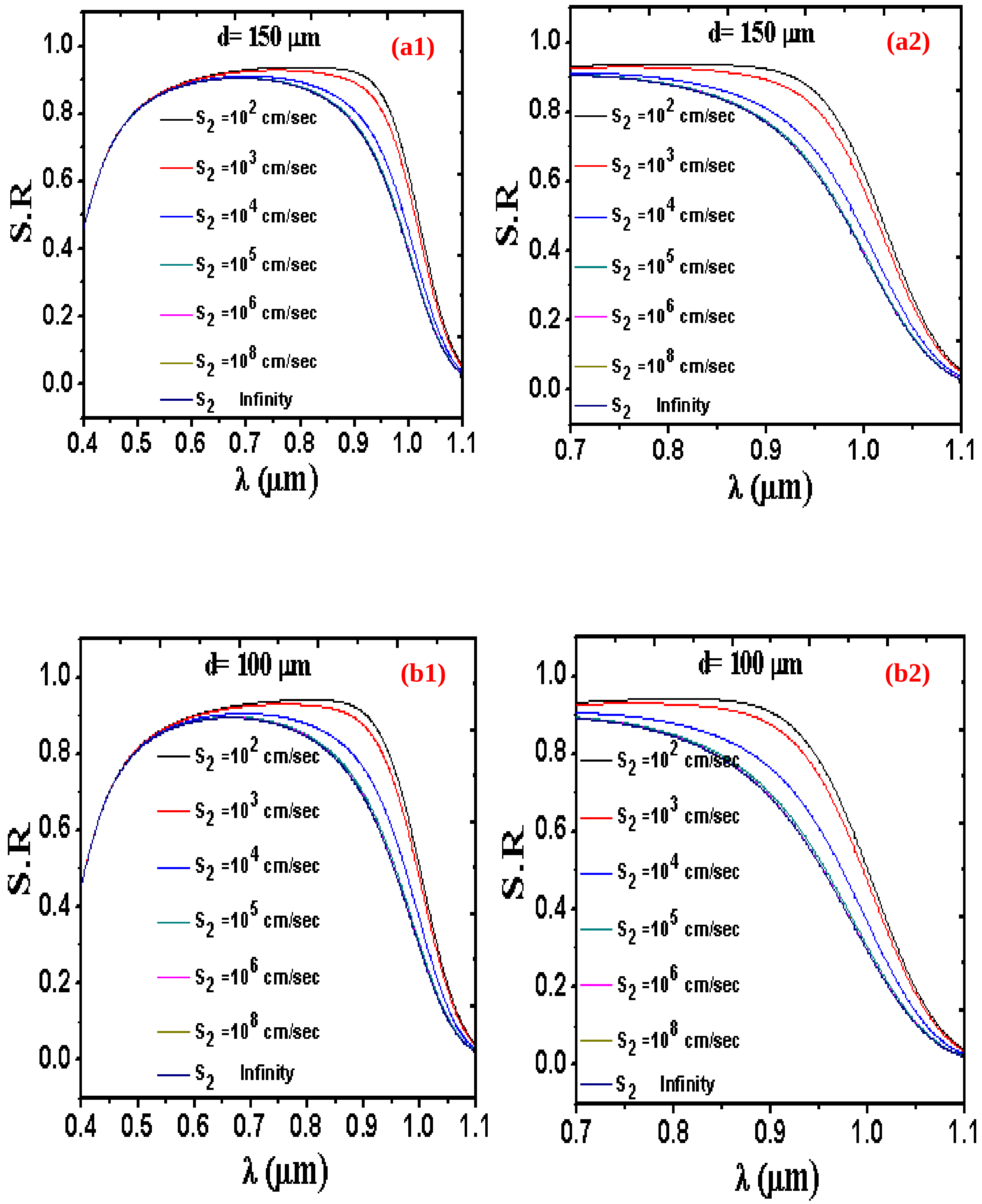

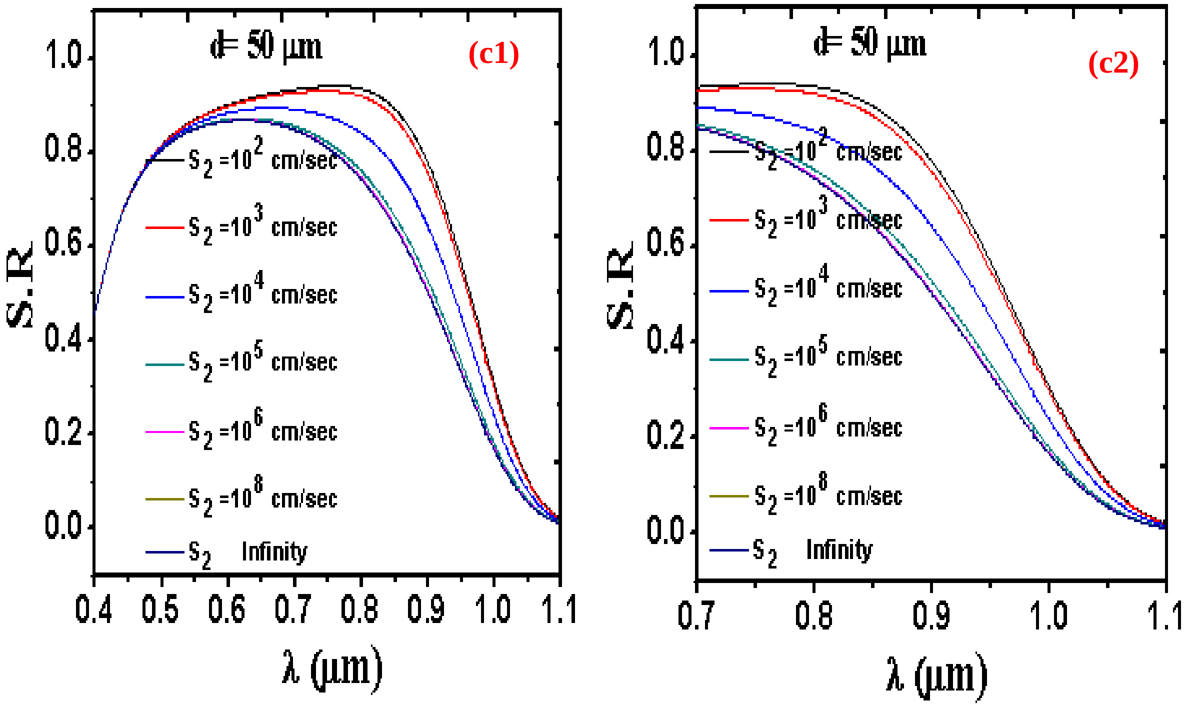

Figure 5.9 The variation of S.R vs. wavelength at different values of S_2, (a1) d=150 µm & λ=(0.4 µm -1.1 µm); (a2) d=150 µm & λ=(0.7 µm -1.1 µm); (b1) d=100 µm & λ=(0.4 µm -1.1 µm); (b2) d=150 µm & λ=(0.7 µm -1.1 µm); (c1) d=50 µm & λ=(0.4 µm -1.1 µm); (c2) d=50 µm & λ=(0.7 µm -1.1 µm).

5.2.4 Comparison Between Modeling and Experimental Results

In this model the effect of S_1 and S_2 is considered and makes significant difference when it has finite values. The calculated value of short circuit current density (J_{sc}) at different dislocation densities are shown in Figure 5.10. The J_{sc} decreases as the recombination activity increases at different dislocation densities. All the values of J_{sc} were plotted at finite values of front and back surface recombination velocities. At lower values of S_d, the change in J_{sc} is negligible when the dislocation density is below 10^5 cm^{-2}. At higher values of S_d, the change in J_{sc} is negligible when dislocation density is below 10^5 cm^{-2}.

As the recombination activity increases the sudden change in J_{sc} will start at low values of dislocation densities which is also in agreement with the results of Ghitani 1989a, who neglected the front and back surface recombination velocity.

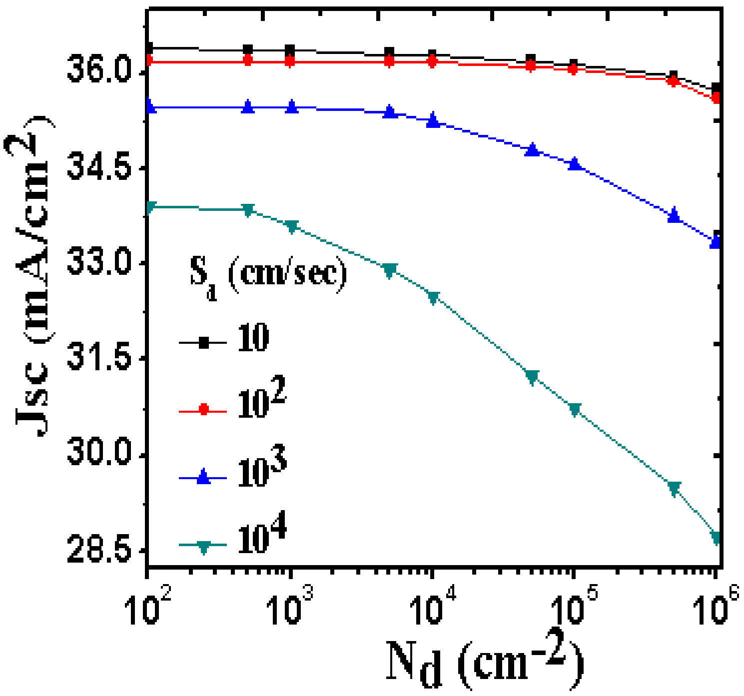

Figure 5.10 Modeling result: J_{sc} vs. N_d at different values of S_d, when $S_1=10^3$ cm/sec, $S_2=10^3$ cm/sec.

The modeling results were compared with experimental results reported by Sopori, 1987. In their work they showed the quantitative effect of dislocations on cell parameters using mesa diode arrays (Sopori, 1988). The comparison between these two results is shown in Figure 5.11. In the comparison the value of S_1 was taken to be 10^6 cm/sec and the value of S_2 was taken to be 10^5 cm/sec. The experimental results were done on ribbon sample without AR coating which may be reason of the difference between experimental and modeling values, but from this comparison it is clear that there will be a drop in J_{sc} and V_{oc} values if the dislocation density increases more than 10^4 cm^{-2}.

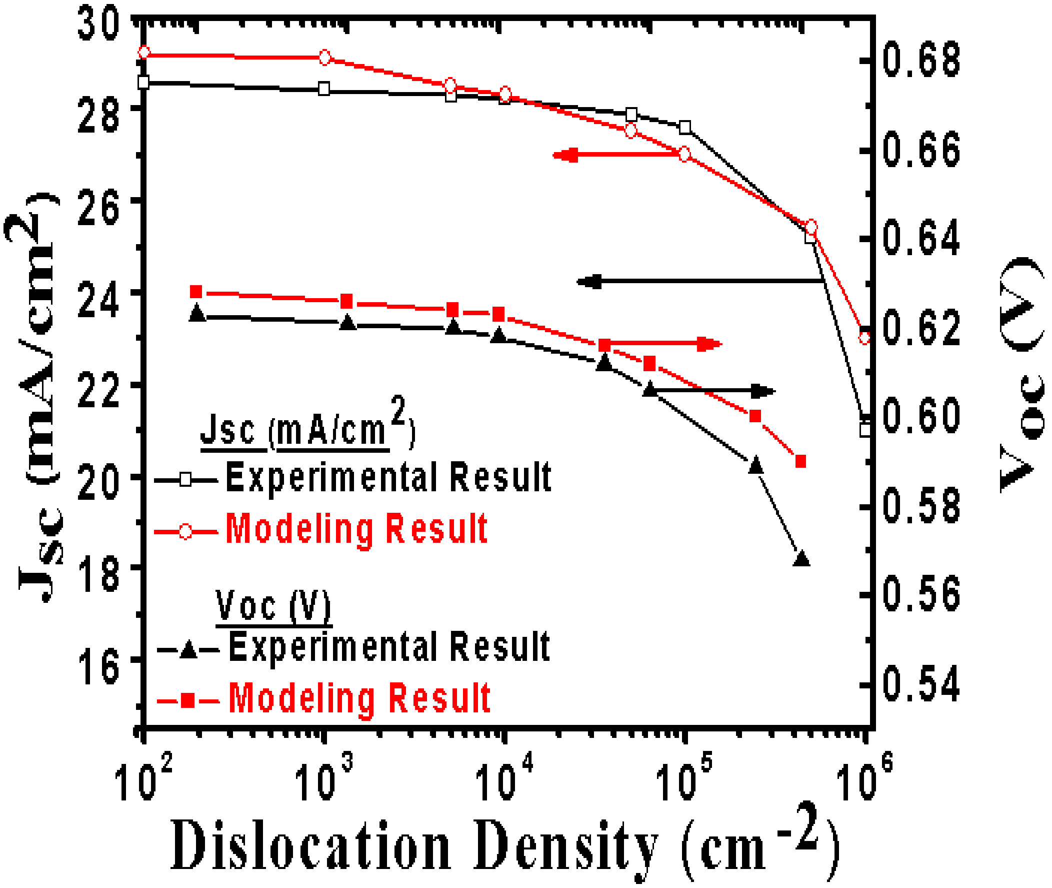

Figure 5.11 Comparison between modeling and experimental results, when $S_1=10^5$ cm/sec, $S_2=10^5$ cm/sec, $S_d=5 \times 10^3$ cm/sec, R=0.85, $Z_j=0.4$ µm.

5.2.5 Comparison Between the Improved and Old Dislocation Model

The J_{sc} and V_{oc} values of the improved model were compared with the Ghitani's (Ghitani, 1989a) model in which the effect of front and back surface recombination velocities were neglected.

The comparison between J_{sc} values are given in Table 5.1 when S_1 and S_2 were taken to finite and S_1 and S_2 were neglected or assumed to be infinity. At low recombination recombination activity the difference in J_{sc} value increases when dislocation density decreases as it is seen in Table 5.1, the percentage change in J_{sc} is increasing with an increase in dislocation density. At high recombination activity there is a little increase in the percentage change in J_{sc} when N_d decreases from 10^4 cm^{-2} to 10^3 cm^{-2}.

Table 5.1 Change in J_{sc} When S_1 and S_2 are Considered and Neglected, Z_j =0.3 µm

S_d (cm/sec)	N_d (cm^{-2})	J_{sc} (mA/cm^2) S_1 =10^3 cm/sec S_2=10^3 cm/sec	J_{sc} (mA/cm^2) S_1 and S_2 neglected	% change in J_{sc}
10^2	10^5	34.9163	23.9965	45.51
10^2	10^4	35.0644	24.0044	46.07
10^2	10^3	35.7120	24.45	46.08
10^4	10^5	27.9406	20.4759	36.45
10^4	10^4	29.9241	22.4650	33.20
10^4	10^3	31.6754	23.7423	33.41

Similarly the comparison between V_{oc} values are given in Table 5.2 when S_1 and S_2 are taken to finite and S_1 and S_2 are neglected or assumed to be infinity.

Higher values of J_{sc} and V_{oc} will be achieved if surface passivation techniques like SiNx:H passivation, back surface field etc. are used in the fabrication of solar cells. In that case it is important to consider the finite values of front and back surface recombination velocity.

Table 5.2 Change in V_{oc} When S_1 and S_2 are Considered and Neglected, S_d= 10^3 cm/sec

Zj (µm)	**N_d (cm^{-2})**	**V_{oc} (V)** **S_1 =10^3 cm/sec** **S_2=10^3 cm/sec**	**V_{oc} (V)** **S_1 and S_2 neglected**
0.4	10^5	0.63	0.61
0.4	10^4	0.641	0.62
0.4	10^3	0.652	0.63
0.3	10^5	0.645	0.63
0.3	10^4	0.66	0.645
0.3	10^3	0.68	0.653

5.2.6 Effect of Variation in Efficiency

Efficiency is an important parameter in the performance of solar cells. Figure 5.12 shows the effect of variation in efficiency at different dislocation densities as estimated using this model. The efficiency of solar cell decreases as the dislocation density increases. There is a marginal change in cell efficiency when the dislocation density increases from 10^2 to 10^3 cm^{-2}. The change in surface recombination velocity is negligible when the dislocation density is between 10^2 cm^{-2} and 10^3 cm^{-2}. There is a rapid decrease in efficiency once the dislocation density goes above 10^3 cm^{-2}. The effect of surface recombination velocities is more pronounced at higher dislocation densities.

Similar change in efficiency was seen when the recombination activity was increase while keeping the dislocation density constant. The variation of efficiency vs. S_d is shown in Figure 5.13. A negligible variation in efficiency was observed for S_d values below 10^3 cm/sec and this change was increased as the S_d was increased above 10^4 cm/sec. As described in Chapter 1, identical results were reported while solving continuity equation for minority carriers in one dimension (Diamitriadis, 1985).

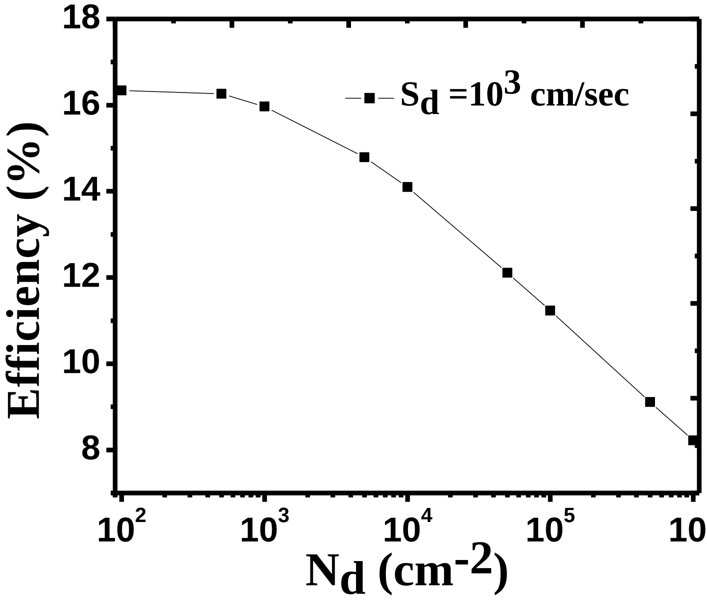

Figure 5.12 Efficiency vs. dislocation density at a fix value of S_d.

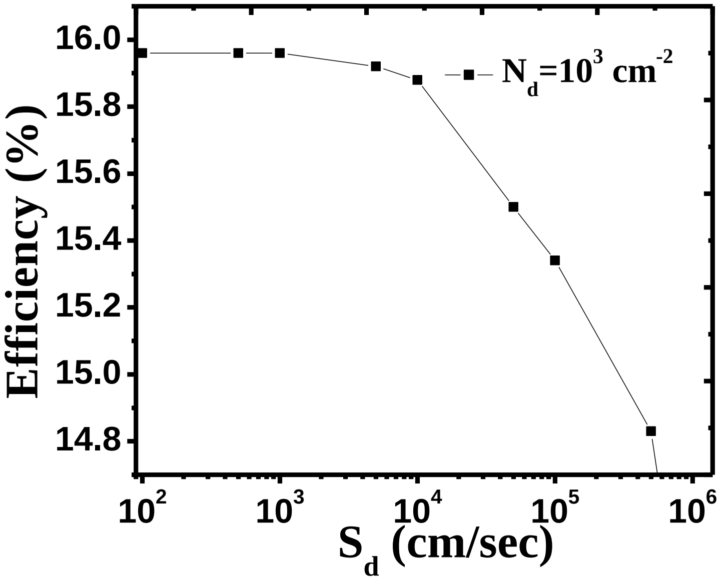

Figure 5.13 Efficiency vs. recombination activity at a fix value of N_d.

CHAPTER 6

CONCLUSIONS AND FUTURE WORK

6.1 Conclusions

The three dimensional model of dislocations was developed using Green’s function with an effect of front and back surface recombination velocity. In the model the uniform distribution of dislocations are considered and the influence of defects are considered in all three dimensions. In the model the current density equations were solved in both light and dark cases.

The modeling results indicate the effect of dislocation density and recombination activity at dislocations on spectral response and J-V characteristics. As the dislocation density and recombination activity increases, it has an adverse effect on the performance of solar cell as expected. From the spectral response calculation it was shown in the results that the effect of front surface recombination velocity is more pronounced at shorter wavelengths and the effect of back surface recombination velocity is more pronounced at longer wavelengths. The shorter wavelength of light gives the recombination properties of front surface and longer wavelength of light gives the recombination properties of bulk.

The effect of back surface recombination velocity cannot be neglected in the present crystalline silicon solar cell technology because the thickness of silicon wafer is reduced by solar industries to reduce cost. Ghitani (Ghitani, 1989a) concluded that the dislocation effect is less marked when the thickness is less than 50 µm. In his model the back surface recombination velocity was assumed to be infinity. In modeling results it was shown that the effect of defects are more pronounced especially the back surface recombination velocity when the cell thickness is less than or equal to 50 µm.

The comparison between experimental and modeling results showed some agreement between two results. There is sudden change in J_{sc} and V_{oc} values when dislocation density exceeds 10^4 cm^{-2}. The present model can also be used to compare with experimental results of solar cells fabricated on silicon and other semiconductor materials having similar features.

A significant difference was observed in the magnitude of J_{sc} and V_{oc} values when front and back surface recombination velocities was taken to be finite and when both were considered to be infinity. This clearly shows that the experimental results of the crystalline silicon solar cells made up on large grain size material cannot be compared with the dislocation models reported by earlier groups in the past.

6.2 Future Work

The suggested model can only be applied to polycrystalline semiconductor material having the same features. In suggested model the continuity equation was solved in three dimensions by assuming the uniform distribution of dislocations. An obvious extension of model is possible by considering a regular array of nonhomogenously recombining dislocations.

The suggested model works for the semiconductor materials of large grain size. The effect of grain boundary is neglected in the model. The extension of the model is possible by considering the uniform distribution of grain boundary and dislocations.

Although suggested model cannot be applied for tandem cells or the devices having multi junctions, suggested model can be extended by solving continuity equation in different regions using same concept of Green’s function. Moreover the effect of p+ region which provides back surface field can also be included.

The processing of good mesa diodes is still a big challenge. It needs to optimize all the steps used for fabrication. During the mesa etching step some parts of negative photoresist get removed from the corners of the circle of the mesa diodes.

REFERENCES

Aberle, A.G., Wenham, S.R., & Green, M.A. (1993). A new method for accurate measurements of the lumped series resistance of solar cells. *23rd IEEE Photovoltaics Specialists Conference, Louisville, Kentucky, USA*, 133-139.

Agarwal, S.K., Muralidharan, R., Agarwal, A., Tewary, V.K., & Jain, V.K. (1981). A new methos for measurement of series resistance of solar cells. *Journal of Physics D: Applied Physics, 14,* 1643-1646.

Alexander, H., & Teichler, H. (2000). *Dislocations.* Chapter 6. Handbook of Semiconductor Technology. Edited by: K.A.Jackson, W.Schroter. WILEY-VCH Verlag GmbH.

Anderson, B.L., & Anderson, R.L. (2005). *Fundamentals of Semicondutor Devices*. New York: McGraw-Hill Companies, Inc., 139-142.

Bary, A., & Nouet, G. (1998). Electrical activity of the first- and second-order twins and grain boundaries in silicon. *Journal of Applied Physics, 63,* 435-438.

Basore, P. (1994). Defining terms for crystalline silicon solar cells, *Progress in Photovoltaics: Research and Applications, 2,* 177-179.

Bentzen, A., & Holt, A. (2009). Overview of phosphorous diffusion and gettering in multicrystalline silicon. *Materials Science and Engineering B, 159-160,* 228-234.

Breitenstein, O., Rakotoniaina, J.P., Rifai, M.H.A., & Werner, M. (2004). Shunt types in crystalline silicon solar cells. *Progress in Photovoltaics: Research and Applications, 12,* 529-538.

Breitenstein, O., Rakotoniaina, J.P., & Rifai, M.H.A. (2003). Quantitative evaluation of shunts in solar cells by lock-in-thermography. *Progress in Photovoltaics: Research and Applications, 11,* 521-526.

Budhraja, V., Misra, D., & Ravindra, N.M. (2011a). Advancements in PV multicrystalline silicon solar cells from 1980 to 2010 – An Overview, *37th IEEE Photovoltaic Specialists Conference, Seattle, Washington.*

Budhraja, V., Sopori, B., Ravindra, N.M., & Misra, D. (2011b). An improved model of dislocations in a silicon solar cell. *21st Workshop On Crystalline Silicon Solar Cells & Modules: Materials and Processes*, Breckenridge, Colorado, July 31-August 3, 2011.

Buonassisi, T., Istratov, A.A., Pickett, M.D., Heuer, M., Kalejs, J.P., Hahn, G., Marcus, M.A., Lai, B., Cai, Z., Heald, S.M., Ciszek, T.F., Clark, R.F., Cunningham, D.W., Gabor, A.M., Jonczyk, R., Narayanan, S., Sauar, E., & Weber, E.R. (2006). Chemical natures and distributions of metal impurities in multicrystalline silicon materials. *Progress in Photovoltaics: Research and Applications, 14,* 513-531.

Buonassisi, T., Heuer, M., Istratov, A.A., Pickett, M.D., Marcus, M.A., Lai, B., Cai, Z., Heald, S.M., & Weber, E.R. (2007). Transition metal co-precipitation mechanisms in silicon. *Acta Materialia, 55,* 6119-6126.

Card, H.C., & Yang, E.S. (1977). Electronic processes at grain boundaries in polycrystalline semiconductors under optical illumination. *IEEE Transactions on Electron Devices, 24,* 397-402.

Chen, J., Chen, B., Sekiguchi, T., Fukuzawa, M., & Masayoki, Y. (2008). Correlation between residual strain and electrically active grain boundaries in multicrystalline silicon. *Applied Physics Letters, 93,* 112105.

Clugston, D., & Basore, P. (1997). Pc1D Version 5:32 bit Solar Cell Modeling on personal computers. 26th *IEEE Photovoltaics Specialists Conference, Anaheim, CA, USA*, 207-210.

Cousins, P.J., & Cotter, J.E. (2006). The influence of diffusion-induced dislocations on high efficiency silicon solar cells. *IEEE Transactions on Electron Devices, 53, 3,* 457-464.

Cuevas, A., Stocks, M., Armand, S., Stuckings, M., Blakers, A., & Ferrazza, F. (1997). High minority carrier lifetime in phosphorous-gettered multicrystalline silicon. *Applied Physics Letters, 70,* 1017-1019.

Dekkers, H.F.W., Carnel, L., & Beaucarne, G. (2006). Carrier trap passivation in Si solar cells by hydrogen from SiNx:H layers. *Applied Physics Letters, 89,* 013508-013510.

Dimitriadis, C.A. (1985). Influence of dislocations on the performance of solar cells made from large-grain polysilicon. *Journal of Applied Physics: D, 18,* 2489-2495.

Ding, J., & Radhakrishnan, R. (2008). A new method to determine the optimum load of a real solar cell using the Lambert W-function. *Solar Energy Materials and Solar Cells, 92,* 1566-1569.

Donolato, C. (1993). Modeling the effect of dislocations on the minority carrier diffusion length of a semiconductor. *Journal of Applied Physics, 84*, 2656-2664.

Durinckx, F., & Szlufcik, J. (2002). Defect passivation of industrial multicrystalline solar cells based on PECVD silicon nitride. *Solar Energy Materials and Solar Cells, 72,* 231-246.

Dyk, E.E.V., & Meyer, E.L. (2004). Analysis of the effect of parasitic resistances on the performance of photovoltaic modules. *Renewable Energy, 29,* 333-344.

Fauchet, P. (2003). Porous Polycrystalline Silicon thin Film Solar Cells. *National Renewable Energy Laboratory Subcontractor Report.* MREL/SR-520-34824.

Fossum, J.G., & Lindholm, F.A. (1980). Theory of grain boundary and intragrain recombination currents in polysilicon p-n junction solar cells. *IEEE Transaction on Electron Devices, 27,* 692-700.

Fujiara, K., Pan, W., Usami, N., Sawada, K., Tokairin, M., Nose, Y., Nomura, A., Shishido, T., & Nakajima, K. (2006). Growth of structure-controlled polycrystalline silicon ingots for solar cells by casting. *Acta Materialia, 54,* 3191-3197.

Fujiwara, K., Maeda, K., Usami, N., & Nakajima, K. (2008a). Generation mechanism of Si-faceted dendrites. *Physical Review Letters, 101,* 055503.

Fujiwara, K., Maeda, K., Usami, N., Sazaki, G., Nose, Y., Nomura, A., Shishido, T., & Nakajima, K. (2008b). In situ observation of Si faceted growth from low-degree-of-undercooling melts. *Acta Materialia, 56,* 2663-2668.

Ghitani, H.El., & Martinuzzi, S. (1989a). Influence of dislocations on electrical properties of large grained polycrystalline silicon cells I Model. *Journal of Applied Physics, 76,* 1717-1722.

Ghitani, H.El., & Martinuzzi, S. (1989b). Influence of dislocations on electrical Properties of large grained polycrystalline silicon cells II Experimental Results. *Journal of Applied Physics, 76,* 1723-1726.

Gilles, D. (1990). Mechanism of internal gettering of interstitial impurities in Cz-grown silicon. *Physics Review Letters, 64,* 196-199.

Green, M.A. (1998). *Solar Cells Operating Principles, Technology and System Applications*. New Jersey: Prentice-Hall, Inc.,Englewood Cliffs, N.J.

Habler, C., Thurm, S., Koch, W., Karg, D., & Patel, G. (1995). Mesadiode analysis of solar cells (MASC): A new characterization technique for solar silicon. *13th European Photovoltaic Solar Energy Conference, NICE, France,* 1364-1367.

Halder, N.C., & Williams, T.R. (1983). Grain boundary effects in polycrystalline silicon solar cells I: Solution of the three dimensional diffusion equation by the green's function method. *Solar Cells, 8,* 201-223.

Hartman, H., Bartony, M., Serdy, J., & Buonassisi, T. (2008). Dislocation density reduction in multicrystalline silicon solar cell material by high temperature annealing *Applied Physics Letters, 93,* 12108.

Hinken, D., Ramspeck, K., Bothe, K., Fischer, B., & Brendel, R. (2007). Series resistance imaging of solar cells by voltage dependent electroluminescence. *Applied Physics Letters, 91,* 182104.

Hussein, R., Borchert, D., Grabosch, G., & Fahrner, W.R. (2001). Dark I-V-T measurements and characteristics of (n) a-Si/(p) c-Si heterojunction solar cells. *Solar Energy Materials & Solar Cells, 69,* 123-129.

Istratov, A.A., Buonassisi, T., McDonald, R.J., Smith, A.R., Schindler, R., Rand, J.A., Kalejs, J.P., & Weber, E.R. (2003). Metal content of multicrystalline silicon for solar cells and its impact on minority carrier diffusion length. *Journal of Applied Physics, 94,* 6552-6559.

Johnson, S.M., & Winter, C. (1984). High efficiency large area polysilicon solar cells. *17th IEEE Photovoltaic Specialists Conference,* 1121-1126.

Kaminski, A., Breitenstein, O., Boyeaux, J.P., Rakotoniaina, P., & Laugier, A. (2004). Light beam induced current and infrared thermography studies of multicrystalline silicon solar cells. *Journal of Physics: Condensed Matter, 16,* S9-S18.

Kazmerski, L. (2011). Research efficiency plot for various photovoltaic technologies 1976-2011. *http://en.wikipedia.org/wiki/File:PVeff(rev110901).jpg* Data compiled by National Renewable Energy Laboratory (NREL).

Kieliba, T., Riepe, S., & Warta, W. (2006). Effect of dislocations on open circuit voltage in crystalline silicon solar cells. *Journal of Applied Physics, 100,* 093708.

Kittler, M., Seifert, W., Stemmer, M., & Palm, J. (1995). Interaction of iron with a grain boundary in boron doped multicrystalline silicon. *Journal of Applied Physics, 77,* 3725-3728.

Kurobe, K., & Matsunami, H. (2005). New two diode model for detailed analysis of multicrystalline silicon solar cells. *Japanese Journal of Applied Physics, 44,* 8314-8321.

Lal, P.M., & Singh, S.N. (2006). A new method of determination of series and shunt resistances of silicon solar cells. *Solar Energy Materials and Solar Cells, 91,* 137-142.

Langenkamp, M., & Breitenstein, O. (2002). Classification of shunting mechanisms in crystalline silicon solar cells. *Solar Energy Materials and Solar Cells, 72,* 433-440.

Lax, M. (1978). Junction current and luminescence near a dislocation or a surface. *Journal of Applied Physics, 49,* 2796-2810.

Macdonald, D., Cuevas, A., & Ferrazza, F. (1999). Response to phosphorous gettering of different regions of cast multicrystalline silicon ingots. *Solid State Electronics, 43,* 575-581.

Macdonald, D.H., Cuevas, A., Kerr, M.J., Samundsett, C., Ruby, D., Winderbaum, S., & Leo, A. (2004). Texturing industrial multicrystalline silicon solar cells. *Solar Energy, 76,* 277-283.

Martinuzzi, S., Perichaud, I., & Warchol, F. (2003). Hydrogen passivation of defects in multicrystalline silicon solar cells. *Solar Energy Materials and Solar Cells, 80,* 343-353.

Matare, H.F. (1970a). *Fundamentals of Charge Carrier Transport.* Chapter 2, Defect Electronics in Semiconductors. New York: John Wiley & Sons, Inc.

Matare, H.F. (1970b). *Basic Electrical Properties of Dislocations in Semiconductors.* Chapter 8, Defect Electronics in Semiconductors. New York: John Wiley & Sons, Inc.

Matare, H.F. (1970c). *Anisotropy of Charge Carrier Transport.* Chapter 9, Defect Electronics in Semiconductors. New York: John Wiley & Sons, Inc.

Matare, H.F. (1970d). *Dislocations and the Electronic Properties of Semiconductor Devices.* Chapter 14, Defect Electronics in Semiconductors. New York: John Wiley & Sons, Inc.

Maurice, J.L., & Colliex, C. (1989). Fast diffusers Cu and Ni as the origin of electrical activity in a silicon grain boundary. *Applied Physics Letters, 55,* 241-243.

Magzine article. C-Si Putting Pressure On Thin Films, *Solar Industry*, January, 2011, pp. 4.

McHugo, S.A., Hieslmair, H., & Weber, E.R. (1997). Gettering of metallic impurities in photovoltaic silicon. *Applied Physics A: Materials Science & Processing, 64,* 127-137.

McHugo, S.A., Thompson, A.C., Perichaud, I., & Martinuzzi, S. (1998). Direct correlation of transition metal impurities and minority carrier recombination in multicrystalline silicon. *Applied Physics Letters, 72,* 3482-3484.

McQuarrier, D.A. (2003). *Mathematical Methods for Scientists and Engineers*. University science books, Sausalito, California, USA, 702-705.

Mittelstadt, L., Dauwe, S., Metz, A., Hezel, R., & Habler, C. (2002). Front and rear silicon nitride passivated multicrystalline silicon solar cells with an efficiency of 18.1%. *Progress in Photovoltaics: Research and Applications, 10,* 35-39.

Moller, H.J., Kaden, T., Scholz, S., & Wurzner, S. (2009). Improving solar grade silicon by controlling extended defect generation and foreign atom defect interactions. *Applied Physics.A, Materials Science & Processing, 96,* 207-220.

Narayanan, S., Wenham, S.R., & Green, M.A. (1986). High efficiency polycrystalline silicon solar cells using phosphorous pretreatment. *Applied Physics Letters, 48,* 873-875.

Nielsen, L.D. (1982). Distributed series resistance effects in solar cells. *IEEE Transaction on Electron Devices, 29,* 821-827.

Nishioka, K., Sakitani, N., Uraoka, Y., & Fuyuki, T. (2007). Analysis of multicrystalline silicon solar cells by modified 3-diode equivalent circuit model taking leakage current through periphery into consideration. *Solar Energy Materials and Solar Cells, 91,* 1222-1227.

Nouri, H., Bouaicha, M., & Bessais, B. (2009). Effect of porous silicon on the performance of silicon solar cells during the porous silicon based gettering procedure. *Solar Energy Materials and Solar Cells, 93,* 1823-1826.

Oldham, W.G., & Milnes, G.A. (1964). Interface states in abrupt semiconductor heterojunctions. *Solid State Electronics, 7,* 153-165.

Opdorp, C. Yan, Vink, A.T., & Werkhoven, C. (1977). Minority carrier recombination at surfaces, dislocations, microdefects: evaluation of parameters from near band edge luminescence *MO, 1976, edited by L.F.Eastman, Inst. Phys. Conf. Ser. Proceeding of the 6th III-V Symposium, St. Louis, 33b,* 317.

Pauls, K.L., Mitchell, K.W. & Chesarek, W. (1993). The effect of dislocations on the performance of silicon solar cells. *23rd IEEE Photovoltaic Specialist Conference,* 209-213.

Pysch, D., Mette, A., & Glunz, S.W. (2007). A review and comparison of different methods to determine the series resistance of solar cells. *Solar Energy Materials and Solar Cells, 91,* 1698-1706.

Read, W.T. (1954). Theory of Dislocations in Semiconductors. *Philosophical Magazine, 45,* 775-796.

Rizk, R., Portier, X., Allais, G., & Nouet, G. (1994). Electrical and structural studies of copper and nickel precipitates in a ∑=25 silicon bicrystal. *Journal of Applied Physics, 76,* 952-958.

Rohatgi, A., Narasimha, S., Kamra, S., Doshi, P., Khattak, C.P., Emery, K., & Field, H. (1996). Record high 18.6% efficienct solar cell on HEM multicrystalline material. *25th IEEE Photovoltaic Specialist Conference,* 741-744.

Roos, O.V. (1978). A simple theory of back surface field for solar cells. *Journal of Applied Physics, 49,* 3503-3511.

Ruby, D.S. (1996). Optimization of plasma deposition and etching processes for commercial mc-Si solar cells. *25th IEEE Photovoltaics Specialist Conference,* 637-640.

Saitoh, T., Warabisako, T., Kuroda, E., Itoh, H., Matsubara, S., & Tokuyama, T. (1980). Impurity gettering of polycrystalline solar cells fabricated from refined metallurgical grade silicon. *IEEE Transactions of Electron Devices, 27,* 671-677.

Sana, P. Salami, J., & Rohatgi, A. (1993). Fabrication and analysis of high efficiency polycrystalline silicon solar cells. *IEEE Transactions on Electron Devices, 40,* 1461-1468.

Schottky, W. (1945). Semiconductor problems. *Halbleiterprobleme, Vieweg, Braunschweig, 1,* 227.

Schultz, O., Glunz, S.W., & Willeke, G.P. (2004). Multicrystalline silicon solar cells exceeding 20% efficiency. *Progress in Photovoltaics Research and Applications, 12,* 553-558.

Seager, C.H., & Ginley, D.S. (1981). Studies of the hydrogen passivation of silicon grain boundaries. *Journal of Applied Physics, 52,* 1050-1055.

Seager, C.H. (1982). The determination of grain boundary recombination rates by scanned spot excitation methods. *Journal of Applied Physics, 53,* 5968-5971.

Shockley, W. (1962). Diffusion and drift of minority carriers in semiconductors for comparable capture and scattering mean free paths. *Physical Review, 125,* 1570-1576.

Sopori, B.L., & Baghdadi, A. (1980). Some investigations on the influence of defects/grain boundaries on photovoltaic mechanisms in polycrystalline silicon films. *Solar Cells, 1,* 237-250.

Sopori, B.L. (1984). A new defect etch for polycrystalline silicon. *Journal of Electrochemical Society, 131,* 667-672.

Sopori, B.L. (1987). Crystal defects in RTR ribbons: Their characteristics and influence on the ribbon cell performance. *Journal of Crystal Growth, 82,* 228-236.

Sopori, B.L. (1988a). Fabrication of diode arrays for photovoltaic characterization of silicon substrates. *Applied Physics Letters, 52,* 1718-1720

Sopori, B.L. (1988b). A backside hydrogenation technique for defect passivation in silicon solar cells. *Journal of Applied Physics, 64,* 5264-5266.

Sopori, B.L. (1991). Silicon solar cell materials research: current progress and future needs. *Solar Cells, 30,* 373-381.

Sopori, B.L., Marshall, C., Rose, D., Jones, K.M., Reedy, R., & Asher, S. (1993). Optical processing: A novel technology for fabricating solar cell contacts. 23rd *IEEE Photovoltaics Specialists Conference, Louisville, KY, USA,* 97-100.

Sopori, B., (2003). *Thin Film Silicon Solar Cells.* Chapter 8, Handbook of Photovoltaic Science and Engineering. Edited by A. Luque and S. Hegedus, John Wiley & Sons, Ltd, ISBN: 0-471-49196-9, (pp. 307-357).

Sopori. B., Budhraja. V., Rupnowski, P., Johnston, S., Call, N., Mountinho, H.& Jassim, M.Al. (2009a). Defect clusters in multicrystalline silicon: Their nature and influence on solar cell performance. *34th IEEE PVSC, Philadelphia, PA, June 7-12,* 1969-1974.

Sopori. B., Rupnowski, P., Mehta, V., Budhraja. V., Johnston, S., Call, N., Mountinho, H.& Jassim,M.Al., Shaikh, A., Seacrist, M., & Carlson, D. (2009b). Performance limitations of mc-Si solar cells caused by defect clusters. *ECS Transactions, The Electrochemical Society, 18,* 1049-1058.

Sopori. B., Rupnowski, P., Shet, N., Budhraja. V., Johnston, S., Call, N., Seacrist, M., Shi, G., Chen, J., & Deshpande, A. (2010). Influence of defects and defect distribution in multicrystalline silicon on solar cell performance. *35th IEEE Photovoltaics Specialists Conference, Hawai, USA,* 2233-2237.

Stirn, R.J. (1972). Junction Characteristics of silicon solar cells. *9th IEEE Photovoltaics Specialists Conference, Silver Spring, New York,* 72-82.

Stokkan, G. (2010). Relationship between dislocation density and nucleation of multicrystalline silicon. *Acta Materialia, 58,* 3223-3229.

Swanson, R.M. (2006). A vision for crystalline silicon photovoltaics. *Progress in Photovoltaics Research and Applications, 14,* 443-453.

Taff, J., Kashte, Y., Mamo, V.S., & Paranjapea, M. (2006). Fabricating multilevel SU-8 structures in a single photolithographic step using colored masking patterns. *Journal of Vacuum Science Technology A, 24,* 742-746.

Takahashi, I., Usami, N., Kutsukake, K., Stokkan, G., Morishita, K., & Nakajima, K. (2010). Generation mechanism of dislocations during directional solidification of multicrystalline silicon using artificially designed seed. *Journal of Crystal Growth, 312*, 897-901.

Tarasov, I., Ostapenko, S., Nakayashiki, & Rohatgi, A. (2004). Defect passivation in multicrystalline silicon for solar cells. *Applied Physics Letters*, *85,* 4346-4348.

Tobias, I., Canizo, C.D., & Alonso, J. (2003). *Crystalline silicon solar cells and modules.*Chapter 7, Handbook of Photovoltaic Science and Engineering. Edited by A. Luque and S. Hegedus, John Wiley & Sons, Ltd, ISBN: 0-471-49196-9, (pp. 255-305).

www.thermosensorik.de accessed: Aug, 2011.

Wan, Y., Zhang, T., You, D., Du, J., Xiao, G., & Zhong, D. (2010). Keep the advantage of mc-Si solar cells through larger ingots and better quality wafers. *The 16th International Conference on Crystal Growth,* Beijing, China, August, 8-13, 2010.

Wang, J., Tsurekawa, S., Ikeda, K., Sekiguchi, T., & Watanabe, T. (1999). Relationship between electrical activity and grain boundary structural configuration in polycrystalline silicon. *Interface Science*, *7,* 197-205.

Website: http://ecee.colorado.edu/~bart/book/book/chapter2/ch2_9.htm accessed: Aug, 2011.

Wenham, S.R., Willison, M.R., Narayanan, S., & Green, M.A. (1985). Efficiency improvement in screen printed polycrystalline silicon solar cells by plasma treatments. *18th IEEE Photovoltaic Specialists Conference,* 1008-1013.

Wu, B., Stoddard, N., Ma, R., & Clark, R. (2008). Bulk multicrystalline silicon growth for photovoltaic (PV) application. *Journal of Crystal Growth, 310,* 2178-2184.

Yamaguchi, M., Yamamoto, A., & Itoh, Y. (1986). Effect of dislocations on the efficiency of thin-film GaAs solar cells on silicon substrates. *Journal of Applied Physics, 59,* 1751-1753.

Zhao, J., Wang, A., & Green, M.A. (1998). 19.8% efficienct honeycomb textured multicrystalline and 24.4% monocrystalline silicon solar cells. *Applied Physics Letters*, *73,* 1991-1993.

Zolper, J.C., Narayanan, S., Wenham, S.R., & Green, M.A. (1989). 16.7% efficient, laser texture, buried contact polycrystalline silicon solar cell. *Applied Physics Letters, 55,* 2363-2365.

Zook, J.D. (1980). Effects of grain boundaries in polycrystalline solar cells. *Applied Physics Letters, 37*, 223-226.